Next Generation Lipid Nanoparticles for mRNA Delivery

DISSERTATION

zur Erlangung des Grades
„Doktor der Naturwissenschaften“
im Promotionsfach Pharmazie

Sara S. Nogueira

Johannes Gutenberg-Universität Mainz
2022

Erstgutachter:	Univ.-Prof. Dr. Peter Langguth
Zweitgutachter	Dr. Heinrich Haas

Tag der mündlichen Prüfung: 31 January 2023

Table of Contents

List of Tables

List of Figures

Abbreviations

Abstract

Messenger RNA (mRNA) has gained significant momentum over the last years since it holds the potential to prevent and treat a wide range of diseases. Although significant improvement has been made in the design of *in vitro* transcribed mRNA regarding its stability, translational capacity, and immunostimulatory potential, the therapeutic use of mRNA still requires the development of safe and potent delivery vehicles. The state-of-the-art design of the LNP for mRNA delivery remains inspired by the findings learned from the short interference RNA (siRNA) field. Moreover, the molecular coherencies and, thus, the fundamentals of LNP design, remain poorly understood, hampering the development of the next generation of clinically relevant lipid formulations.

In this thesis, the state-of-the-art design of LNP for mRNA delivery was systematically investigated by exploring the effect of different formulation and manufacturing process parameters (such as N/P ratio, manufacturing process, and lipid composition) on the formulations' physicochemical properties, morphology, and biological activity. Our results indicated that the structure of mRNA-LNP differs from those previously described for siRNA, only a 2 to 3 repeat units, presumably RNA lipid complexes, are present. Moreover, mRNA-lipid formulations can be manufactured using either the LPX or the LNP manufacturing process devoid of limited performance. More importantly, particle size, rather than manufacturing process, appeared to determine the RNA-lipid formulation biodistribution and potency. Apart from the physicochemical properties of the formulation, it was further shown that the combination with other components, such the selection of helper lipids and grafting moieties, can enable targeting beyond the liver. For the first time non-PEGylated LNP were successfully engineered; proteins, mRNA, poloxamers, and polipeptoids were used to manufacture mRNA-lipid formulations by rapid mixing techniques. Among those, pSar grafted lipids showed promising results by enabling particle size control without diminishing the activity of the formulations, opening novel possibilities for the combination of particle engineering and optimization of biological activity. To improve the performance of pSar technology, novel ionizable lipids were screened for hepatic delivery. Optimized pSar LNP improved hepatic performance and tolerability, illustrating that pSar-based nanoparticle technology is promising for the development of next-generation potent and safe RNA therapeutics for clinical translation. Finally, throughout this thesis, LNP formulations were developed for intramuscular application of saRNA vaccines against infectious diseases – an important field nowadays since the emerging pandemic. The self-replicative properties of saRNA-LNP formulations allow for lower doses to be administered, possible reducing secondary effects. Three of the thirteen *in vivo* candidates showed high antibody and neutralization titers against HA-specific antigens. Besides, the data showed promising results on intramuscular delivery of vaccines by pSar technology. An optimized saRNA LNP elicited EBOV-GP specific antibody neutralization titers, and T cell responses, and thus poses as a promising candidate for vaccination against infection diseases.

This work provides a comprehensive overview on the state-of-the-art of mRNA-lipid formulation design, which subsequently enabled the engineering of novel mRNA-lipid therapeutics with improved potency and safety.

Zusammenfassen

Die Messenger-RNA (mRNA) hat in den letzten Jahren stark an Bedeutung gewonnen, da sie das Potenzial hat, eine Vielzahl von Krankheiten zu verhindern und zu behandeln. Obwohl bei der Entwicklung von *in vitro* transkribierter mRNA hinsichtlich ihrer Stabilität, ihrer Translationsfähigkeit und ihres immunstimulatorischen Potenzials erhebliche Verbesserungen erzielt wurden, erfordert der therapeutische Einsatz von mRNA weiterhin die Entwicklung sicherer und wirksamer Transportmittel. Der aktuelle Entwicklungstand bei der LNP-Technologie für den mRNA-Transport ist von den Erkenntnissen aus dem Bereich der kurzen Interferenz-RNA (siRNA) inspiriert. Darüber hinaus sind die molekularen Zusammenhänge und damit die Grundlagen des LNP-Designs nach wie vor kaum verstanden, wodurch die Entwicklung der nächsten Generation klinisch relevanter Lipidformulierungen behindert wird.

In dieser Arbeit wurde das hochmoderne Design von LNP für die mRNA-Verabreichung systematisch untersucht, indem die Auswirkungen verschiedener Parameter der Formulierung und des Herstellungsprozesses (z. B. N/P-Verhältnis, Herstellungsprozess und Lipidzusammensetzung) auf die physikochemischen Eigenschaften, die Morphologie und die biologische Aktivität der Formulierungen erforscht wurden. Unsere Ergebnisse zeigten, dass sich die Struktur von mRNA-LNP von den zuvor für siRNA beschriebenen unterscheidet, da nur 2 bis 3 Wiederholungseinheiten, vermutlich RNA-Lipid-Komplexe, vorhanden sind. Darüber hinaus können mRNA-Lipid-Formulierungen sowohl mit dem LPX- als auch mit dem LNP-Herstellungsverfahren hergestellt werden, ohne dass die Leistungsfähigkeit eingeschränkt wird. Noch wichtiger ist, dass die Partikelgröße und nicht das Herstellungsverfahren die Biodistribution und Wirksamkeit der RNA-Lipid-Formulierung zu bestimmen scheint. Abgesehen von den physikalisch-chemischen Eigenschaften der Formulierung wurde außerdem gezeigt, dass die Kombination mit anderen Komponenten, wie z. B. die Auswahl von Hilfslipiden und Pfropfkomponenten, ein *Targeting* über die Leber hinaus ermöglichen kann. Zum ersten Mal wurden nicht-PEGylierte LNP erfolgreich entwickelt; Proteine, mRNA, Poloxamere und Polipeptoide wurden zur Herstellung von mRNA-Lipid-Formulierungen durch schnelle Mischtechniken verwendet. Die mit pSar enthaltenen Lipide zeigten vielversprechende Ergebnisse, da sie eine Kontrolle der Partikelgröße ohne Beeinträchtigung der Formulierungsaktivität der Formulierungen ermöglichten, was neue Möglichkeiten für die Kombination von Partikeltechnik und Optimierung der biologischen Aktivität eröffnet. Um die Leistung der pSar-Technologie zu verbessern, wurden neuartige ionisierbare Lipide für die Verabreichung an die Leber untersucht. Optimierte pSar-LNP verbesserten die hepatische Leistung und Verträglichkeit, was zeigt, dass die pSar-basierte Nanopartikeltechnologie vielversprechend für die Entwicklung potenter und sicherer RNA-Therapeutika der nächsten Generation für die klinische Anwendung ist. Schließlich wurden im Rahmen dieser Arbeit LNP-Formulierungen für die intramuskuläre Applikation von saRNA-Impfstoffen gegen Infektionskrankheiten entwickelt - ein wichtiger Bereich, der seit der aufkommenden Pandemie an Bedeutung gewonnen hat. Die selbstreplikativen Eigenschaften der saRNA-LNP-Formulierungen ermöglichen die Verabreichung geringerer Dosen, wodurch Sekundäreffekte reduziert werden können. Drei der dreizehn *In-vivo*-Kandidaten zeigten hohe Antikörper- und Neutralisationstiter gegen HA-spezifische Antigene.

Außerdem zeigten die Daten vielversprechende Ergebnisse bei der intramuskulären Verabreichung von Impfstoffen durch die pSar-Technologie. Ein optimierter saRNA-LNP löste EBOV-GP-spezifische Antikörper Neutralisationstiter sowie T-Zell-Reaktionen aus und stellt somit einen vielversprechenden Kandidaten für die Impfung gegen Infektionskrankheiten dar.

Diese Arbeit gibt einen umfassenden Überblick über den Technologiestandbeim Design von mRNA-Lipid-Formulierungen, die anschließend eine Entwicklung neuartiger mRNA-Lipid-Therapeutika mit verbesserter Wirksamkeit und Sicherheit ermöglichten.

.

Acknowledgements

It was a privilege to work with many brilliant and inspiring scientists during my PhD. I would like to begin by thanking my advisors Dr. Heinrich Haas, , and Prof. Dr. Peter Langguth, which supported me every step of the way, empowered me to explore my interests, and helped me to become a better scientist.

A special thanks to Prof. and Dr. for both helpful discussions and unparalleled expertise within the field.

I would like to show my gratitude for the great collaboration with Prof. Dr. and Prof. Dr. and their teams. A very special to the Peer Lab for the very welcoming environment and the great time in Tel Aviv.

At BioNTech, I had the honor to work closely with different groups and in a multitute of projects. Several people have taught me new skills, provided me guidance, helped with experiments and provide fruitful discussions over four years. I would like to specially acknowledge the Formulation group, the IDV unit, and the In vivo unit. Particularly, a special thanks

. Many of my colleagues also have become friends during this time, and therefore I want to give a special to Gaby, Isabell, Mathias, Shaheer, Erik, Janina, Konrad, and Jorge.

Finally. I want to thank my friends and finally for their unconditional love and support. ‘Pastelianos’ friends for keeping the promise of never coming back to take me back to Portugal. My parents and my little sister for being my fiercest advocates over the years. Finally, to my husband for being my rock solid helping me to maintain sanity and never let me doubt of myself.

CHAPTER 1 | Introduction

1.1 Messenger RNA Therapy

The concept of exploiting nucleic acids (NA) as a novel therapeutic modality was envisaged in 1990 when Wolff *et al.* demonstrated that direct injection of messenger RNA (mRNA) and plasmid DNA (pDNA) into the skeletal muscle of the mice mediated the expression of the encoded protein at the injection site[1]. At the time, the high instability of mRNA turned the interest of the scientific community towards the development of DNA-based therapeutics over mRNA. Nonetheless, continuous basic and applied research on mRNA's structural and functional aspects enabled recent scientific and technological advances towards overcoming associated limitations, such as its short half-life and unfavorable immunogenicity[2].

Messenger RNA transiently carries the genetic information from the DNA in the nucleus to the ribosomes in the cytosol, functioning as a template for protein synthesis[3]. Unlike pDNA, mRNA only requires reaching the cytosol to be translated into a protein of interest. Furthermore, mRNA does not pose the risk of being integrated into the host genome. Finally, the mRNA production is relatively inexpensive and straightforward via *in vitro* transcription (IVT) process[4].

The development of IVT mRNA-based therapeutics has gathered significant scientific and industrial interest over the last decades. Several pre-clinical and clinical therapeutic applications of mRNA are currently being explored within protein-replacement therapy, vaccination, and gene editing[2,5–8]. The outbreak of COVID-19 pandemic has caused severe public health, economic and social crisis across the world. The development with unparalleled speed and the effective of mRNA vaccines in the COVID disease prevention by Comirnaty® (Pfizer-BioNTech) and Spikevax® (Moderna) showed the potential application of mRNA-based therapies.

1.1.1. Fundamental Pharmacology of mRNA

The principle of mRNA therapy involves the transfer of defined genetic information into the target cells to prevent or alter a particular disease state[2]. Two distinct therapeutic approaches have been used: 1) *ex vivo* transfection of target cells that are then adoptively administrated back to the patient, and 2) direct *in vivo* delivery of mRNA using different administration routes. For both approaches, the target cell's machinery is hijacked for transient translation of the information to the corresponding protein or peptide, which is the pharmacologically active molecule inside the body (Figure 1.1-1). Thus, mRNA is designed to structurally resemble naturally occurring mature and processed mRNA in the cytoplasm of eukaryotic cells. Accordingly, IVT mRNA is a long, single-stranded ribonucleic acid molecule with a 5′

cap and a 3′ poly (A) tail, and an open reading frame (ORF) that encodes the protein of interest, which is flanked by start and stop codons, as well as 5' and 3' untranslated regions (UTRs).

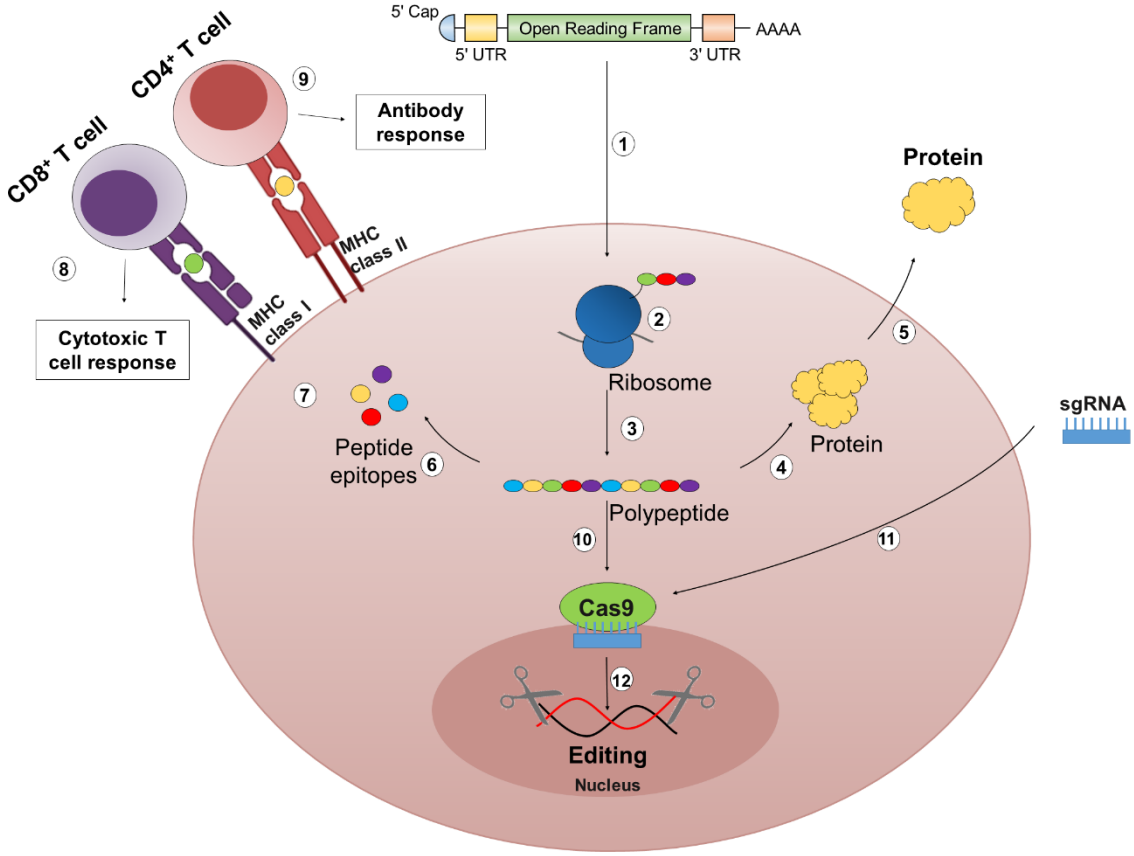

Figure 1.1-1 The pharmacology of IVT mRNA.
In vitro transcripted (IVT) mRNA contains a cap, a 5′ and 3′ UTRs, an ORF, and a poly(A) tail that determines the stability, the translational capacity, and the immunostimulatory potential of the mRNA molecule. The mRNA molecules are endocytosed by cell-specific mechanisms (e.g., macropinocytosis) reaching the cytosol of the cell (**1**). Here, mRNA molecules are recognized by ribosomes, the host's translation machinery, which initiates the elongation process by adding amino acids to the peptide chain (**2**) and terminates the process by releasing the newly synthesized peptide (**3**). Post-translational modifications convey functionality to the new protein that can be expressed intracellular (**4**) and/or secreted (**5**). Alternatively, an antigenic peptide can be processed into smaller peptide epitopes (**6**) that bind to the major histocompatibility complex (MHC) class I or class II (**7**). The MHCs are trafficked to the cell surface, where they present their antigenic epitopes to either CD8+ (cytotoxic) T cells (**8**) or CD4+ (helper) T cells (**9**), leading to cellular immunity or an antigen-specific antibody response. Lastly, mRNA can also encode for the Cas9 nuclease (**10**), which combined with the single guide RNA (sgRNA) (**11**), will form Cas9 protein complexes that are then translocated to the nucleus. The Cas9 protein complexes bind then to a specific DNA sequence complementary to the sgRNA, mediating a double-stranded DNA "cut" (**12**), which can edit the genome by deleting, replacing, or inserting a new piece of DNA. Image adapted from[2].

The IVT mRNA is synthesized in a cell-free system from a DNA template, such as a linearized plasmid or a polymerase chain reaction (PCR) product, which encodes all the structural elements of a functional mRNA. *In vitro* transcription is performed with RNA polymerases, such as T3, T7, or SP6, in the presence of nucleotides, followed by an enzymatic capping process. The template DNA is then digested by deoxyribonuclease (DNases) and purified by conventionally used methods for isolating NA (e.g., precipitation and chromatography)[4,9,10].

The pharmacodynamic activity of both native and IVT mRNA occurs in the cytosol. In contrast to natural mRNA, which is transcribed from DNA in the nucleus and transported to the cytosol via nuclear export, IVT mRNA needs to be delivered into the cytoplasm of the target cell from the extracellular space. The cytoplasm bioavailability of mRNA is dictated by extracellular ribonucleases (e.g., RNases) and by the cell membrane that hampers the passive diffusion of the negatively charged large mRNA molecule into the cytoplasm[2].

Once IVT mRNA has entered the cytoplasm, it undergoes the same cellular mechanisms that regulate the stability and translation of native mRNA. IVT mRNA is translated by ribosomes into polypeptide chains, which may then undergo post-translational modification to form the mature protein product. The pharmacokinetics of mRNA therapeutics is dictated by the half-life of the IVT mRNA template and the mature protein. Furthermore, the protein contains signal peptides, which will determine the destination of the protein. These can be either intrinsic to the natural protein sequence or recombinantly engineered to guide the protein of interest toward the host cell's desired compartment. Alternatively, the therapeutic protein may be secreted to execute in neighboring cells or released in the bloodstream to act in distant organs[2].

1.1.2. Clinical application of mRNA

Messenger RNA can be used to express in the body one or several pharmaceutically active proteins that hold the potential to treat a wide range of diseases. **Protein therapy** field includes: 1) **protein replacements** where mRNA is used to produce a missing protein or restore the function of a single protein for rare monogenic diseases[11,12]; 2) **cell programming** that involves the expression of transcription or growth factors to modulate cell behavior[13]; and 3) **immunotherapies** where mRNA is applied to induce specific immune responses against target cells or to modulate the immune system (e.g., therapeutic antibodies, cytokines)[14]. The advantages of mRNA over other therapeutic modalities include the fact that mRNA is non-infectious, non-integrating, and can be transiently translated into many copies of a protein for hours (h) or days (d), allowing a reduced schedule of administration of the drug. A myriad of studies have been performed on the protein therapy scope and comprehensively reviewed in[2,15].

Vaccination with an mRNA encoding an antigen has the potential to induce an antigen-specific immune response against cancer or infectious diseases. Nucleic acid vaccination is advantageous compared to traditional strategies since it can cause both humoral and cellular-mediated immunity (Th1 and Th2), thus preventing the infiltration of pathogens and assisting in their elimination[16]. The majority of vaccinations against viral infections and cancers using IVT mRNAs have focused on autologous dendritic cells (DCs) transfected with IVT mRNA either *in vitro* for adoptive transfer into the patient or *in vivo* by direct administration to express specific anti-tumor or anti-viral antigens (reviewed in detail[5]). The authorization of mRNA vaccines against COVID-19 emphasizes the potency of mRNA nanomedicines.

Gene editing therapy enables the replacement or alteration of gene expression by introducing site-specific modifications into the genome of the cells, including the correction of deleterious or introduction of protective mutations[17]. To this aim, mRNA encoding for the Cas9 protein and a single guide RNA (sgRNA) that guide the insertion or deletion of the gene are co-delivered into the target cells.

In comparison with other approaches, mRNA does not integrate into the genome, and it is transiently expressed, limiting the presence of nucleases inside the cells, reducing the risks of off-target cutting and immune response against Cas9 protein. *In vivo* gene-editing approach using mRNA has been directed toward the liver, lungs, and spleen[18,19]. In a study by Intellia Therapeutics, chemically modified sgRNA and Cas9 mRNA induced up to 70 % genome editing in the liver of mice[20].

1.1.3. Approaches for Enhancing mRNA Stability, Translation, and Immunogenicity

Despite the therapeutic potential of mRNA, its clinical translation is rather challenging. mRNA is a single-stranded and large molecule (300-5000 kDa ~ 1-15kb). Thereby, it is highly susceptible to degradation by 5' exonucleases, 3' exonucleases, and endonucleases[21]. Moreover, mRNA is a negatively charged hydrophilic molecule that does not readily diffuse across the cell membrane. Cell membranes are composed of zwitterions and negatively charged lipids, ion pumps, and ion channels that help to maintain a negative potential (-40 to -80 mV) of the membrane. Although some eukaryotic cells are capable of actively engulfing naked mRNA, it seems to be less than 1 out of 10,000 molecules of the initial mRNA input[2].

Exogenous mRNA is recognized by a class of pattern recognition receptors (PRRs) expressed on endosomal compartments or cytosol of mainly the innate immune system cells[22]. Single-stranded RNA is recognized through toll-like receptors (TLR), such as TLR7 and TLR8, located in the endosomes[23,24]. TLR3 is activated by secondary structures of RNA and double-stranded RNA (dsRNA) fragments introduced as contaminants during the IVT mRNA production process [25]. Additionally, dsRNA can be recognized by the cytosolic RNA sensors retinoic acid-inducible gene I (RIG-I) and melanoma differentiation-associated protein 5 (MDA5)[26–28]. The binding of mRNA molecules to these RNA sensors leads to downstream signaling resulting in the production of type I interferon (IFN) and other pro-inflammatory cytokines (e.g., IL-6 and TNF-α) and, finally, the inhibition of mRNA translation[29].

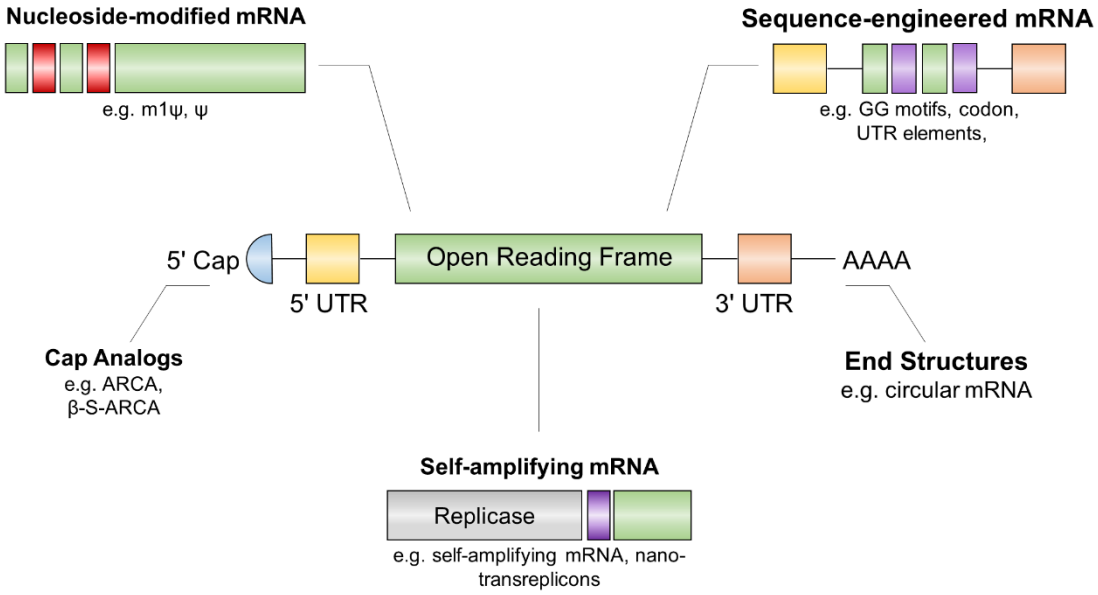

Figure 1.1-2 Structural features of IVT mRNA.
The figure illustrates the structural elements, such as Cap, sequence, and end structures that can be optimized and modified to modulate the profile of mRNA. Adapted image[2,30].

For the purpose of using IVT mRNA as a therapeutic drug, several modification strategies have been implemented to optimize mRNA stability, translation, and immunogenicity[2,30,31]. Strategies included modifying the 5′ cap, elongation of poly(A)-tail, optimization 5′- and 3′-UTRs, incorporation of modified nucleotides and, engineering of pattern sequence in the ORF.

Incorporation of modified nucleotides in the mRNA, and hence **nucleoside-modified mRNA**, improved the protein expression and avoided recognition by the immune system. Karikó and colleagues showed that the presence of modified nucleotides in the mRNA construct, such as methylated nucleosides or pseudouridine, strongly reduced the immune-modulatory capacity of exogenous mRNA[9].

Sequence optimizations, termed **sequence-engineered mRNA,** in the ORF and UTRs of IVT mRNA, including enrichment in the guanine-cytosine (GC) content, the introduction of two beta-globin 3'-UTR aligned in a head-to-tail configuration, or condon optimization has been introduced to boost the mRNA expression[32]. Besides, anti-reverse cap (ARCA) modifications with one 3'-OH group instead of two 3'-OH groups (ARCA; $m_2^{7,3'}$-oGpppG) were incorporated to prevent the incorporation of ARCA in opposite orientation at the 5' end[33]. Other cap modifications, e.g., phosphorothioate, locked nucleic acid, and other cap analogs, provide the mRNA with resistance to decapping by the mRNA-decapping enzyme 2, leading to a longer half-life of the mRNA[34]. Furthermore, a gradual increase in poly(A) tail length has also been shown to improve the efficiency of polymersome generation, thus the level and duration of protein expression. Moreover, the poly (A) tail also plays a role in preventing decapping and mRNA degradation. Specific modifications at the 3' UTR can reduce the decay of the poly(A) tail by deadenylation[35,36].

Another strategy designed to increase RNA translation is based on **self-amplifying mRNA (saRNA) or replicons**[37,38]. The replicon constructs contain an additional ORF, which encodes proteins for the RNA-dependent RNA polymerase (viral replicase) combined with the ORF, which encodes structural proteins. The viral replicase drives the amplification of mRNA intracellularly, which results in higher protein expression[38]. Johanning *et al.* demonstrated that local application of saRNA mediated a ten-fold improvement in protein expression levels from up to 10 days compared to (non-amplifying) mRNA[37].

Alternative approaches have been proposed to improve the half-time of mRNA[15,39,40]. For example, circular RNA could mediate up to a 3-fold improvement in protein expression compared to linear RNAs (non-modified and modified) *in vitro*[15]. Purification of mRNA with High-Performance Liquid Chromatography (HPLC) helped to reduce the amount of dsRNA contaminant minimizing the immunogenicity of the IVT mRNA[10].

Despite the strategies developed to overcome the limitations of synthetic mRNA, its encapsulation into delivery vehicles is required for safe and potent mRNA delivery. Viral (alphaviruses, picornaviruses, and flavivirus) and non-viral methods (lipid or polymers) have been developed to improve mRNA delivery *in vivo*. However, the limited cargo size, integration risk, off-target editing, immune reaction, high cost, and manufacturing limitations of viral vehicles hinder their usage in clinical translation despite their high efficiency.

1.2 Lipid-based Systems for RNA Delivery

Lipid-based nanocarriers are the most advanced non-viral systems for drug delivery[41]. In the 1960s, Alec Bangham inspired the drug delivery field when he first reported on vesicular structures formed by a mixture of phospholipids (lecithin) extracted from egg yolk. These mixtures, when hydrated, resulted in lamellar structures capable of maintaining ion concentration. Initially designated "Banghasomes", those lipid bilayers enclosing a water compartment became known as liposomes in 1968[42,43]. Although liposomes were first introduced as membrane model systems, the discovery of their ability to entrap biologically active compounds unveiled their potential for the drug delivery field[44,45].

Liposomes can incorporate a wide variety of therapeutic molecules, from small molecules to NA[46,47]. Liposomes shield them from degrading enzymes, improve their pharmacokinetic profile, and enhance drug targeting toward specific tissues. Several liposomal formulations (e.g., AmBisome®, DOXIL®) have been approved for human use (reviewed in detail[48]). Nevertheless, the application of cationic liposomes to the delivery of nucleic acids (e.g., short interference RNA (siRNA), pDNA, mRNA) have been limited by the lack of colloidal stability, poor potency and tolerability issues. A breakthrough in the development of lipid-based formulations for nucleic acids was the development of ionizable cationic lipids[49]. Ionizable lipid-based lipid nanoparticles are currently the most advanced vehicle for the delivery of NA, as demonstrated by the approval of Onpattro® for treatment of Amyloidosis in 2018[50].

1.2.1. The Lipid Mesophases

Lipids are amphipathic molecules that self-assemble in water into structures or mesophases to minimize the exposure of the hydrocarbon chains to the water (see Figure 1.2-1). In 1975, Israelachvili and colleagues proposed that liposomes have a critical packing parameter (PP*)* between 1/2 and 1[51]. This parameter describes the geometry of the lipid as the ratio between the surfactant tail volume *(V)* and the effective area per molecule at the interface (*a)* and the surfactant tail length *(l)*. These mesophases are thermodynamically stable and are determined by temperature, concentration, pH, and the packing constraints of the individual lipid molecules[52].

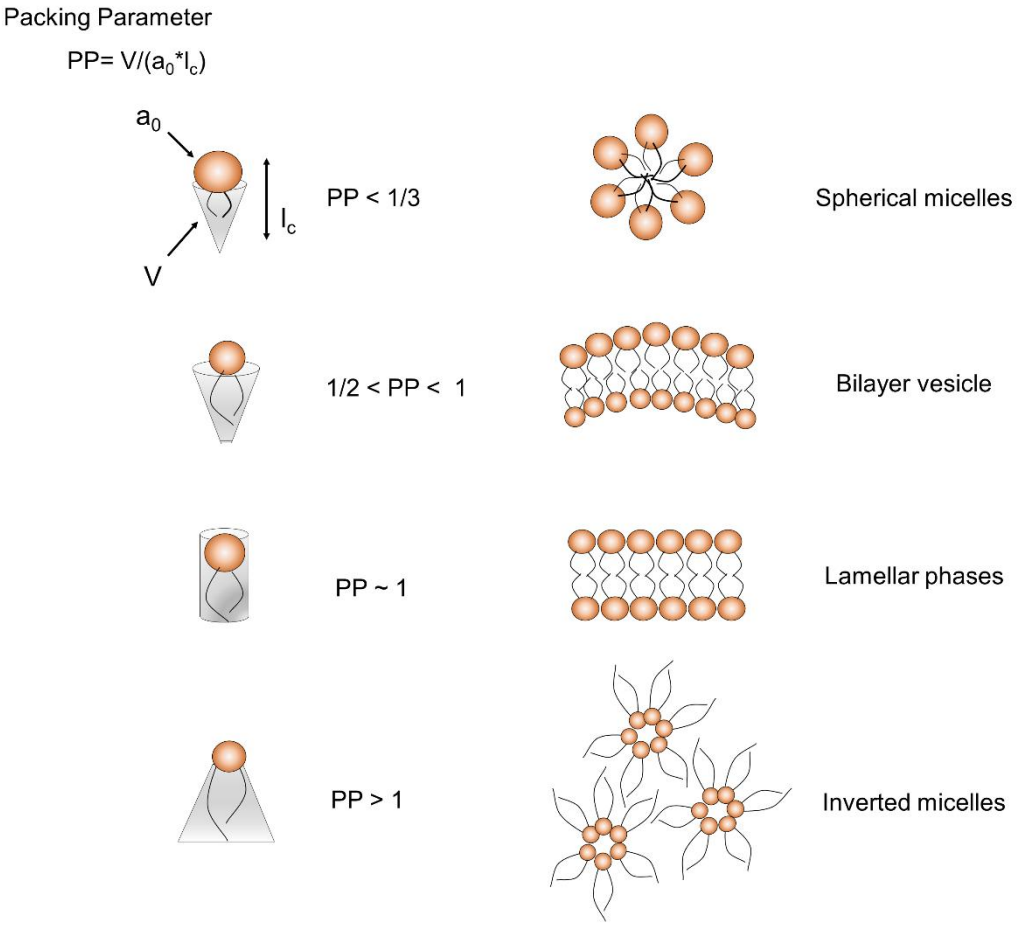

Figure 1.2-1 Lipid mesophases as a function of the molecular shape and critical packing parameter (PP) of amphiphilic lipid molecules.
Adapted image[53].

Lipids with packing parameters between 1/2 and 1, with a similar area of the polar head and the hydrocarbons chain, form the lamellar liquid crystalline structure (L_α). The cell membrane is an example of lipids' self-assembly in nature, where a lamellar mesophase is formed due to the high composition of phospholipids such as phosphocholines (PC)[54]. When amphiphilic lipids have a large polar head relative to the hydrophobic chains (P<1/3), the self-assembly results in type I structures such as micelles (L_1) and hexagonal phases (H_1). On the other hand, lipids that display a small polar head and a large hydrocarbon chain, P>1, adopt structures type II or inverse structures, such as reverse hexagonal (H_2) and reverse micelles (L_2). The reverse hexagonal is a destabilizing non-bilayer structure that is crucial in biological processes involved in the delivery of nucleic acid into the cytosol[55].

1.2.2.History of RNA Nanocarriers: From Liposomes to Lipid Nanoparticles

Early attempts to load nucleic acids into neutral **liposomes** resulted in poor encapsulation efficiency[56]. Still, Dimitriadis was able to report first in 1978 the delivery of mRNA encoding rabbit globin when loaded into large phosphatidylserine (PS) liposomes, prepared by thin-film hydration and sonication, to mouse splenocytes. To improve the encapsulation efficiency, positively charged lipids, such as N-[1-(2,3-dioleyloxy)propyl]-N,N,N-trimethylammonium chloride (DOTMA), were developed to promote the electrostatic binding to negatively charged nucleic acids. In 1989, Malone and colleagues

first demonstrated that cationic liposomes composed of cationic DOTMA and the helper lipid dioleyl phophatidylethanolamine (DOPE) mediated successful transfection of pDNA and mRNA into NIH 3T3 mouse cells[57]. These complexes termed ‘‘**lipoplexes (LPX)**,’’ were unstable and characterized by broad size distributions ranging from the submicron scale to a few microns[58].

In the 1990s, pre-clinical exploration of nucleic acids was initiated for diverse applications[59,60]. The high instability of mRNA turned the interest of the scientific community toward the development of liposomes for pDNA, antisense oligodeoxynucleotide (ODN), and siRNA[61–63]. For example, Buyens *et* al reported on liposomes manufactured by hydrating a lipid film of 2-Dioleoyl-3-trimethylammonium propane (DOTAP), DOPE and 1, 2-Distearoyl-sn-glycero-3-phosphoethanolamine-Poly(ethylene glycol (DSPE-PEG) (47.5/47.5/5 mol %) with a solution of siRNA in 4-(2-hydroxyethyl)-1-piperazineethanesulfonic acid (HEPES), resulting in particles with sizes ranging between 80 to 300 nm, with encapsulation efficiency up to 43 %. It was postulated that the cationic lipid is equally distributed among the bilayer, and thereby half of the cationic lipid complexed with siRNA is located in the interior core of the liposome, whereas the other half is located at the surface, resulting in low encapsulation efficiencies[63].

The high positive net charge of permanently cationic lipid/liposomes was also further associated with cellular toxicity, non-specific interaction with blood and immune system components, and rapid plasma clearance[64]. The drawbacks of permanently cationic lipids lead to the development of non-permanently charged cationic lipids (also denominated ionizable lipids or ionizable cationic lipids). Ionizable lipids are characterized by an amine group with an apparent acid dissociation constant (p*K*a). At physiological conditions (pH > pK_a), the net charge of the lipid is rather neutral, resulting in improved circulation and biocompatibility. While in an acidic environment (pH < pKa), the ionizable lipids are positively charged, enabling the complexation of negatively charged nucleic acid.

In 2001, Semple *et al.* reported on the first ionizable amino-lipid 1,2-dioleoyl-3-dimethylammonium-propane (DODAP) to deliver ODN, which consisted of a tertiary amine linked to two oleyl chains, via diester linker. Moreover, the authors demonstrated that by adding 40% ethanol during lipid-film hydration of lipid mixture containing distearoyl-sn-glycero-3-phosphocholine (DSPC)), cholesterylhexadecylether (CHE)), DODAP, and 1-O-(2P-(w-methoxypolyethyleneglycol)succinoyl)-2-N-myristoylsphingosine (PEG-CerC14) at molar ratios of 25/45/20/10 mol %, the encapsulation efficiency could be improved up to 70 %, termed as stabilized antisense-lipid particles (SALP). This procedure is mentioned as a preformed vesicle method, which was further simplified by mixing a lipid mixture dissolved in 100 % ethanol with a buffer solution containing oligonucleotides[49].

Meanwhile, improved control was achieved over the mixing process (further describe in section 2.3). In 2005, stabilized plasmid lipid particles (SPLPs) formulated with a lipid mixture of Chol, DSPC, 1,2-dioleyloxy-3-dimethylamino-propane (DODMA), and PEG-succinoyl distearylglycerol (PEG-S-DSG) at molar ratios of 55:20:15:10 was mixed with pDNA in T-shaped mixing chamber. The SPLPs exhibited sub-200 nm particles and encapsulation efficiencies higher than 80 %[65]. This method was subsequently adapted for encapsulation of siRNA payloads, termed stable nucleic acid lipid particles (SNALP), yielding sub-100 nm with high encapsulation efficiencies (>90%)[66–68]**.**

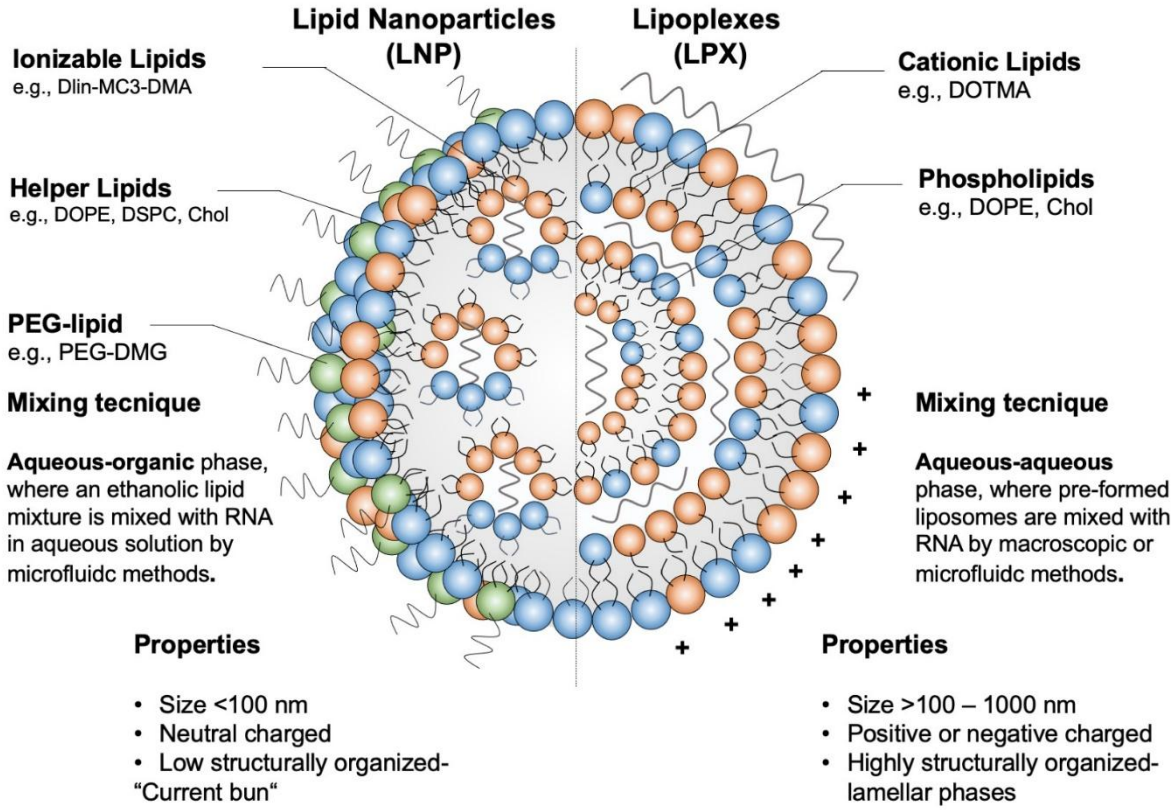

Figure 1.2-2 Schematic representation of lipid formulations.

Several years later, SNALPs were employed for self-amplifying RNA[69] These systems were prepared by in-line mixing of equal volumes of lipids dissolved in ethanol and mRNA in 100 mM citrate buffer (pH 6) through a T-Junction[69]. Only in 2015, Pardi *et al.* reported on SNALP systems for mRNA delivery to the liver[70]. Similarly, these were composed of previously described ionizable lipids[71,72], in combination with DSPC, Chol, and polyethylene glycol (PEG)-lipid at a molar fraction of 50:10:38.5:1.5 mol % and assembled by mixing an aqueous solution of mRNA at pH 4 with a solution of lipids dissolved in ethanol by the rapid mixing process[70].

Since then, SNALP, or as now commonly denominated **lipid nanoparticles (LNP)**, have been showing promising results for pDNA, siRNA, and mRNA delivery in preclinical[73–75] and clinical studies (reviewed in detail[41]). The mechanism of LNP formation is based on the precipitation of lipids as the solvent polarity increases upon dilution of the ethanol phase in the aqueous phase[76]. Typically, LNP is composed of ionizable lipid, helper lipids (phospholipid and chol), and PEG-lipid, which when produced by rapid mixing display sub-100 nm and neutral surface charge, RNA encapsulation efficiencies above 90 %, and electron-dense core[77].

In 2018, the first LNP comprising an ionizable lipid D-Lin-MC3-DMA or MC3 (Heptatriaconta-6,9,28,31-tetraten-19-yl 4-(dimethylamino) butanoate) was approved for the delivery of siRNA for the treatment of Amyloidosis in the USA and EU. More recently, the first mRNA-based LNP vaccine (Comirnaty®) was approved for COVID-19[78]. Several new LNP formulations are being evaluated in the pre-clinical and clinical settings for a broad range of diseases[41].

1.2.3.Manufacturing of Liposomes and Lipid Nanoparticles

Lipid-based delivery systems can be produced by different manufacturing methods; however, these methods can be divided into either aqueous-aqueous mixing or ethanol-aqueous mixing. In the case of aqueous-aqueous mixing, the mixing occurs between preformed lipid vesicles with mRNA in an aqueous environment. In this case, lipid vesicles have been previously prepared using conventional methods, such as lipid-film hydration followed by size reduction or ethanol injection methods. On the other hand, the ethanol-aqueous mixing implicates the mixing between an ethanolic lipid phase with an aqueous solution of mRNA by rapid mixing technologies (e.g., T-tube mixing, microfluidic hydrodynamic focusing (MHF), and staggered herringbone mixer (SHM)).

Liposome production

The thin-film hydration method is considered to be one of the most practical methods to yield small and uniform liposomal particles. In the thin-film hydration method, lipids are dissolved in an organic solvent and transferred to a steel production vessel or a round-bottom flask. The solvent is then removed under evaporation, and a thin film is produced on the surface of the flask. When this thin film is hydrated with an aqueous solution, a heterogeneous population of large multilamellar vesicles is formed with a size distribution around several micrometers[79,80]. Size-reduction methods, such as extrusion and sonication, are then implemented to produce a homogenous particle suspension with a defined particle size. Extrusion consists of repeatedly forcing a heterogeneous suspension of particles through a polycarbonate or inorganic filter with a determined size pore. This process results in a homogenous population of unilamellar vesicles, with monodisperse particle size in the range of the pore size[79,81]. On the other hand, sonication reduces the particle size using acoustic energy from either a probe tip sonicator or a bath sonication. Vesicles prepared by sonication may be either unilamellar or multilamellar, with the particle size strongly depending on the lipid composition and the time of sonication. In comparison with the extrusion method, the sonication process is less time-consuming; however, the liposome batch-to-batch reproducibility is lower[82]. Alternatively, high-pressure homogenization can be employed to reduce particle size using high-pressure machines (e.g., French pressure cell) or with an interaction chamber where two fluids collide (microfluidization)[80,83]. In microfluidization, the liposomal suspension is pumped at high velocity through an inlet divided into two streams and progressively bifurcates. These streams eventually collide within an interaction chamber leading to the formation of smaller particles due to extreme conditions of turbulence and pressure[83,84].

The ethanol injection technique was developed as an improved alternative to the thin-film hydration method combined with sonication. In this process, an ethanolic solution of lipids is rapidly injected into an aqueous medium through a needle, promoting lipid vesicles self-assembly due to a rise in solvent polarity. The cross-flow injected method consists of a cross-flow module where a lipid solution dissolved in ethanol is injected by two perpendicular stainless-steel tubes into a stream of an aqueous buffer resulting in the formation of liposomes. Thereby, particle size is influenced by the flow rates and injection pressures; particle size is reduced with higher flow rates of the aqueous buffer streams at higher injection pressures of the ethanol solution containing lipids[85].

The RNA-lipid nanoparticles manufactured by aqueous - aqueous mixing are labor-intensive and multi-staged processes that typically lack scalability and reproducibility[79]. Nevertheless, these

methods remain popular because they are inexpensive, easy to implement, and executed at a laboratory scale without preventing large-scale production[86].

Rapid-Mixing Technologies

Several improved strategies for RNA lipid nanoparticles production are based on the ethanol injection method. In 1999, Hirota *et al.* described, for the first time, the use of T-junction mixing to produce DNA-lipoplexes[87]. It consisted of two input streams, which collide in a T-junction resulting in a turbulent output flow. This process provided an alternative controlled mixing environment compared to macroscopic mixing methods leading to the reproducible production of lipoplexes[87,88]. The resulting particle characteristics depend on operating controls (e.g., flow rate (FR) and flow rate ratio (FRR)). T-junction technique requires high flow rates to ensure rapid mixing, and therefore, its implementation is limited in routine laboratories but preferred by companies for large scale production of LNP[89].

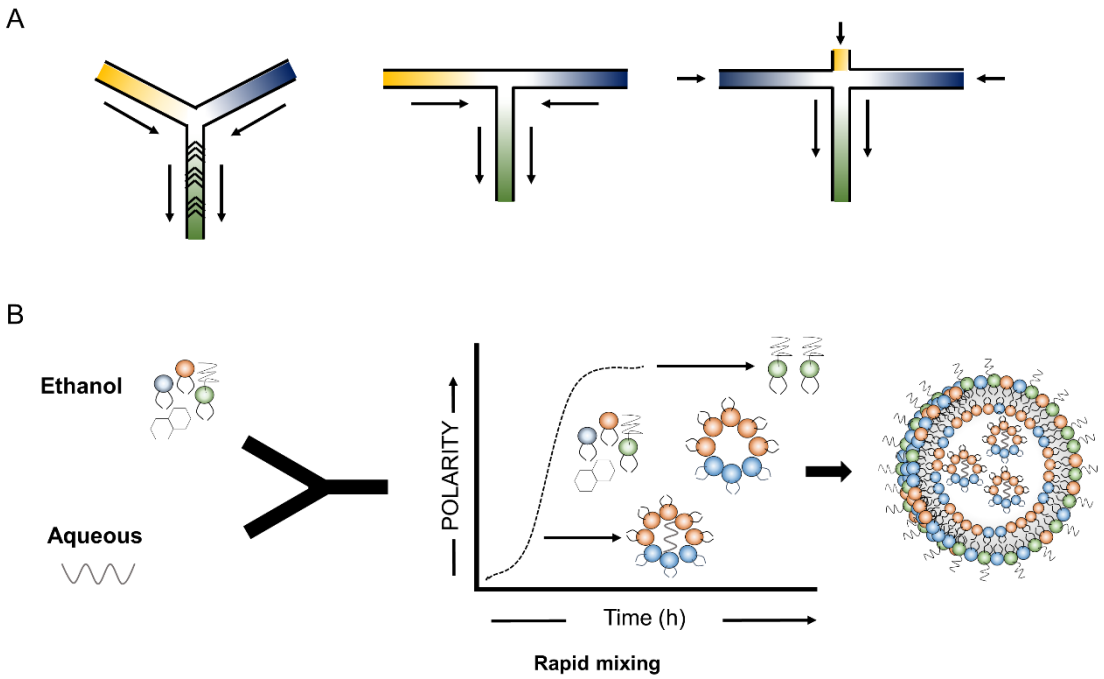

Figure 1.2-3 Types of rapid mixing and ethanol loading mechanism for LNP formation containing nucleic acids.
A)Types of rapid mixing structures, such as SHM, T-junction, and MHF mixers. B) Lipids in ethanol are rapidly mixed with nucleic acids in an acidic aqueous buffer. The lipid mixture is composed of ionizable lipids (orange headgroup), Chol, DSPC (blue headgroup), and PEG lipid (green headgroup). On mixing, electrostatic interactions drive the formation of an inverted micelle containing the RNA surrounded by predominantly ionizable lipid and DSPC that drops out as the polarity increases. If the mixing occurs rapidly, these inverted micelles are coated by PEG lipids that precipitate at higher polarity to surround the inverted micelles. Adapted image[89,90].

An alternative setup to the T-junction mixing is the microfluidic hydrodynamic focusing (MHF) technique. In this technique, the mixing is characterized by a laminar flow, where the mixing occurs by convection-diffusion processes resulting in a relatively slow process. Thus, the length of the channel and the contact surface area of the two streams determine the degree of mixing[91,92]. Jahn *et al.* firstly reported on the MHF technique to produce liposomes with 100 to 300 nm[93]. Here, the microfluidic is composed of three inlets, where the core flow containing the sample (lipids in ethanol) is sheathed by two side streams of an aqueous solution. Besides other factors, operating parameters, such as the flow

rate and flow rate ratio can be used to control particle size[94]. Despite few reports on its use for the preparation of RNA-based lipid nanoparticles, the application of such mixing is limited[89].

Alternatively, staggered herringbone mixing was developed by Stroock *et a*l. and described by the Cullis group for the preparation of RNA-loaded LNP[95,96]. The geometric patterns (e.g., arrays of herringbones) induce transversal flow components that stretch and fold volumes of fluid over the cross-section to produce chaotic advection. The SHM technique improved the control over the mixing process and shortened the mixing time[97]. Shorter mixing times decreased mass-transport effects, which are known to cause lipid aggregation and heterogeneous particle populations[95]. Geometry, and operating parameters can also be used to manipulate particle size and size distribution. Another advantage is that SHM mixers can be easily scaled up by the parallelization of microfluidic chips[98].

Lipid nanoparticles have been massively produced using SHM mixers or SHM-based commercially available devices. Multiple reports demonstrated the effect of geometry, operating parameters, lipid composition on physicochemical properties, e.g., particle size, structure, and RNA encapsulation efficiency (reviewed in detail[89]).

The development of rapid-mixing methods facilitated the clinical translation and commercialization of LNP. However, significant drawbacks have been associated with rapid mixing techniques, such as the incorporation of substantial amounts of organic solvent in the manufacturing process, limited solubility for determined lipids resulting in LNP with low concentrations, and incompatibilities of the solvents[99].

1.3 State-of-the-Art of Lipid-RNA Formulation: Overview and Challenges

The surface properties of lipid nanoparticles play an essential role in overcoming biological barriers, such as tissue barriers, immune system recognition, non-specific distribution, cell membrane internalization, and endosomal escape[100]. The choice of the lipid composition, manufacturing procedure, charge, and size are critical in the design of lipid nanoparticles for a specific tissue or disease treatment.

Several types of lipids, such ionizable lipids, phospholipids, PEG-lipids, and cholesterols have been used for LNP design (Figure 1.3-1).

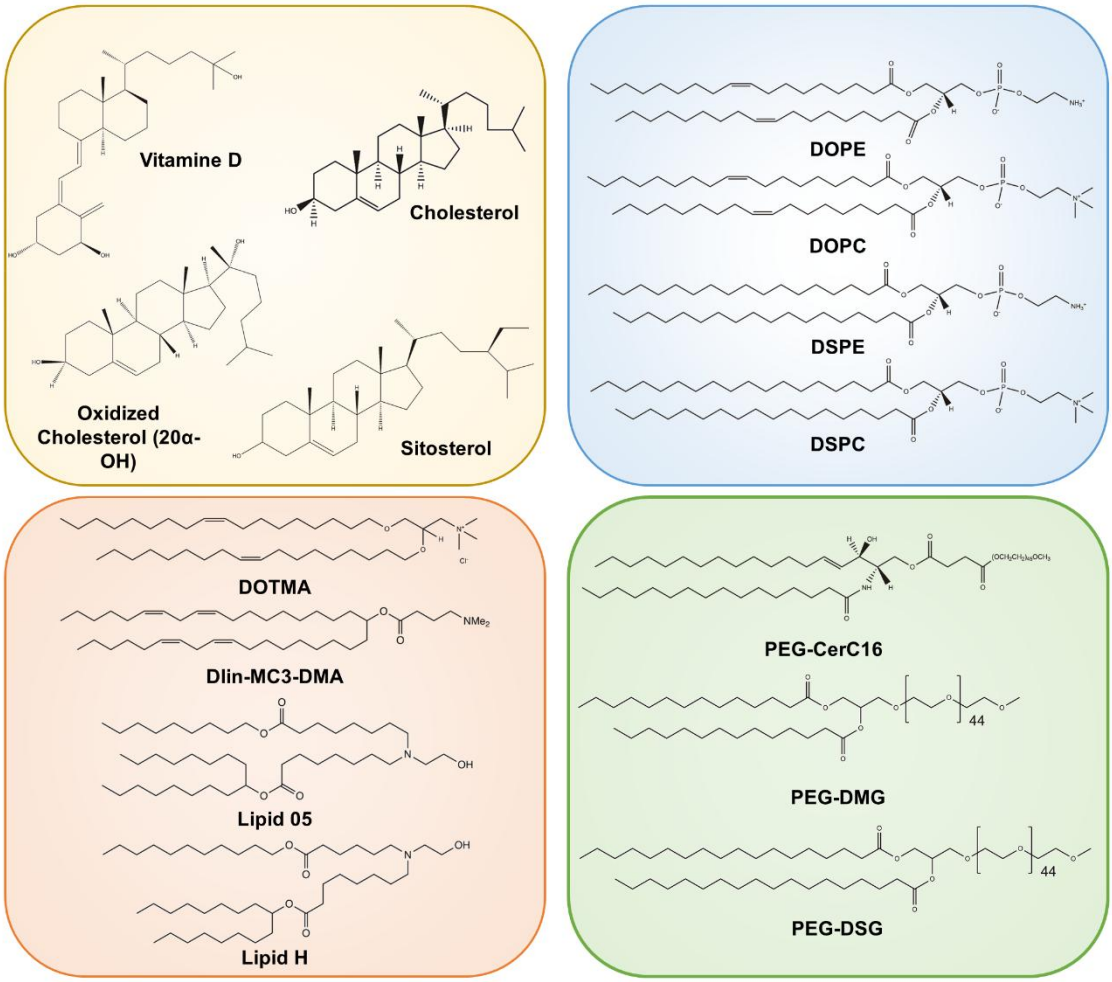

Figure 1.3-1 Representative structures of various classes of lipids used to formulate the lipid nanoparticles for mRNA delivery in pre-clinical and clinical settings.

The **ionizable cationic lipid** drives efficacy and toxicity. Rational approaches have been employed in the design and synthesis of ionizable amino-lipids to elucidate the structure-activity relationship (SAR)[66]. Novel lipids were synthesized with rational design approaches by systematically varying the lipid head and tail structures (e.g., 2-[2,2-bis[(9Z,12Z)-octadeca-9,12-dienyl]-1,3-dioxolan-4-yl]-N,N-dimethylethanamine (Dlin-KC2-DMA or KC2), MC3, L319), The degree of unsaturation of the alkyl chain, the type and length of the linker group, and the pK_a of the lipid determined the hepatic gene silencing[72,101]. Recently, a biodegradable ionizable lipid (lipid 05), developed by Moderna Therapeutics, mediated higher mRNA expression in non human primates (NHPs) compared with MC3 lipids. The incorporation of a primary ester on one of the hydrophobic tails of lipid 05 improved liver clearance, whereas the terminal alcohol on the head group enhanced the transfection potency[102,103]. Hasset *et al*. reported on optimal immunogenicity and tolerability of LNP formulated with lipid H for IM (intramuscular) administration of mRNA vaccines. The ionizable lipid pKa for optimal immunogenicity upon IM administration was 6.6-6.8[104], contrary to the previously reported of pKa 6.2-6.4 for liver expression upon intravenous (IV)) administration[66,103,105]. Lipid H corresponds to ionizable lipid SM-102 in Moderna's SARS-CoV-2 vaccine product mRNA-1273.

Other materials were discovered by creating large combinatorial libraries of lipid-like materials, also denominated lipidoids (such as C12-200, cKK-E12, OK-02). A diketopiperazine-based ionizable

lipid, cKK-E12, initially developed for siRNA, has shown high transfection efficiency in different immune cell populations, including dendritic cells, macrophages, neutrophils, and B cells[106–108]. The incorporation of double bonds in the fatty acid chains to cKK-E12 structure gave origin to the lipid designated OF-02, which improved the mRNA expression in the liver compared to cKK-E12[109]. These results corroborated the earliest findings, where it was demonstrated that unsaturated lipid tails introduce structural defects that might facilitate the fusion of the LNP with the lipid bilayers, and thus promoting endosomal escape[110]. A further biodegradable ester version of OF-02, named OF-Deg-Lin, was shown to promote selective mRNA expression in B lymphocytes in the spleen. In contrast, the non-biodegradable OF-02 promoted expression in mouse liver[111].

Helper lipids (e.g., Chol, DSPC, DOPE) are typically included in lipid nanoparticles to provide membrane integrity and potency[112]. The helper lipids preferentially used in LNP technology are Chol and DSPC lipids. Chol is used as a stabilizing agent; it fills up the gaps between phospholipids improving packing density[113], and thereby, improves stability in the presence of serum proteins and promotes membrane fusion. DSPC has saturated aliphatic chains and a high melting temperature phase (T_m)), and favors the formation of bilayer phases, which allows higher lipid bilayer stability[114,115]. A significant drawback of PC is the incapability of fostering endosomal escape and RNA disassociation[112]. Early liposome designs incorporated DOPE instead of DSPC, since DOPE has unsaturated aliphatic chains and a low melting temperatures phase, and also promotes the bilayer hexagonal phase[116]. Du *et al.* showed that DOPE promotes substantially higher transfection efficiency *in vitro* and *in vivo* than those formulated with PC[117]. Additionally, DOPE is the helper lipid of choice in lipidoid-based LNP (e.g., C12-200) formulated with mRNA since it may reduce the membrane stability, resulting in a looser complexation of the mRNA, thereby promoting endosomal escape of mRNA and release into the cytosol[106]. Unsaturated PC, such as 1,2-dioleoyl-sn-glycero-3-phosphocholine (DOPC) have been incorporated in LNP designs with limited success[106]. DOPC exhibit low T_m values and thus results in LNP highly susceptible to serum protein opsonization but favors formation of bilayer structures[118]. DOPC-based LNP are less stable than DSPC-based nanoparticles, but more stable than DOPE-based formulations, which may reduce the compromise between stability and efficacy[112].

Anionic lipids have been included in lipid formulations to confer a pH-responsive zeta potential profile due to the ion pairs formation with cationic lipids[119]. Non-pH sensitive anionic lipids, such as phosphatidylglycerol (PG), can balance the charges of a pH-sensitive cationic lipid, typically a tertiary amide-based cationic lipid. In another approach, cationic or anionic lipids such as negative phospholipid 1,2-dioleoyl-sn-glycero-3-phospho-L-serine (DOPS), 1,2-distearoyl-sn-glycero-3-phosphate (18PA), DOTAP, have been used to modulate the fate of the lipid nanoparticles[19,59,120,121].

Recently, modified cholesterols have been investigated for mRNA delivery. For example, Patel *et al.* investigated the substitution of Chol with Chol analogs in the structure-activity of mRNA-LNP. This report showed that incorporating C-24 phytosterols in LNP (eLNP) enhanced cellular uptake and retention, resulting in higher transfection efficiency[122]. In addition, Paunovska *et al.* showed that oxidized cholesterols could deliver gene-editing mRNA to the liver microenvironment. Moreover, the position of the oxidative modification in cholesterol plays a crucial role in efficacy; cholesterols modified on the hydrocarbon tail associated with sterol ring D tend to outperform cholesterols modified on sterol ring B[123].

Stealth lipids have been incorporated into lipid-based delivery systems to reduce the opsonization and clearance of lipid nanoparticles by the mononuclear phagocyte system[124]. One common approach is to provide steric hindrance effect by incorporating PEG-conjugated lipids at the surface of the particle[125]. PEGylation of nanoparticles prevents inter-particle fusion/aggregation during particle formation and storage, provides longer circulation time, and determines the particle size[126]. However, the PEGylation of nanoparticles can also have substantial disadvantages concerning activity and safety, which is named the “PEG dilemma”. PEGylation may lead to the lowering of the transfection potency by hindering cellular uptake and processing[127]. Recently, PEG has also been associated with the accelerated blood clearance (ABC)phenomenon, induced by the formation of anti-PEG antibodies following repeated systemic administration[128–132]. These anti-PEG antibodies are typically found in healthy humans due to increased exposure to PEG-containing products, such as cosmetics[131,133]. PEG has been shown to trigger complement activation, which can lead to hypersensitivity reactions, also known as Complement-Activation Related Pseudo-Allergy (CARPA) in specific individuals[134,135].

Lipid nanoparticles are typically formulated with PEGs with shorter alkyl chains (C8-C14), such as 1,2-Dimyristoyl-rac-glycero-3-methylpolyoxyethylene (PEG-DMG), at low molar content (1-2 %) to confer exchangeable properties and promote cell interaction followed by the release of the mRNA in the cytosol. In addition, cleavable linkers sensible to reduction or interstitial protease may allow reversible PEGylation[136]. Although there have been improvements, **safety** concerns are still present in PEGylated LNP[137,138].

Novel moieties, such as poly(glycerol), poly(oxazolines), sugar-based systems, and poly(peptide)s, have been investigated as PEG alternatives for drug delivery[139–141]. Polysarcosine (pSar), a polypeptoid made of repetitive units of the endogenous amino acid sarcosine (N-methylated glycine), has emerged as a promising alternative to PEG since it showed comparable stealth-like properties[142–149].

Lipid nanoparticles tend to naturally accumulate in the liver, resulting from the adsorption of serum proteins, predominantly apolipoproteins, on the surface of the LNP following their IV administration[150]. This apolipoprotein-enriched protein corona can be determined by the LNP surface properties[151,152]. The pH-dependent charge of ionizable lipid and PEG-lipid confer a neutral charge to the LNP in circulation and drives specific interactions with apolipoprotein E (ApoE), facilitating their endocytosis via the low-density lipoprotein (LDL) receptor into the hepatocytes[150].

Further studies suggested the involvement of distinct uptake mechanisms depending on the lipid composition[153,154]. The ionizable-based LNP (MC3) was internalized by clathrin-mediated endocytosis (CME) and macropinocytosis, with micropinocytosis being the primary mechanism in Hela cells[153]. In contrast, lipidoid-based LNP (e.g., C12-200) was mainly internalized by macropinocytosis pathway[154].

Following cellular internalization, the LNP performance is still dependent on escaping the endosomal compartments to avoid enzymatic degradation and the release of the RNA cargo into the cytoplasm. The main hypothesis is that upon acidification of the endosome, the ionizable lipid becomes positively charged and interacts with counter-charged anionic lipids of the inner endosomal membrane via ion-pairing. This lipid pairing promotes the formation of non-lamellar phases, such as reversed

hexagonal phases, resulting in the destabilization of endosomal membranes and the release of RNA in the cytosol[155].

It is estimated that less than 3 % of the siRNA loaded into the internalized LNP is released into the cytosol, where the rest of siRNA is mainly exocytosed via a recycling pathway regulated by a Niemann Pick type C1, a late endosomal/lysosomal membrane protein or subject to lysosomal degradation and other non-productive pathways[153,154]. In the case of mRNA-based LNP, the percentage of mRNA released from endosomes is up to 15%, depending on the ionizable lipid fusogenicity[103,153,156].

Research groups have been developing new strategies beyond the ionizable lipid design to improve RNA endosomal escape[106,157]. Fusogenic lipids, such as DOPE, have been included in formulations to optimize the formation of non-lamellar structures and mediate higher mRNA release[106]. In another approach, Wang *et al.* showed enhanced intracellular uptake and colocalization of siRNA-LNP in cell lines upon administration of inhibitor of Niemann-Pick type C1 compound NP3.47[157].

Other organs or tissues **beyond the liver** have proved to be more challenging to reach[158]. Enormous efforts have been made to overcome the extrahepatic targeting limitation by passive targeting approaches by relying on high-throughput screening of formulations[66,159,160]. Physicochemical characteristics, such as size, surface charge, and shape**,** have been shown to modulate the nanoparticle fate and localization following IV administration[100,161]. Recently, Chen and colleagues showed that when a selective organ targeting (SORT) molecule, positive and negative lipid, is included in lipid nanoparticles can selectively edit therapeutically relevant cell types in the lung, and spleen, respectively[19]. As an alternative, sub-100 nm particles display longer circulation times and tend to accumulate in the liver and tumor[162], while bigger particles tend to accumulate in the lungs and spleen[100].

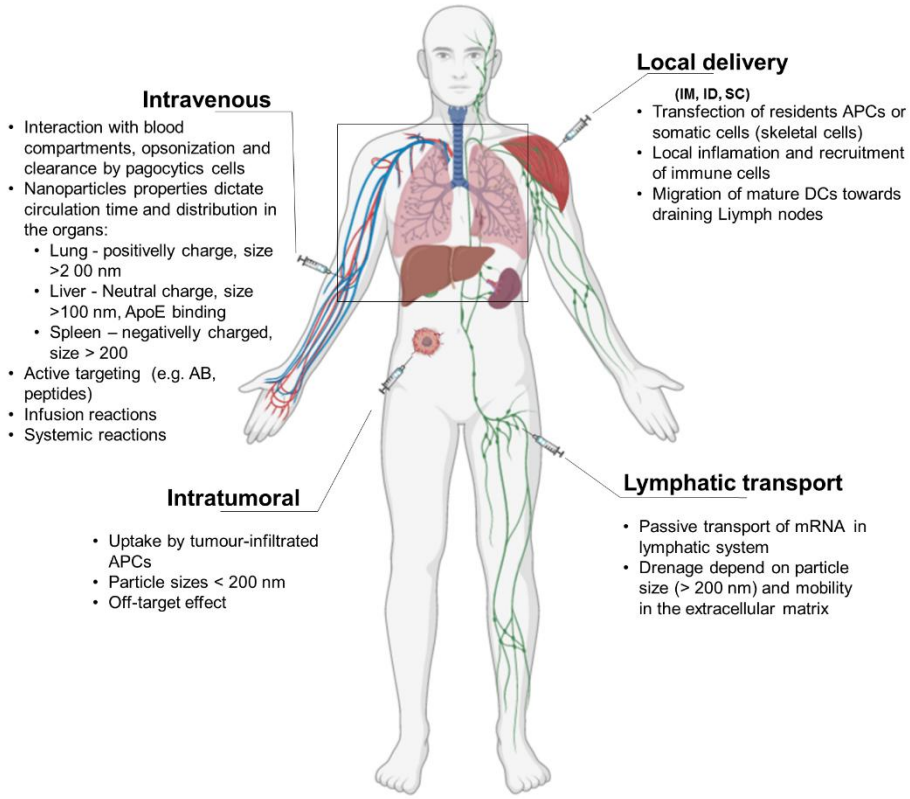

Figure 1.3-2 Administration routes for mRNA-lipid nanoparticles.
Adapted image[30].

Alternative administration routes have also been used to deliver RNA-loaded lipid nanoparticles[70,101,163–167]. For example, Chen and colleagues developed siRNA-LNP system for subcutaneous (SC) injection delivered siRNA-LNP systems for hepatocyte gene silencing based on particle size, PEG-lipid retention, and hepatocyte-specific ligands[163]. Additionally, mRNA-LNP have been specifically optimized for the intramuscular application. In this case, LNP were developed for mRNA vaccination against infectious diseases and cancer, and therefore LNP aim to target residents DCs and skeletal muscle cells to initiate an immune response[104]. Furthermore, LNP-encapsulated mRNAs have been delivered to the lungs via inhalation to protect against viral infections. The inhalation route is probably the safer and most efficient way to administer therapeutics to the lungs since it maximizes the concentration of the therapeutic in these organs and limits its systemic exposure[166].

Another approach to ensure extrahepatic delivery and reduce off-target effects is to employ **active targeting** by conjugating targeting ligands, such as peptides, antibodies, antibody fragments, or small molecules (reviewed in detail[168]). For instance, systemically administered anti-VCAM-coupled LNP formulated with mRNA encoding for thrombomodulin selectively accumulated in the inflamed brain[169]. Although active targeting has shown enormous potential, its clinical translation is challenging due to the complexity of the manufacturing process and deposition of a protein corona[170]. As an alternative, cell-specific expression can also be obtained by incorporating specific microRNAs (miRNAs) target sites in the mRNA sequence to degrade the mRNA in unwanted cell types. miRNAs are small noncoding RNAs naturally present in the cells that regulate gene expression by repressing the translation of target cellular transcripts[171].

Currently, three LNP formulations approved for RNA therapeutics and several others are being evaluated in pre-clinical and clinical settings[41]. Despite the disparity in the doses, administration route, and disease, Onpattro® patisiran, BNT162b2 (BioNTech/Pfizer), and mRNA-1273 (Moderna) lipid compositions are somewhat similar (Table 1.3-1).

Table 1.3-1 Information about the LNP drug products.

Category	siRNA	Pfizer-BioNTech mRNA vaccine	Moderna mRNA vaccine
Name product	Onpattro * patisiran	BNT162b2; Comirnaty	mRNA-1273;SpikeVax
mRNA dose; route of administration	0.3 mg/kg, intravenous	30 µg; intramuscular	100 µg; intramuscular
Lipid nanoparticle components	DLin-MC3-DMA	ALC-0315	SM-102
	PEG2000-c-DMG	ALC-0159	PEG2000-DMG
		DSPC	
		Cholesterol	
Molar lipid ratios (%) Ionizable lipid: phospholipid: cholesterol: PEG-lipid	50:10:38.5:1.5	47.5:10:40.7:1.8	50:10:38.5:1.5
N/P ratio	3	6	6
Excipients	Potassium phosphate, monobasic, anhydrous	Potassium dihydrogen phosphate	Tris (tromethamine)
	Sodium phosphate, dibasic, heptahydrate	Disodium hydrogen phosphate dihydrate	
	pH ~ 7	pH 7-8	pH 7–8
	Sodium chloride	Potassium chloride	Sodium acetate
	Water for injection	Sodium chloride	Sucrose
		Sucrose	Water for injection
		Water for injection	

*N/P (Nitrogen/Phosphate) ratio

The success of the LNP in the fight against the pandemic also highlighted the sub-optimal conditions of LNP (such as storage, stability, and efficacy) and the related-safety concerns[138,172]. Mild infusion-related reactions (IRRs) have been observed upon IV administration of Onpattro® treatment[101,173] Similarly, several incidences of acute anaphylaxis have been observed since the emergency approval of the Pfizer/BioNTech vaccine, 1 case in 100,000 vaccinations, which is about 10-fold the rate seen with other vaccines

1.4 Aim of the thesis

The advances in nucleic acid therapy have been governed by the progress in the delivery system field. Remarkably, the design of ionizable lipids and the improvements in the manufacturing process enabled the success of lipid nanoparticles for RNA delivery in pre-clinical and clinical studies over the last decade. However, significant opportunities for improvement still remain since the majority of knowledge in engineering and designing lipid carriers for RNA derived from initial studies with LNP formulated for specifically hepatic delivery of siRNA. The influence of critical technical aspects such as manufacturing technology, lipid selection and composition, and particle surface properties on the mRNA functionality is still poorly understood. Moreover, extra-hepatic delivery still persist limited, and new approaches are required to deliver mRNA to other organs of interest. Furthermore, the development of lipid nanocarriers with improved efficacy and safety for mRNA delivery remain the biggest challenges in developing novel RNA-based therapies. Specifically, the design of PEG-free lipid nanoparticles in order to overcome the potency and safety issues associated with the use of PEG-lipids in the LNP, such as reduced transfection efficiency, and as well as the triggering of ABC phenomenon and hypersensitivity reactions (e.g., CARPA). Also, the delivery of alternative RNA formats, such as self-amplifying RNA, which could lead to improved potency and safety in vaccination against infectious diseases have not been fully explored. Finally, alternative methods for production of LNP or other potent nanoparticles are required to tackle the limitations associated with the current rapid-mixing method, which results in LNP with low concentrations and requires buffer exchange.

This thesis aims to gain a deep insight into the fundamentals of mRNA-lipid complexes and rationally design the next generation of lipid delivery systems for potent and safe mRNA therapeutics and vaccines. Throughout this study, the effect of structural parameters, such as N/P ratio, lipid and molar composition, as well as the effect of the manufacturing process on particle size, morphology, transfection efficiency, and biodistribution of mRNA-lipid complexes were systematically investigated.
In addition, a new generation of grafted lipids, polysarcosine-conjugated lipids, were explored as PEG-lipid alternatives to tackle the PEG-associated issues and formulate lipid nanoparticles by rapid mixing for mRNA delivery. The therapeutic potential of polysarcosine functionalized-lipid nanoparticles was further pursued by assembling a panel of proprietary ionizable lipids to improve the overall efficacy. The efficacy, biodistribution, and toxicity of optimized polysarcosine-functionalized LNP were investigated for therapeutic protein replacement purposes.

The final part of the thesis focusses on the use of LNP for vaccination against infectious diseases – an approach that has gained worldwide momentum due to the recent pandemic. Here, we aimed to optimize LNP for intramuscular administration of saRNA encoding for antigens against infectious diseases. Since saRNA and mRNA constructs differ in size, structure, and function, a wide range of parameters were used to optimize and tailor nanocarriers for saRNA vaccination. For this work, an influenza mouse model was used to evaluate the therapeutic potential of newly developed saRNA-LNP.

CHAPTER 2 | Materials and Methods

2.1 Materials

Chol, DSPC, Sodium dodecyl sulfate (SDS), Kolliphor (P188, P181, P338, and P 407), and 1,2-Dioleoyl-sn-glycero-3-phosphoethanolamine labeled with Atto 647N (Atto 647N DOPE) were purchased from Sigma-Aldrich (St Louis, MO, USA). DOPC, DODMA, DOTMA was purchased by Merck (Darmstadt, Germany). N-palmitoyl-sphingosine-1-{succinyl[methoxy(polyethylene glycol)2000]} (PEG-CerC16) was purchased by Avanti Polar Lipids (Darmstadt, Germany). PEG-DMG was purchased from NOF (Frankfurt, Germany). DLin-MC3-DMA, DLin-KC2-DMA, DPL14 were purchased by Nucleosyn (Olivet, France). pSar-lipids were either provided by AG Barz (Johannes Guttenberg University, Mainz, Germany) or purchased by Polymer Therapeutic Solutions (Valencia, Spain). Ionizable lipids described in section 3.1.3 and 3.2.1 were provided by Peer Lab (Tel Aviv University, Tel Aviv, Israel).

2.2 *In vitro* Transcribed mRNA

In vitro transcribed RNA was produced by BioNTech Pharmaceuticals, Mainz, Germany, as described elsewhere[174,175]. IVT firefly luciferase and EPO pseudouridine-modified encoding mRNA was produced by Andreas Kuhn and coworkers (BioNTech RNA Pharmaceuticals, Mainz, Germany). Firefly encoding mRNA containing miR-122, miR-650, or mirR-143-3p target sites was synthesized by and (BioNTech RNA Pharmaceuticals, Mainz, Germany). Hemagglutinin (HA), ZEBOV GP, and luciferase–encoding saRNA was synthesized by and coworkers, according to the literature[176].

2.3 Nanoparticle Formulation

2.3.1. Aqueous-Aqueous mixing

Liposomes were produced using an adopted proprietary protocol based on the ethanol injection technique[177]**.** In this thesis, liposomes were composed of ionizable cationic lipids instead of the conventional cationic lipids. Briefly, the lipid mixtures containing ionizable lipid, cholesterol, phospholipid, and PEG-lipid were prepared in absolute ethanol (ETOH) (Merck KGaA, Darmstadt, Germany) and stored at -20 °C until further use. For liposome preparation, 400 µl of an ethanolic lipid solution with a concentration of 75 mM or 208 mM was injected into 9.6 ml of 2 mM acetic acid in nuclease-free water (Carl Roth Gmbh & Co. Kg, Karlsruhe, Germany) using a 0.9x40 mm needle (Microlance 3, BD Biosciences, Heidelberg, Germany), under stirring at 220 rpm on a magnetic stirrer. After stirring for 30 min, the liposome solution was stored at 4 °C until further use.

mRNA-LPX were manufactured under sterile and nuclease-free conditions to avoid contamination and degradation of mRNA by ubiquitous RNases. An appropriate volume of liposome solution was added under vigorous vortexing to an mRNA solution in nuclease-free water to reach a desired N/P ratio in the presence or absence of sodium chloride (NaCl) (Ambion, Austin, TX, USA), in a sequential manner. Liposomes with a concentration of 75 mM were mixed with mRNA to prepare 200 nm-LPX, while 100 nm-LPX were manufactured by mixing a lipid mixture of 208 nM with mRNA solution.

After 10 minutes (min) incubation, NaCl concentration was adjusted to a final concentration of 150 mM, and mRNA-LPX were stored at 4 °C until further use.

2.3.2.Ethanol-Aqueous mixing

LNP were prepared by mixing an ethanolic solution of lipids with an acidic solution containing mRNA using a microfluidic instrument (NanoAssemblr, Precision NanoSystems, Vancouver, BC). Before mixing, mRNA was diluted in 100 mM citrate buffer (CB) pH 5.4 to a concentration of 0.15 mg/ml, and the lipids were diluted in absolute ETOH to an appropriate lipid concentration in order to reach a desired N/P ratio. A stepwise dilution was included to reduce the ETOH concentration immediately upon formulation (1 ml of 1 x Dulbecco's phosphate-buffered saline (DPBS) was added previously to the 14-ml falcon to manufacture 2 ml LNP solution).

For studies involving N/P ratio, the concentration of the starting lipid mixture varied from 1 mM to 20 mM. If not stated otherwise, LNP were manufactured by mixing 13.5 mM of lipid mixture with a 0.15 mg/ml mRNA solution to reach a N/P of 4. The poloxamer-functionalized LNP were prepared by mixing a lipid mixture of DODMA, Chol, DOPE, and Poloxamer P338 (45:44:10:1 and 45:43:10:2 mol %) at 9 mM with mRNA in 10 mM CB at pH 4 solution at 0.15 mg/ml, at N/P 3, using the Nanoassemblr® device.

The microfluidic settings were the following: total flow rate =12 ml/min, flow rate ratio (ethanolic phase: aqueous phase) = 1:3, start waste =350 µl, end waste =50 µl, unless stated otherwise.

Lipid nanoparticles of increased particle sizes (~200 nm sizes) were prepared by mixing a lipid mixture of 4.5 mM with an mRNA solution at 0.15 mg/ml, at the following settings: flow rate 6 ml/min), flow ratio (1:1), start waste (350 µl), end waste (50 µl).

In all above conditions, the LNP solution (1-3 ml) was dialyzed against 500 ml of DPBS (Gibco, Life Technologies, Carlsbad, CA, USA) for 3 h in a 10 K MWCO dialysis cassette (Slide-A-Lyser, Thermo Fisher Scientific, Waltham, MA, USA). LNP solution was concentrated using ®Amicon 30 K Ultra Centrifugal Filters (Merck, Darmstadt, Germany), if necessary. LNP solution was stored at 4 °C for a maximum time of 5 days.

The preparation protein-functionalized LNP involved the mixing of ethanol phase containing the lipids of DODMA, DOPE at a 50:50 mol % and at a total lipid concentration of 9 mM with an aqueous phase containing the mRNA at 0.15 mg/ml and HSA at 20 mg/ml in 100 mM citrate buffer (CB) pH 5.4. For this experiment, NanoAssemblr Spark® (Precision NanoSystems, Vancouver, BC) were used since it enables to produce very low amounts of LNP volume (25 – 250 µL).

2.4 Physicochemical techniques

2.4.1.Nanoparticle characterization

Particle size analysis was done by dynamic light scattering using a DynaPro Plate Reader II (Wyatt, Dernbach, Germany). mRNA-formulations were diluted in DPBS to a final RNA concentration of 5 µg/ml and added to a Nunc transparent 96-well plate (Thermo Scientific, Waltham, MA, USA) at 120 µl/well. Data was acquired 10 times, with 5 seconds per acquisition, at 23 °C with a viscosity of 0.931 cP, using Dynamics software (Version 78026). Z-average and polydispersity index (PdI) was calculated using the cumulate formalism[178].

Zeta (ξ)-potential was investigated via laser doppler electrophoresis using WALLIS$^{\zeta TM}$ (Coorduan technologies, Pessac, France). LNP and LPX were diluted to a final mRNA concentration of 10 µg/ml in 0.1x DPBS (diluted in nucleases-free water) or in 13 mM NaCl solution, respectively. In some experiments, the LPX and LNP were diluted in diethyl pyrocarbonate (DEPC)-treated water. All samples were measured at 23 °C, with a viscosity of 0.931 cP, a dielectric permittivity constant of 78.77, at medium resolution measurement (3 sequences of 10 runs each). Measurements with low signal to noise ratios, or with extreme mobility µ (>3 or <-3 µm*cm/V*S) were excluded from the final analysis. ξ-potential was calculated using the Smoluchowski approximation, where $v = (\varepsilon E/\eta)\ \xi$, where v is the measured electrophoretic velocity, η is the viscosity, ε is the electrical permittivity of the electrolytic solution, and E is the electric field.

Encapsulation efficiency, or accessible mRNA, was evaluated by a modified Quant-iT Ribogreen Assay (Invitrogen, Carlsbad, CA). Briefly, in Nunc black 96-well plate (Thermo Fisher Scientific, Waltham, MA, USA.), formulation samples and sample buffer were diluted in duplicates in 1x TE buffer (10 mM TRIS, 0.1 mM EDTA, pH 8) to a final mRNA concentration between 2-5 ng/µl. Subsequently, 50 µl of the diluted sample was added to 50 µl of 1x TE (accessible mRNA) and 50 µl of 2% Triton X-100 (VWR International GmbH, Germany) (total mRNA). 100 µl of RiboGreen dye (diluted 1/100 in TE) was added to each sample and incubated for 5 min in the dark. The fluorescent intensity was quantified in an Infinite F200PRO microplate reader (Tecan, Männedorf, Switzerland). Bound and unbound mRNA was qualitatively assessed by agarose gel electrophoresis. 1 % agarose gel (Agarose Standard, PanReac AppliChem, Darmstadt, Germany) containing 0.05% of sodium hypochlorite (Sigma-Aldrich Chemie GmbH, Germany), 1x Tris-acetate-EDTA (TAE) Buffer (Rotiphorese® 50X TAE, Carl Roth, Karlsruhe, Germany) and 10 µl of GelRed Nucleic Acid Gel Stain (Biotium, Hayward, CA, USA) were used to prepare the agarose gel. The formulation samples were incubated either with 10% Triton X-100 (bound and unbound mRNA) or diluted in DPBS (unbound mRNA) in a 1:1 (v/v) ratio for 8-10 min at 40 °C. After the addition of DNA Gel Loading Dye (6X, Thermofisher, Waltham, MA, USA), the gel electrophoresis was run at 80 V, 500 mA, 50 W for 40 min. Images were acquired with ChemiDOC XRS+ Imaging device (BioRad, Berkeley, CA, USA).

2.4.2.TNS assay

2-(p-toluidino)-6-naphthalene sulfonic (TNS) acid (Merck KGaA, Darmstadt, Germany) is a negatively charged probe that only fluoresces when associated with the surface of positively charged membranes in aqueous solutions. TNS assay has been used extensively to probe positive charge at membrane surfaces, and its implications in particle design[179–181]

A series of buffers with pH ranging between 3 and 9 were prepared by adjusting the pH of a solution containing 10 mM citrate, 10 mM phosphate, and 10 mM borate complemented with 150 mM of NaCl. In Nunc black 96-well plate, 90 µl of each buffer solution was added to 2 µl of a 300 µM solution of TNS prepared in DMSO (Carl Roth GmbH & Co. Kg, Karlsruhe, Germany). 10 µl of lipid formulation (prepared without mRNA) was added to the above mixture to a final concentration of 22 µM. The fluorescence intensity was measured at an excitation wavelength of 322 nm and an emission wavelength of 431 nm in Safire 2 microplate reader (Tecan, Männedorf, Switzerland). A sigmoidal best

fit analysis was applied using Origin software and the pKa was measured as the pH at half-maximal fluorescence intensity.

2.4.3.Cryo-TEM

Cryogenic transmission electron microscopy (Cryo-TEM) is a microscopy technique in which a beam of electrons is transmitted through a specimen in a holder capable of maintaining the specimen at liquid nitrogen or liquid helium temperatures to form an image. This technique allows imaging of specimens prepared in vitreous ice that enables the imaging of individual molecules or macromolecular assemblies. To evaluate the particle size and morphology, mRNA-lipid formulations were imaged by Cryo-TEM.

Grids were hydrophilized by oxygen plasma (negative surface charge), and each sample was vortexed for 30 s before grid preparation. The samples were preserved in vitrified ice supported by QuantiFoil® R2/1 holey carbon films from Quantifoil Micro Tools GmbH (Jena, Germany). After applying 6 µl sample suspension, vitrification in liquid ethane at -180°C with a Leica EM GP from Leica Microsystems GmbH (Wetzlar, Germany) was performed. The final grids were stored under liquid Nitrogen and Cryogenic TEM imaging was performed with a Zeiss Libra® 120 from Carl Zeiss (Jena, Germany) at 120 kV acceleration voltage under liquid N_2 cryo-conditions, and the images were taken with a Gatan UltraScan® CDD camera (Gatan, Inc, Pleasanton, Ca, USA). Vitreous ice grids were transferred into the electron microscope using a cryostage that maintains the grids at a temperature below -170°C. Images were acquired at multiple scales to assess the overall distribution of the specimen.

2.4.4.Small Angle Scattering X-rays and Neutrons

Small Angle X-rays (SAXS) is a scattering technique used in biophysics to analyze the size, shape, and structure of macromolecules. In SAXS setup, a collimated, monochromatic x-ray beam incident on a sample scatter onto a 2D detector, giving rise to a diffuse pattern (see Figure 2.4-1).

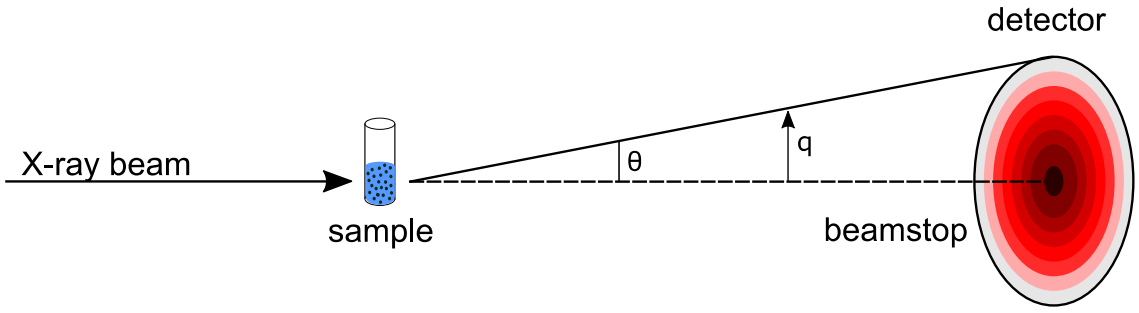

Figure 2.4-1 Schematic geometry of conventional x-ray scattering experimental set up.

If we consider a particle consisted of n elements (e.g., atoms or larger model-elements) as depicted in Figure 2.4-2

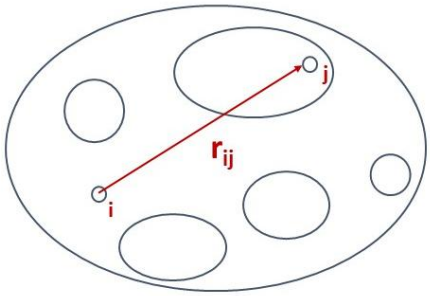

, then a particle can be described as:

Equation 1

$$r_{ij} = \left|\overrightarrow{r_{ij}}\right|$$

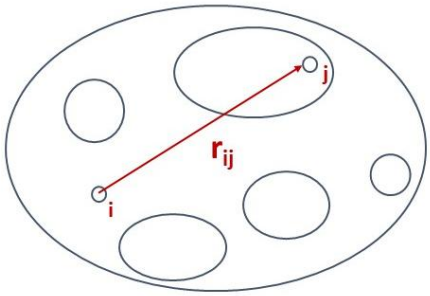

Figure 2.4-2 A schematic graphic of a particle.

If particles are measured in the solution, then the difference between the scattering length density of the element (ρ_i) and the solvent (ρ_{solv}) can be described by the contrast ($\Delta\rho$). Since the excess scattering length of the n model elements can be varied by changing the scattering length density of the solvent, The scattering function can be obtained by modification of Debey´s scattering formula:

Equation 2

$$I(k, \rho_{solv}) = d_v^3 \sum_{i=1}^{n} \sum_{j=1}^{n} \{ (\rho_i - \rho_{solv}) \times (\rho_j - \rho_{solv}) \frac{sin(qr_{ij})}{qr_{ij}} \}$$

Since these particles are placed unorderly in a sample volume V which was irradiated by incident x-rays, all orientations of the particles have the same probably and that no order preferred exist. Within this sample volume a N number of particles is excited to scatter. In this system, no long range of order exist and thus, the distribution of particles is isotropic.

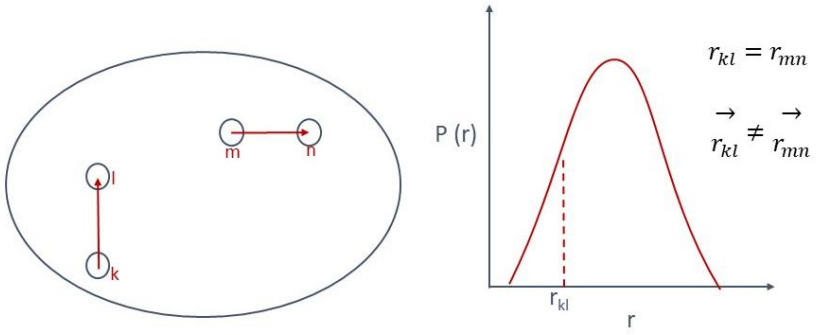

Figure 2.4-3 A graphical drawing of the statistics of the distance in the particle.

The scattering from a single particle can be derived from the form factor P(q) which strongly depends on its size and shape. Homogeneous particles with electron density ρ_P and volume V_P, dispersed in a homogeneous matrix with electron density of ρ_0. The scattering intensity I(q) from a single particle at a scattering angle 2θ as a function of the scattering vector q, $q = 4\pi\sin\theta/\lambda$ can be expressed by:

Equation 3

$$I(q) \propto \frac{d\sum(q)}{d\Omega} = \frac{1}{V}\left|\int p(r)e^{iqr}\mathrm{dr}\right|^2$$

where ρ(r) is the electron density, and V is the illuminated volume. The scattered intensity I(q) is proportional to the square of the Fourier transformation of electron density. For identical particles, ρ(r) is a constant and the total scattering intensity can be further expressed by:

Equation 4

$$I(q) = \frac{d\sum(q)}{d\Omega} = \frac{N}{V}\,(\rho_p - \rho_0)^2 V_p^2 \left|\frac{1}{V_p}\int p(r)e^{iqr}\mathrm{dr}\right|^2$$

As in this system no longer order exist, the distribution of particles is isotropic. The total charge distribution can be written as $\rho(r) = \rho_P - \rho_0$ is the difference of electron density between particle and matrix, it is normally called “scattering contrast”. Then, the scattering intensity, I(q), as a function of the momentum transfer, q, is directly correlated to the autocorrelation function of the electron density distribution.

Equation 5

$$\boldsymbol{I(q) \sim \left|\int p(r)e^{iqr}d^3\right|^2}$$

The characteristic length information scales with 1/q, i.e., scattering at low q gives information on large sizes (up to ~1 μM), while the scattering at high q comprises information on smaller sizes (up to 1 nm). At q-range from about 0.03 nm^{-1} to about 5 nm^{-1}, scattering from structures at length scales between several nanometers down to the Angstrom range (~200 nm to ~12 Ä) becomes relevant, where information on ordered and non-ordered structures can be derived. In case repeating stacks of defined

structures (such as bilayers) are present, scattered intensity can be approximated as a function of the form factor, F(q), and the structure factor G(q):

Equation 6

$$I(q) \sim F(q) * G(q)$$

The structure factor represents repeating patterns with defined organization as outlined below. The form factor derives from the electron density distribution of single or non-ordered scattering units, which can be the whole particle, or as well the singe bilayer in a stack. For example, for spherical compact particles, a scattering curve with oscillations according to:

Equation 7

$$I(q) \sim \left[\frac{3[sin(q * R) - q * R * cos(q * R)]}{(q * R)^3}\right]^2$$

would be expected (with q= momentum transfer, R = radius of the particle). This curve has a first minimum at q=4.66/R. This formalism can be used to get an estimate on the particle size, neglecting parameters like polydispersity, anisotropy, surface roughness of packing compactness.
Some further information on the particle characteristics can be obtained by analyzing the intensity decay using the power law, defined by:

Equation 8

$$I(q) \sim I(0) * q^{-x}$$

Which provides insight into the packing compactness and fractal dimensionality of the particles is obtained. For particles with smooth surfaces, the intensity decays with the 4th power of q (Porod law), where the decay becomes less steep if the roughness increases. For example, a rough interface is expected to yield a value of 3 for the exponent, while for Gaussian chains a value of 2 is expected. Flat particles or increased polydispersity can yield a value of 2[182].
Scattering from ordered structures results in peaks, from which further information on the internal organization can be derived. Using Bragg's law, the repeat distance is obtained from the peak position according to:

Equation 9

$$d = \frac{n * 2\pi}{q_n}$$

where q_n is the maximum position of the nth order peak. Typical types of organization are lamellar stacks, resulting in equidistant Brag peaks (positions 1, 2, 3,…), hexagonal structures (positions,1, √3, 2, √7, 3,) or cubic phases (1, √2, √3, 2, √5,…)[183]. The width, w, of the peaks is analyzed to get information on the number of ordered units or on the positional order of the stacks. Lipidic systems in an aqueous environment are usually described as liquid crystalline phases, where the positional order decays as a function of the distance. In a generally accepted model to describe liquid crystalline arrays[184], the correlation length, w, defined as the distance at which the positional correlation decays to the value 1/e is given as:

Equation 10

$$x \sim \frac{2}{w}$$

The area of the peaks was taken as a measure for the total amount of material present in the respective state of the organization. The scattering curves can be compared with diffraction patterns from organized units using basic formalisms in an utmost reductionistic manner. One-dimensional ordered arrays consisting of scatterers of homogeneous internal electron density distribution and fixed length, l, forming stacks with spacing, d, where scattering for increasing numbers, N, (N=2, 3, 4,…) in the stacks was calculated. Following equation 2, for the form factor a slit function was used:

Equation 11

$$F(q) \sim \left| \frac{sin\left(q * \frac{l}{2}\right)}{q * \frac{l}{2}} \right|^2$$

and for the Structure Factor, a lattice with N repeat units is considered.

Equation 12

$$G(q) \sim \left| \frac{sin\left(N * q * \frac{d}{2}\right)}{q * \frac{d}{2}} \right|^2$$

Simulations and data analysis were performed with OriginLab Corporation (Northampton, MA, USA) software package. The implemented non-linear fitting protocol was used for fitting of Lorentzian peak profiles using the formalism:

Equation 13

$$y = y_0 + \left(\frac{2 * A}{\pi}\right) * \left(\frac{w}{4 * (q - q_c)^2 + w^2}\right)$$

where y_0 is the offset, x_c is the peak center, w is the FWHM, and A is the peak area. Prior to fitting, a linear baseline was subtracted from the experimental data manually. In certain cases, double Lorentzian fitting was tried to model the data. Due to the large width of the main peaks, there was an indication, that these should be better represented by the superposition of two separate peaks such as resulting from organized stacks of pure lipids and lipid complexed RNA with different spacings. With that, lower values of x^2 were obtained however, no substantial additional information was gained, and therefore, for most cases only single Lorentzian were used. Only in case or the systems with high fractions of pSar$_{11}$, where the presence of two peaks was obvious, both peaks were fitted. The position of the maximum peak height, q_c, and the peak width, w, were used to calculate the Bragg spacing (d-spacing), and the correlation length (ξ) of the internal lamellae of the lipid vehicles.

The SAXS measurements were performed at the EMBL P12 bioSAXS beamline at PETRA III, DESY (German Electron Synchrotron Hamburg, Germany). The measurements were conducted at an X-ray energy of 10 keV and a flux of 5 ×10^{12} ph/s; the beam size at the sample position was 0.2 × 0.3 mm² (v × h, full width half maximum, FWHM) and with the help of BioSAXS Sample Changer [185]. Low

volumes (30 µl) of the samples were transferred to quartz capillary mounted in vacuum, and a PILATUS 6M detector was used to collected images. Images of the scattering signal were processed by the SASFLOW pipeline [186]: all images were radially averaged, the frames were compared for radiation damage, and excluded if the frames were subjected.

2.4.5.Liquid chromatography-mass spectrometry (LC-MS)

Liquid chromatography-mass spectrometry (LC-MS) is an analytical chemistry technique that combines the capabilities of liquid chromatography with mass spectrometry. While liquid chromatography allows the separation of mixtures with multiple components, mass spectrometry provides structural identity of the individual components with high molecular specificity and detection sensitivity. This technique has been applied to analyze biochemical, organic, and inorganic compounds commonly found in complex samples of environmental and biological origin. Therefore, LC-MS can be used to monitor the lipid biodistribution after *in vivo* administration of mRNA-lipid complex.

LC-MS analysis was conducted on a 1290 Infinity Ultra High Performance Liquid Chromatography (UHPLC) consisting of a binary pump connected to a 6460 Triple Quadrupole Mass Spectrometer (Agilent Technologies, Santa Clara, USA) equipped with an electrospray ion source with Jet Stream Technology. For the liquid chromatographic separation, a reversed-phase column Zorbax SBC18, RRHD (21 x 50 mm, 18 µm) (Agilent Technologies, Santa Clara, USA) was used. The column and autosampler temperatures were 50 and 20 °C, respectively. The injection volume was 5 µl. Upon every injection, the needle was flushed with methanol/isopropanol (1:1, v/v) for 15 sec flow rate was 0.5 ml/min. The mobile phase comprised two eluents including 0.1% ammonium acetate, 0.1% acetic acid in water/methanol (1:1, v/v) (eluent A) and 0.1% ammonium acetate, 0.1% acetic acid in isopropanol/methanol (1:1, v/v) (eluent B). For the liquid chromatography gradient, 50 % of eluent A was added to 100 % of eluent B in 35 min, where it remained for 45 min, 50% of eluent B was added for 30 sec, and the column was stabilized by 35 min flow of 50 % of eluent A, and 50% of eluent B. For the Agilent Triple Quadrupole instrument, the electrospray ionization source was operated on positive ion mode and the optimal sources were as following: drying gas temperature 275°C, gas flow 13 l/min, capillary voltage 4500 V, nebulizer gas (nitrogen) pressure 30 psi and the highest parent ion abundance was determined using fragmentor voltages of 258 V. Product ion (MS2) spectra were generated using collision-induced dissociation (CID) in the collision cell with nitrogen gas. The most intense product ion signal was achieved by applying offset voltages of 45 eV and 50 eV. Following transitions were selected for multiple reaction monitoring (MRM): m/z 6211→581 (Quantifier) and m/z 6211→841 (Qualifier). Data acquisition and quantitation of the analyte DODMA was performed using the Agilent MassHunter Workstation software. LC-MS measurements were conducted by (BioNTech RNA Pharmaceuticals, Mainz, Germany).

2.5 Cell Culture

2.5.1.Cell culture and cell culture medium

Cell lines were handled under sterile conditions in a laminar airflow hood (Heraeus Instruments, Hanau, Germany) and cultivated at 37 °C and CO_2 in the HERAcell 240i incubator (Thermo Scientific,

Waltham, MA, USA.). The cells were subcultured with Acutase (StemPro Accutase, Thermo Fisher Scientific Scientific, Waltham, MA, USA.)).

Table 2.5-1 Cell and culture mediums.

Cell lines	Medium		Conditions
HepG2	Eagle Minimum Essential Medium (EMEM) 10 % non-inactivated FBS)	Life Tecnologies, San Diego, USA Life Tecnologies, San Diego, USA	5 % CO_2
C2C12	Dulbecco Modified Eagle Medium (DMEM) 10 % non-inactivated FBS	Life Tecnologies, San Diego, USA Life Tecnologies San Diego, USA	7.5 % CO_2
RAW 264.7	Eagle Minimum Essential Medium (EMEM) 10 % non-inactivated FBS	Life Tecnologies, San Diego, USA Life Tecnologies, San Diego, USA	5 % CO_2

2.5.2.Cell density and viability

The cell counting and viability were performed on Scepter™ 2.0 Cell Counter (Merck KGaA, Darmstadt, Germany) using the Coulter impedance-based particle detection principle[187]. The cells flow through the aperture in the sensor causing an increase in the resistance and thereby an increase in the voltage. The voltage changes are recorded as spikes, and spikes with comparable size are agglomerated into a histogram and counted. The histogram provides quantitative data on cell morphology, which can be used to evaluate cell viability and cell density. A single-cell suspension of HepG2, C2C12, and RAW 264.7 were prepared in DPBS buffer to a final concentration between 10000 to 500000 cells/ml. The cell concentration was obtained by using a sensor with an operating range for 60 µM, and by adjusting the histogram displayed as a function of cell diameter to eliminated duplexes and dead cells.

2.5.3.Cell-binding assay

Flow cytometry is a biophysical method that utilizes laser-based technology to profile cells in a heterogeneous fluid mixture. Cells or particles suspended in a liquid stream are passed through a laser light beam in a single file manner, and interaction with the light is measured by an electronic detection apparatus as light scatter and fluorescence intensity. The forward scatter (FSC) and the sideward scatter (SSC) correlates with the size and granularity of the analyzed cell, respectively. In the case of the fluorescence intensity, i.e., when fluorescent label-antibodies, or fluorescent dyes, are linked specifically to a cellular or compartment component, the fluorescence intensity represents the amount of that particular cell component.

For the cell-binding assay, HepG2 and RAW 264.7 cells were seeded at 20 000 and 25 000 cells/ well, respectively, in Nunc transparent flat-bottom 96-well plate (Thermo Scientific, Waltham, MA, USA). mRNA-lipid complexes containing 0.05 % of ATTO Atto647N were incubated at 50 ng of mRNA for 30 min at 4 °C in the dark. After incubation, the cells were centrifugated at 500 g for 5 min and then, incubated with 20 µl of Accutase for 7 min. The cells were then resuspended in 100 µl 1xPBS (4°C) and transfer to a round bottom 96 well plate and washed twice at 500 x g for 5 min. The cells were then incubated with the viability dye eFluor450 (1:7500, in 100 µl PBS) for 30 min at 4°C, in the dark. After

washing procedure, the cells were resuspended in 200 µl FACS buffer and acquired with FACS Celesta, HTS analytical flow cytometer (BD Biosciences, Heidelberg, Germany), and analyzed with FlowJo software (Tree Star, Ashland, OR, USA.).

2.5.4.Luciferase and Viability assay

Luciferase activity assays are a reliable and sensitive method to detect the expression of luciferase in live cells[188]. In this assay, firefly luciferase catalyzes the mono-oxygenation of beetle luciferin via adenosine triphosphate (ATP) and Mg^{2+}-dependent reaction, resulting in the emission of light in the range of 550 to 620 nm (bioluminescence)[189].

For cell transfections, HepG2, C2C12, and RAW 264.7 cells were seeded at respective cell number of 20 000 cells/well, 5 000 cells/well, and 40 000 cells/well in Nunc white flat-bottom 96-well plate (Thermo Scientific, Waltham, MA, USA) and centrifuged at 500 x g for 5 min. After 18-24h, the medium was replaced by fresh medium at 90 µl/well. Formulation samples were assessed at mRNA concentration between 50 to 12.5 ng per well, and medium was used as negative and blank control. Samples and controls were added at 10 µl/well. After 24 h, luciferase expression was determined by Bright-Glo™ Luciferase assay (Promega, Madison, WI, USA) according to the manufacturer's protocol. Briefly, the reagent was added to the cells in the medium at 1:1 (v/v) ratio, followed by an incubation of 5 min in the dark to allow for complete cell lysis. Viability was measured by CellTiter-Glo® (Promega, Madison, WI, USA) according to the manufacturer's protocol. Briefly, the reagent was added to the cells in the medium at 1:1 (v/v) ratio, followed by an incubation of 10 min in a shaker followed by 20 min to allow for stabilization of the signal.

Alternatively, luciferase and viability were determined by ONE-Glo™ + Tox Luciferase Reporter and Cell Viability Assay (Promega GmbH, Madison, WI, USA) according to manual instructions. Briefly, 20 µl of 5X CellTiter-Fluor™ Reagent was added to the wells and mix by orbital shaking (300–500rpm for ~30 sec). After incubation for 30 min at 37°C, the fluorescence was measured with excitation wavelength at 400 nm and emission at 505 nm (viability). Then, ONE-Glo™ Reagent was added at 100 µl/well. After incubation for three min, the bioluminescence was measured (luciferase expression). Bioluminescence signals (photons per second [p/s])), and fluorescence was measured using a microplate luminescence reader Infinite M200 (Tecan, Männedorf, Switzerland). The relative luminescence was calculated by subtracting the signal of the cell treated with DPBS control from the sample control.

The relative viability was calculated by:

Equation 14

$$\boldsymbol{Viability}\,(\%) = \frac{(\boldsymbol{RLU\ sample - RLU\ blanck})}{(\boldsymbol{RLU\ PBS - RLU\ blanck})} \times \mathbf{100}$$

2.5.5.Hemolysis Assay

Hemolysis is characterized by the lysis of red blood cells (RBC), leading to the release of hemoglobin into the blood plasma. This hemoglobin release can lead to anemia, jaundice, and other pathological conditions, which could become life-threatening. Whenever nanoparticles are administered

IV, they may cause hemolysis due to small curvature and the sizeable surface-area-to-volume ratio of nanoparticles, which make hemolysis thermodynamically favorable. In addition, erythrocyte hemolysis can be used as a surrogate assay for endosomal escape due to similarities in their lipid bilayer (phospholipid and Chol) and glycocalyx compositions[190].

Hemolysis was performed both at a physiological pH of 7.4 and endosomal pH of 5.5; erythrocytes lysis at pH 7.4 is an indication of toxicity, whereas at pH 5.5 is a model for the endosomal membrane escape, i.e., the ability of the LNP to interact with endosomes/lysosomes membranes upon acidification. Blood from four donors was withdrawn into K2-EDTA-coated vacutainer tubes (Sarstedt AG & Co, Nümbrecht, Germany) and centrifuged for 5 min at 500 x g. After marking the levels of hematocrit and plasma, the plasma was aspirated until hematocrit level and filled up with DPBS. The RBC were washed three times with DPBS at 500 x g for 5 min. Undiluted RBC was then mixed and diluted either in DPBS or in CB saline (20 mM CB, 130 mM NaCl) at pH 5.4 to 4 % (v/v) of RBC solution. 0.1% Triton-X100 and DPBS were used as positive and negative controls, respectively. Formulations were diluted in DPBS to mRNA concentration of 0.05 µg/µl. In Corning® V-shaped 96-well plate (Thermo Scientific, Waltham, MA, USA.), 100 µl of samples or controls were added to 100 µl of the 4 % RBC solution in either DPBS or CB solution. The incubation was performed at 37 °C for 1 h under shaking. After cooling, the plate was centrifuged at 500 x g for 5 min 100 µl of the supernatant was transferred into a transparent 96-well assay plate. The ultraviolet absorption was read at 540 nm in Microplate Reader Infinite M200 PRO (Tecan, Männedorf, Switzerland).

2.5.6.Whole Blood Assay

Human whole blood is considered a reliable and predictive model to investigate the potential of drugs to induce a cytokine storm[191]. This is characterized by high plasma levels of inflammatory cytokines, chemokines, and interferons and accompanied by fever, hypo- or hypertension and may progress to a more severe life-threatening condition called systemic inflammatory response syndrome (SIRS).

Human whole blood from three healthy donors was collected in Li-heparin vacutainer tube (BD Vacutainer® Li-heparin, Becton Dickinson GmbH, Heidelberg, Germany). Whole blood was diluted 4X with RPMI culture medium (RPMI 1640 – GlutaMAX™ –I, Thermo Fisher Scientific, Bleiswijk Netherlands) containing 10 % of heat-inactivated fetal bovine serum (FBS) and platted in a flat-bottom 96-well plate at 180 µl/well. Positive controls such as Requisimod (R848) (Merck KGaA, Darmstadt, Germany) and Lipossacharide (LPS) (Invivogen, San Diego, CA, USA) were added at assay concentrations of 10 mM and 20 ng/ml, respectively DPBS was used as vehicle buffer and negative control. Lipid formulations were diluted in DPBS to an mRNA concentration of 312.5, 62.5, and 12.5 µg/ml corresponding to 5 x the final assay concentration. These final mRNA concentrations correspond to 5 and 1x the theoretical human plasma concentration of a human mRNA dose of 10 mg/Kg. 20 µl of controls or samples were added to the diluted whole blood and incubated at 37 °C, 5 % CO_2 for 24 h. Plasma was then collected and stored at -80 °C until analysis. Cytokine levels were measured using a Bio-Pex 200 Luminex (Bio-rad Laboratories, Hercules, CA, USA) with Cytokine Human Ultrasensitive Magnetic 10-Plex Panel (Waltham, Massachusetts, USA.). Analytes included: GM-CSF, IFN-γ, IL-1β, IL-2, IL-4, IL-5, IL-6, IL-8, IL-10, and TNF-α.

2.5.7.Complement Activation by EIA

The complement is a key part of the innate immune system acting as the first line of defense against pathogens. It is composed of a group of proteins linked to each other in a biochemical cascade that enables three main functions: 1) opsonization which subsequently leads to clearance by phagocytic cells; 2) release of potent soluble mediators that recruit and activate immune cells; 3) formation pores in the membranes that can lyse cells. In the case of systemically administered drugs, complement is responsible for hypersensitivity (allergic) reactions and anaphylaxis, a life-threatening condition. Hence, nanoparticles intended for systemic administration are required to be evaluated for potential activation of the complement system.

The complement activation of lipid nanoparticles was investigated by determining the concentration of C3a fragment that is common to lectin, classical, and alternative pathways. The concentration of LNP was selected based on the theoretical plasma concentration of the nanoparticle for the intended therapeutic dose (reviewed elsewhere[192]). In this example, we assume a mouse dose of 12.3 mg/kg, thus the scaled equivalent dose would be:

Equation 15

$$Human\ dose = \frac{mouse\ dose}{12.3} = \frac{12.3\frac{mg}{Kg}}{12.3} = 1\frac{mg}{Kg}$$

Since the blood volume constitutes 8% of the body, thus an average human of 70 Kg body weight has approximately 5.6 L of blood.

$$theoretical\ plasma\ concentration = \frac{human\ dose}{human\ blood\ volume} = \frac{70\ Kg\ x\ 1\frac{mg}{Kg}}{5.6\ L} = 0.0125\frac{mg}{ml}$$

Lipid formulation was diluted in DPBS to a final mRNA concentration of 312.5, 62.5, and 12.5 µg/ml, which correspond to a final assay concentration of to 5, 1, and 0.2 x the theoretical human plasma concentration equivalent of a human mRNA dose of 1 mg/Kg. Vehicle buffer DPBS and 200 mM solution of EDTA (Merck KGaA, Darmstadt, Germany) were used as negative control. Cremophor El solution and 20 u/mL of Cobra Venom Factor (CVF), Quidel, San Diego, USA) were used as positive controls. Cremophor El was prepared by dissolving 100 mg anhydrous citric acid (Merck KGaA, Darmstadt, Germany) in 50 ml absolute ethanol, which was combined with Cremophor El (Merck KGaA, Darmstadt, Germany) in 1:1 (v/v) ratio. The final mixture was filtrated through 0.22 µM filters (Merck KGaA, Darmstadt, Germany). Samples and controls were incubated with Normal Human Serum Complement (NHS, Quidel, San Diego, USA) in a 20:80 (v/v) ratio for 1 h at 37 °C. To stop the reaction, the appropriate volume of a 200 mM of EDTA solution (1/10, v/v) was added to the specimens on ice following by the addition of the Specimen Stabilizer (Quidel, San Diego, USA) in 1:1 ratio (v/v). Specimens were then stored at -20 or 4 °C for further evaluation with the C3a Plus EIA kit (Quidel, San Diego, USA). Specimens were diluted in Specimen Diluent following the conditions: buffer control (1:1000), EDTA (1:500), CVF (1:10000), Cremophor (1:4000), formulation samples (1:25000, 1:5000, 1:10000). Then, Specimen Diluent (blank), C3a Plus Standards (A, B, C, D, E), C3a Plus Low Control, C3a High Control, and diluted specimens were added at 100 µl/well in duplicates to microassay wells. After 60 min incubation at room temperature, the plate was washed four times in HydroSpeed™ plate

washer (Tecan, Männedorf, Switzerland) with 300 µl/well of Wash Solution. C3a Plus Conjugate was added at 100 µl/well and the microassay was incubated for 60 min at room temperature. The washing process was repeated, and 100 µl of substrate solution was added to microassay wells followed by incubation for 15 min at room temperature. Stop solution was added at 100 µl/well, and the absorbance was read at 450 nm in microplate reader Infinite M200 PRO (Tecan, Männedorf, Switzerland). The C3a concentration was calculated using a 4-parameter logistic curve and multiplying by the appropriated specimen dilution factor.

2.6 Animal Experimental Techniques

2.6.1. Animals

Healthy female Balb/C mice were obtained from Charles River Animals were kept under federal and state policies on animal research at BioNTech SE.

2.6.2. Anesthesia

Mice were anesthetized with 2.5 % isoflurane and O_2 in a plexiglass chamber and XGI-8 Gas Anesthesia System (Perkin Elmer, Waltham, MA, USA). Blood retrieval and retro-orbital intravenous injection were performed when the footpath reflex was no longer observed. For *in vivo* bioluminescence measurements, mice were kept under constant anesthesia until the measurement was completed.

2.6.3. Bioluminescence imaging

Bioluminescence imaging is an optical technology based on the detection of light emitted by luciferases from tissues[193]. In the case of the firefly (Photinus pyralis), the luciferase enzyme converts its substrate D-luciferin to oxyluciferin via an ATP-dependent pathway. This process emits low levels of photons (2 to 3 eV) that can be detected and counted by a cooled CCD camera. Hence, this technique can be used to evaluate the biodistribution and capabilities of nanoparticles to deliver RNA to target cells and organs. To evaluate the biodistribution, nanoparticles formulated with luciferase-encoding mRNA were injected IV (via retro-orbital) or IM (in tibialis posterior) with 10 to 2 µg of mRNA. After 6 and 24 h post-administration, an aqueous solution of 0.006 mg/µl of D-luciferin (BD Biosciences, Heidelberg, Germany) was injected intraperitoneal (IP), and within 10-25 min, the bioluminescence was performed on living mice or isolated organs in Xenogen IVIS Spectrum (Caliper Life Sciences, Hopkinton, MA, USA). Images were quantified by region of interest (ROI) as total flux (p/s) using Living Image Software 40 (Perkin Elmer). Moreover, the signal intensity was represented as a pseudocolor image superimposed to grayscale photographic images of mice. The acquisition time ranged between 1 second and 1 min at binning 2, 4, and 8, depending on the signal intensity.

2.6.4. Erythropoietin levels

Erythropoietin (EPO) is a secreted 30 kD glycoprotein that is produced mainly by the kidney and the fetal liver. EPO is essential for terminal proliferation and differentiation of progenitor cells into erythrocytes, and hence it is used to treat anemia caused by kidney failure. EPO-encoding nucleic acids have been administrated into model animals to increase hematocrits[194]. Additionally, EPO is used as a model to determine potency expression efficacy and kinetics of mRNA-loaded nanoparticles. For EPO

experiments, the mice received single or multiple injections (4) of mRNA-loaded LNP at an mRNA dose from 30 and 0.3 µg. EPO levels in the plasma were measured by ELISA described in section 2.7.1 .

2.6.5.Toxicological studies

For toxicological studies, the mice received multiple injections, weekly, at an mRNA dose of 30 and 3 µg. Mice were weighed every week. At 48 h after the last injection, blood was drawn, and the serum was obtained by centrifugation of the whole blood for 3 min at 10,000 x g. Liver enzyme levels of alanine aminotransferase (ALT), aspartate aminotransferase (AST), lactate dehydrogenase (LDH), and total bilirubin levels were measured by Indiko^{tm} (Thermo Fisher Scientific, Waltham, Massachusetts, USA.). Indiko measurements were performed by (BioNTech SE).

2.6.6.Tissue preparation

Blood retrieval and serum preparations

The blood was retrieved from the retrobulbar venous plexus via a microhematocrit capillary tube (Brand, Wertheim, Germany). For serum preparations, the blood is drawn into gel pad-containing microtube (11 ml Z-Gel, Sarstedt, Nümbrecht, Germany) and centrifuged at 13,000 rpm for 5 min at room temperature (Biofuge pico, Heraeus Instruments, Hanau, Germany). After serum collection, the samples were stored at -20 °C until further use.

Isolation of splenocytes

Upon disinfection with 70 % ethanol of sacrificed mice, the spleen was excised and collected into 2-ml tubes filled with 1 ml of DPBS. Under sterile conditions, single cells were collected by pressing the spleen through a 70 µM cell strainer (Falcon, VWR, Darmstadt, Germany) with the help of the 5-ml syringe plunger. The spleen was mashed and rinsed with 2 ml of DPBS, and then the collected cell suspension was centrifuged (1200 rpm, 10 min, 4°C). The supernatant was discarded, and the cells were resuspended with 5 ml erythrocyte lysis buffer 0.1 mM EDTA in DPBS for 5-8 min. After stopping the lysis reaction with 1.5 ml of PBS, the splenocytes suspension was centrifuged (1200 rpm, 10 min, 4°C) and resuspended in 10 ml in RPMI medium. The splenocytes (diluted 1:5 in DPBS) were automatically counted with the i-CELL XR cell viability analyzer (Beckmann-Coulter, Krefeld, Germany).

Preparation of tissue for extraction of lipids

Animals were disinfected with 70% ethanol, and different organs were excised, weighed, and collected into 2-ml tubes. Appropriated volumes of DPBS were added to 2-ml tubes, e.g., 100 µl DPBS was added to 100 mg of organ. Subsequently, samples were disrupted and homogenized using a Tissuelyser (Tissuelyser II Qiagen, Hilden, Germany) by applying a frequency of 24 Hz for 10 min. From the obtained suspension, 50 µl was added to 2 ml-tubes containing 1.5 ml of a $CHCl_3$ / MeOH mixture (1:1 v/v). The tubes were vigorously mixed using a shaker (Multi Reax, Heidolph, Schwabach, Germany) for 40 min, followed by centrifugation at 10000 rpm for 10 min at room temperature (Heraeus Pico 17, Thermo Fischer Scientific, Waltham, USA.). After the supernatant was withdrawn, the extraction process was repeated two times. The extracted volumes were pooled for further LC-MS analysis (see section 2.4.5).

2.7 Techniques

2.7.1.Enzyme-linked Immunosorbent assay

Enzyme-linked immunosorbent assay (ELISA) is a plate-based assay technique designed for the detection and quantification of single analytes, such as peptides, proteins, and hormones, in serum, plasma or cell culture supernatant. In ELISA, the antigen is captured by an antibody immobilized in a microtiter plate and then complexed with horseradish peroxidase (HRP)-coupled secondary antibody. The detection is accomplished by assessing the conjugated enzyme activity via incubation with a substrate to produce a measurable product.

Mouse Erythropoietin DuoSet® ELISA

Greiner® transparent 96-well plate was coated with 100 µl of Rat Anti-Mouse EPO Capture Antibody (R&D Systems, Abingdon, UK) at 20 µg/ml in DPBS and incubated overnight at room temperature. The plates were washed three times with 400 µl washing buffer (0.05% Tween® 20 in DPBS, pH 7.2-7.4) with HydroSpeed™ plate washer. After blocking by adding 300 µl of Reagent Diluent (1% bovine serum albumin (BSA) (Sigma Aldrich, St. Louis, Missouri, USA) in DPBS, filtered 0.2 µm), the plates were incubated at room temperature for 1 h. Samples were diluted in Reagent Diluent according to the administered dose and time point the blood was drawn. After repeating the washing process, 50 µl of sample and Recombinant Mouse EPO Standard (R&D Systems, Abingdon, UK) were added to the wells and incubated for 2 hours at room temperature. A repeating washing process was followed by the addition of 100 µl/well of Biotinylated rat anti-mouse. EPO detection antibody (R&D Systems, Abingdon, UK) diluted to 10 µg/ml in Reagent Diluent and incubation for 2 h at room temperature. The plates were washed and incubated with 100 µl/well of Streptavidin-HRP (R&D Systems, Abingdon, UK) diluted 1:200 v/v in Reagent Diluent followed by a 20 min incubation at room temperature in the dark. After washing step, 100 µl/well of KPL TMB Microwell Peroxidase Substrate (SeraCare, Milford, MA, USA) resulted from 1:1 mixture of color reagent A and color reagent B was added and incubated for 20 min incubation at room temperature in the dark. The reaction was stopped by adding 50 µl/well of 2 N of sulfuric acid (H_2SO_4) solution (R&D Systems, Abingdon, UK)). The optical density was measured using a microplate reader Infinite M200 PRO (Tecan, Männedorf, Switzerland) was measured at 450 nm calculated to wavelength reference of 540 nm (Δ450–540 nm).

IgG ELISA

Recombinant Cf4/H1N1-HA protein (Life Sciences, Idstein, Germany) was biotinylated utilizing the EZ-Link Sulfor-NHS-LC-biotinylation kit according to supplier's protocol (Thermo Fisher Scientific, Germany). 96-well streptavidin plates (VWR, Darmstadt, Germany) were coated with the 100 ng/µl of biotinylated-HA protein diluted in DPBS and incubated at 4 °C overnight. After washing three times with 300 µl/well with PBS-T (0.05 % Tween20 diluted in DPBS) using Hydrospeed Plate Washer (Tecan, Männedorf, Switzerland), the plates were blocked with 250 µl of 1x BB for 1 h at 37°C in a shaker. The washing procedure was repeated, and then the serum samples were screened for HA-specific antibodies by incubation on plates for 1 h at 37°C. Plates were then incubated with HRP-labeled secondary anti-mouse immunoglobulin G (IgG) antibody for another 45 min at 37°C before. 3, 3', 5, 5'-tetramethylbenzidine (TMB) one substrate (BIOTREND, Cologne, Germany) was applied. Colorimetric

detection was monitored, and optical density read at 450nm in microplate reader Infinite M200 PRO (Tecan, Männedorf, Switzerland) calculated to a wavelength reference of 620 nm (Δ450–620nm). In some experiments, ELISAS were performed by (BioNTech RNA Pharmaceuticals, Mainz, Germany).

2.7.2.Virus Neutralization Test

Blood samples collected on 14, 30, and 56 days were analyzed using Virus Neutralization Titers (VNT). Sera were incubated with a defined amount of A/California/04/2009 virus prior to the inoculation of MDCK-II-vero cells for 3 days with the virus-serum mixture. Supernatants of infected cells were analyzed in a classical hemagglutination assay (HAI) afterward, and infectious progeny viruses that were not inactivated by antibodies in the mouse sera were detected.

To determine the level of neutralizing antibodies against HA in the serum of animals, VNTs were performed according to the manual for the laboratory diagnosis and virological surveillance of influenza (WHO Global influenza Surveillance Network). A serial dilution of serum samples starting with 1:10 were incubated for 2 h with 100 TCID50 of infectious influenza virus (A/California/04/2009). The final serum dilution and thereby the upper detection limit of this assay was 1:1280 (titration from row A to row H of a 96 well plate), if not indicated that the elongated titration scheme was used. The serum-virus mix was then applied onto confluent MDCK monolayer in Greiner U-bottom 96 well plates (Greiner Bio-One GmbH, Frickenhausen, Germany) and incubated for another 3 days. A volume of 50 µl of supernatant was thereafter incubated with 50 µl of 0.5% chicken RBC (Lohmann Tierzucht GmbH, Cuxhaven, Germany) and RBC agglutination was evaluated. The VNT titer was recorded as the inverse of the lowest dilution that inhibited agglutination (VNT/50 µl). If an elongated titration scheme was used (titrated from well 1-12 of a 96 well plate), serum samples have been titrated until a final detection limit of 1:10240. VNT experiments were performed by (BioNTech RNA Pharmaceuticals, Mainz, Germany).

2.7.3.Enzyme-Linked Immunospot Assay (ELISpot)

The enzyme-linked immunospot (ELISpot) assay is a highly sensitive immunoassay that detects the frequency of cytokine-secreting cells at the single-cell level. The cytokine IFN-γ is secreted by $CD4^+$ as well as $CD8^+$ T cells, which is a hallmark of the TH1-type phenotype, hence, high production of IFN-γ by activated T cells is typically associated with effective host defense against intracellular pathogens. For IFN-γ ELISpot assay, pre-coated 96-well plates (mAb AN18; Mabtech, Nacka Strand, Sweden) were washed three times with 300 µl sterile DPBS and conditioned with RPMI medium (200 µl/well) for 1 h at 37 °C. After, $5x10^5$ freshly isolated splenocytes were seeded per well and stimulated with 6 µg/ml with peptide Concanavalin A (Sigma Aldrich, St. Louis, Missouri, USA) (2 µg/ml) and AH1 (JPT, Berlin, Germany) at 6 µg/ml were used as a positive and negative control, respectively. After overnight culture at 37 °C with 5 % CO_2, the cell suspension was discarded, and the plates washed three times with 300 µl unsterile DPBS. The cytokine secretion was detected by adding 50 µl/well of biotinylated- INF- γ antibody R4-6A2 (Mabtech, Nacka Strand, Sweden) diluted to 1 µg/ml in DPBS complemented with 0.5 % of BSA, and incubated for 2 h at 37 °C. After washing six times with 300 µl of DPBS, 100 µl/well of Streptavidin-ALP (Mabtech, Nacka Strand, Sweden) diluted 1/1000 v/v in DPBS complemented with 0.5 % of BSA was added and incubated for 1 h at room temperature in the dark. The plates were washed

six times, and the BCIP/NBT (Mabtech, Nacka Strand, Sweden) solution was added at 100 µl/well. After 5 min, the reaction was stopped by washing thoroughly with water. Images of individual wells were captured with CTL Immunospot S6 Macro Analyzer (CTL, Shaker Heights, OH, USA), and the spot number and size were analyzed using ImmunoSpot software (CTL, Shaker Heights, OH, USA). Some of the ELISpot experiments were performed by (BioNTech RNA Pharmaceuticals, Mainz, Germany).

2.7.4.Data Analysis

All statistical analysis was conducted using GraphPad Prism 8 software. Error bars represent standard deviation (SD) (sample sizes provided in each figure). One-way ANOVA was performed when the means of three or more groups were compared against each other or to a corresponding control; when appropriated, multiple comparisons were performed using Tukey's post hoc test. Two-way ANOVA was performed when the means of three or more groups of data with independent variables are compared. Multiple comparisons were performed with Tukey' post hoc test to compare all variables and Dunnet's post hoc test was used to compare all variables to a control. P-values are defined as follows: *p<0.05, **p<0.01 and ***p<0.001. Unmarked significance indicates non-significance.

CHAPTER 3 | Results

Part of this chapter (including text and figures) is published as Sara S. Nogueira, Anne Schlegel, Konrad Maxeiner, Benjamin Weber, Matthias Barz, Martin A. Schroer, Clement E. Blanchet, Dmitri I. Svergund Srinivas Ramishetti, Dan Peer, Peter Langguth, Ugur Sahin & Heinrich Haas. Polysarcosine-Functionalized Lipid Nanoparticles for Therapeutic mRNA Delivery. *ACS Applied Nano Materials 2020;* 3 (11):10634–10645.

3.1 Optimization of State-of-the-Art Lipid Delivery Systems

3.1.1. Effect of Nitrogen to Phosphate (N/P) ratio in mRNA-LNP formulations on LNP physicochemical properties and biological activity

A crucial element of the nanocarrier design is the ratio between the carrier (lipids) and the cargo (NA). Electrostatic interactions between the positively charged nitrogen (N) in the amino lipid headgroup and the negatively charged phosphate (P) in the RNA backbone are the basis of the RNA complexation. Initial experiments focused on investigating the effect of the N/P ratio on physicochemical properties and its impact on biological activity. To this end, a lipid mixture of ionizable lipid DODMA, Chol, DOPE, and PEG-CerC16 at a molar fraction of 40:48:10:2, respectively, at increased total lipid concentration, was mixed with a luciferase-encoding mRNA aqueous solution using a microfluidic device, resulting in various N/P ratios (see section 2.3.2). The resulting LNP characteristics are summarized in Table S 1.

The particle size (top), mRNA encapsulation efficiency (middle), and the fraction of unbound mRNA (bottom) as a function of the N/P ratio are given in Figure 3.1-1. By varying the N/P ratio, colloidally stable particles of reproducible particle size (70-110 nm) could be obtained. The gradual decrease in N/P ratio at LNP formation, in excess of negative charges (N/P<1), resulted in a slight enlargement of the particle size up to 140 nm. While, in excess of positive charges (N/P>1), the progressive increase of positive charges led to a steep reduction in particle size up to 70 nm (obtained at N/P 4). No alterations in particle size were obtained with the further addition of positive charges, indicating that 70 nm is the limiting size of mRNA formulated LNP.

The mRNA encapsulation efficiency was investigated by RiboGreen assay (middle). RiboGreen is a commercial reagent dye that fluoresces only when bound to the RNA, and thus gives indication on encapsulation efficiency by discriminating between mRNA accessible and non-accessible to the fluorescent dye. Here, with an increased N/P ratio, the amount of mRNA accessible to the RiboGreen dye decreased monotonously; consequently, the mRNA encapsulation efficiency improved with the increased N/P ratio. At high N/P ratios (N/P>4) only a low fraction of mRNA was accessible to the dye (<10 %), and therefore high encapsulation efficiencies.

The bound and unbound mRNA was further investigated by agarose gel electrophoresis (Figure S 1). In the agarose gel electrophoresis, the unbound (or free mRNA) migrates towards the positive electrode, whereas the mRNA-lipid complexes remain in the pocket well, allowing to discriminate between bound and unbound nucleic acid fractions. In this case, quantitative analysis revealed that 100 % of all mRNAs were bound to the lipids/particles at N/P ratios ~ 2.5, with no further changes upon an excess of positive charges.

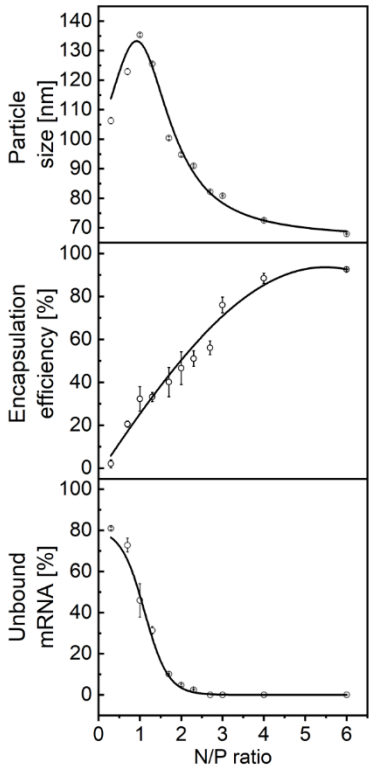

Figure 3.1-1 Characterization of LNP formulations as a function of N/P ratio.
mRNA-LNP were produced at varying N/P ratios by mixing an increased lipid concentration of DODMA:Chol:DOPE:PEG-CerC16 at respective 40:48:10:2 mol % with a constant mRNA citrate solution at pH 5.4. Analytic characterization showing a) particle size (Z-Average) measured by DLS, b) the mRNA accessibility measured by RiboGreen assay, and c) the amount of unbound mRNA measured by agarose gel electrophoresis.

The effect of the N/P ratio on the internal organization of the LNP was further investigated by SAXS and Cryo-TEM measurements. Figure 3.1-2 shows the X-ray scattering profile of LNP formulations at N/P ratio 1 to 6 (from bottom to the top). In general, the SAXS profile is characterized by smooth and steep intensity decay in the q-range of 0.03 to 7, in the log-log scale, dominated by a maximum broad peak at the moment transfer around 1 nm^{-1}, corresponding to a D-spacing of 6-7 nm^{-1} from the application of Bragg's law. Interestingly, some scattering curves display a further modulation of the intensity at q around of 0.6 nm^{-1}, corresponding to a D-spacing of ~ 10 nm, which was most clear visible for LNP with excess of lipids. In similar manner, LNP prepared in the absence of mRNA showed a single modulation at the moment transfer around 0.6 nm^{-1} (Figure S 2).

The curves are otherwise smooth and exhibit a steep intensity decay as a function of q, where a region of a linear slope, in log-log scale, in the q range below the main peak can be identified.

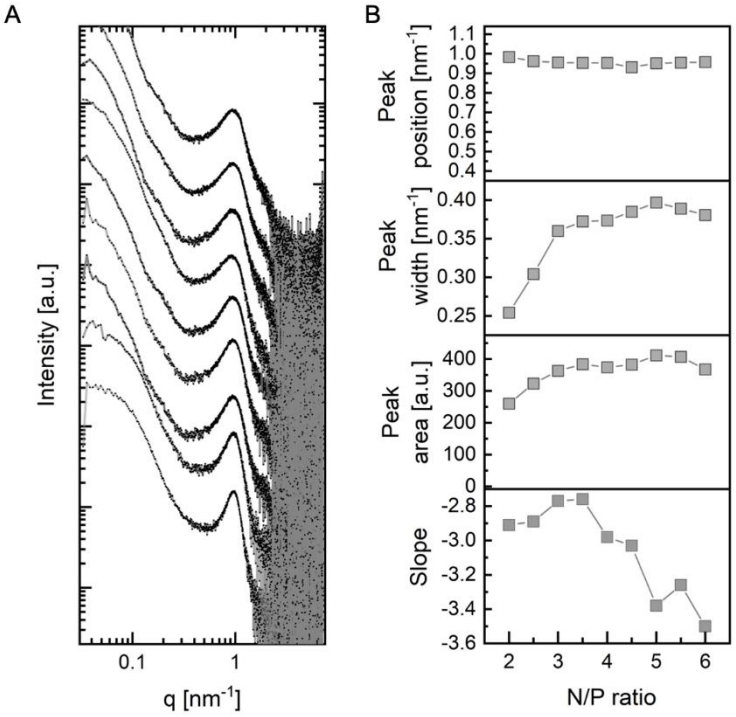

Figure 3.1-2 Small angle X-Ray scattering data of LNP as a function of N/P ratio.
LNP composed of DODMA, Chol, DOPE, PEG cerC16 at a respective 40/ 48/ 10 / 2 molar composition were formulated by microfluidic mixing at varied N/P ratio. A) Representative X-ray scattering profile of LNP as a function of N/P ratio (2, 2.5, 3, 3.5, 4, 4.5, 5, 5.5, and 6 from bottom to top). In B) peak position (q_c), peak width (w), peak area (A) of the X-rays analyzed by Lorentz fitting as a function of N/P ratio. The fourth diagram shows the Porod exponent for the scattering curves as a function of the N/P ratio.

Quantitative data analysis underlines these qualitative observations (Figure 3.1-2B**)**. Lorentzian functions were used to determine the peak positions (q_c), peak width (w), and peak area (A) of the main broad maximum, from which information on repeat distance, correlation length, and relative amount of material present in such organization can be derived (see section 2.4.4 for more details). The peak positions (q_c), maintained rather constant as a function of the N/P ratio, indicating there is no alteration on the repeat distance of the lipid layers. Further, the peak width, indicating the correlation length (ξ=1/s), increased slightly, and thereby the correlation length slightly decreased. Accordingly, the peak area, which is indicative of the material contributing to the diffraction pattern, enlarged with increasing N/P ratio. Since the increase in the peak area is not proportional to the excess of the lipids, it can be derived that both RNA and lipid phases might have contributed to the SAXS profile.

The range of smooth decay at lower q values was analyzed using a power law ($I \approx q^{-x}$), where from the exponent, x, the mass fractal dimension of the particles can be derived (Porod exponent). A Porod exponent of −4 is indicative of ideally smooth interfaces, lower (negative) numbers, e.g., −4 to −3, is thought to be induced by surface roughness (surface fractals), while slopes between −3.5 and −2 point toward mass fractals. The Porod exponents seems to increase with increased N/P ratio; therefore, the surface and/or the mass fractal dimension decrease, which could be an effect of increased surface roughness, changes in packing, or anisotropy.

The structure of LNP was further characterized with Cryo-TEM measurements. In Figure 3.1-3, representative Cryo-TEM images of N/P 2, 3, and 4 are depicted. Cryo-TEM images revealed the co-existence of vesicular particles with one or two lipid-bilayers, with electron core dense and particles with

electron-bright core commonly referred to as ‘blebs’ structures. Notably, the quantity of ‘blebs structures’ present in the formulation increased with the increasing N/P ratio.

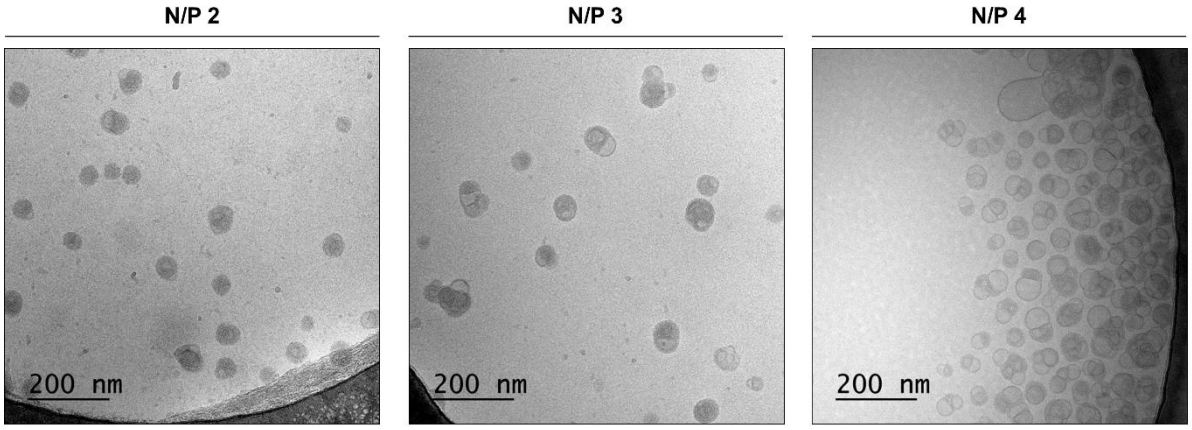

Figure 3.1-3 Representative cryo-TEM micrographics of LNP formed at N/P ratio 2, 3, and 4.
Scale bar=200 nm.

The biological activity as a function of the N/P ratio is given in Figure 3.1-4**.** The protein expression was evaluated 24 h post-transfection with LNP at an mRNA dose of 50 ng/well in murine myoblast (C2C12) and macrophage (RAW 264.7) cell lines using a luciferase assay. In both cell lines, a steep improvement in the activity was obtained up to N/P 4, whereas only a mild improvement could be obtained with further addition of positive charges.

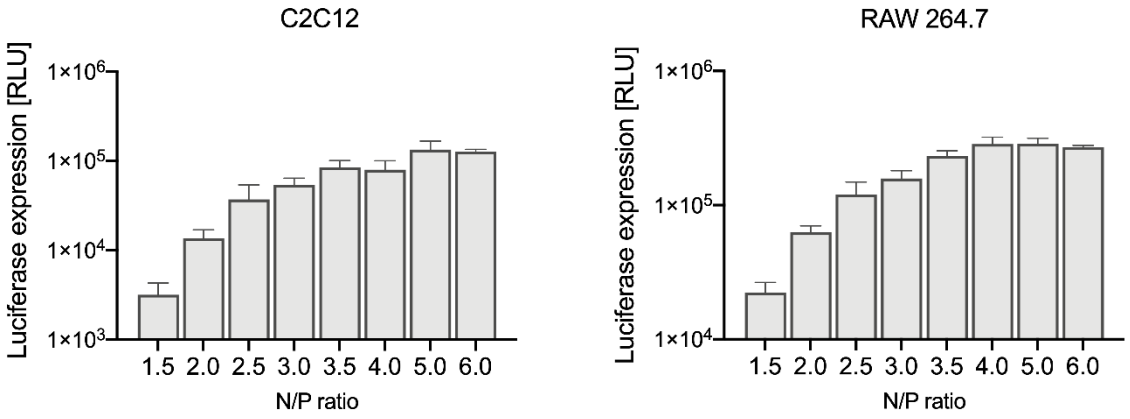

Figure 3.1-4 Biological activity as a function of N/P ratio in murine myoblast and macrophages cell lines.
Luciferase expression was measured 24 h post-transfection with mRNA-LNP at 50 ng/well. Data are presented as mean ± SD of three technical replicates.

The results indicated that lipid nanoparticles complexed with mRNA are compact particles with smooth interfaces, with a low internal organization, in the sense that only a few repeat units are present in organized stacks. Besides, the SAXS and Cryo-TEM point towards the co-existence of two phases, an RNA-rich and RNA-poor phase, within the LNP formulation, which the latter increased with increasing N/P ratio mRNA-loaded LNP and ‘bleb structures’ or empty vesicles. It is plausible to hypothesize these structures correspond to the ‘blebs structures’ previously described by Leung *et al*. in mRNA and DNA-loaded LNP, which they argued were indicative of the segregation of bilayer-preferring lipids such as DSPC. These ‘bleb structures’ were not observed for siRNA-LNP, which suggested that the nanostructure packing of lipid around the shorter siRNA oligonucleotides in the core does not lead to

such rapid lipid segregation[195]. The increased presence of bleb structures with increasing N/P ratio, correlates with decreasing mRNA accessibility and increased expression *in vitro* up to N/P ratio of 4. These results are an indication that additional lipids, which do not interact with the encapsulated mRNA, should be available to protect the mRNA and foster endosomal escape, as previously suggested [66]. The current LNP for mRNA are manufactured at N/P ratio 6, which would represent a very excessive number of 'blebs' in this case, and thereby impair the LNP stability. Therefore, the N/P ratio used for further studies with mRNA-lipid formulations was 4.

3.1.2. The Effect of Manufacture Procedure of RNA-Lipid Formulations as Function of Particle Size

Various techniques for formulating NA have been previously proposed in Section 1.2.3. In general, clinically relevant lipid systems can be prepared by two different preparation methods and are categorized such as LPX, where pre-formed cationic liposomes are mixed with mRNA, or LNP, where lipids dissolved in ethanol are combined with an acidic mRNA solution commonly by rapid mixing techniques. Thus, this section aimed to investigate the differences and similarities between identically composed LPX and LNP formulations. For this purpose, a lipid mixture of ionizable lipid DODMA, Chol, phospholipid DOPE, and PEG-CerC16 to a molar fraction of 40:48:10:2, was mixed with luciferase-encoding mRNA at N/P 4 to formulate LPX and LNP accordingly to Figure 3.1-5.

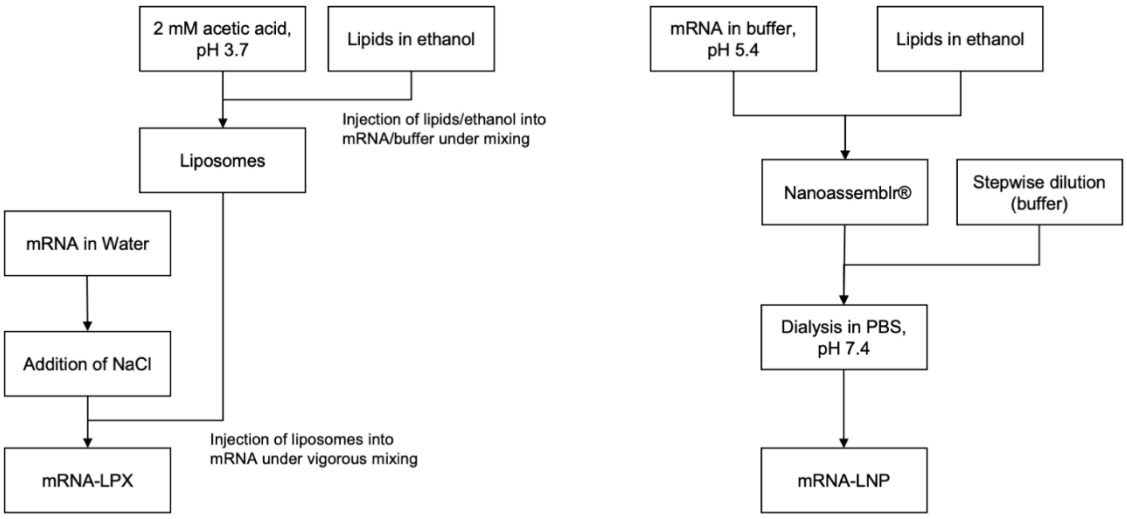

Figure 3.1-5 Scheme of LNP and LPX preparation.

Ionizable-based liposomes prepared by the ethanol injection method exhibiting particle sizes of 180 nm on average. When ionizable-based liposomes were mixed with mRNA using a sequential protocol, in the presence of 120 mM of NaCl (according to section 2.3.1), mRNA-lipoplexes displayed a monodisperse particle size of 200 ± 30 nm in diameter. On the other hand, LNP prepared by mixing an ethanolic mixture with an mRNA solution using the microfluidic device (according to section 2.3.2) displayed a particle size of 80 ± 15 nm in diameter. Further analysis revealed that despite all mRNA was bound to the lipids/particle, the mRNA accessibility to the RiboGreen dye was higher in LPX than LNP systems (52 % vs. 20 %), which could be explained by a possible higher localization of the ionizable

lipids on the surface of the LPX[127]. The ξ-potential of LPX and LNP was similarly neutral when measured at physiological conditions (data not shown).

It is worth noting that particle size is a determinant physicochemical characteristic[126]; thereby, the effect of the size, as a function of manufacturing protocol was investigated in this section. The particle size of LNP can be varied by adjusting the mixing parameters (FR and FRR); the particle size was enlarged from ~ 80 to ~200 nm by decreasing the FFR from 3:1 to 1:1 (Aqueous: Organic) and the FR from 12 to 6 ml/min (data not shown). On the other hand, the particle size of LPX formulations can be controlled by adjusting the initial liposome concentration; increasing the starting liposome concentration (from 1.2 mM to 2.4 mM) during the mixing procedure resulted in a decrease from 200 to 100 nm. The physicochemical characteristics of the mRNA-lipid formulations are summarized in Table 3.1-1.

Table 3.1-1 Summary of the physicochemical characteristics of mRNA- lipid nanoformulations.

Lipid vehicle	*Z-Average [nm]*	*PdI*	*Accessibility mRNA [%]*	*Zeta Potential [µm.cm/V.s]*
100nm-LNP	83 ± 1	0.158 ± 0.01	14 ± 2	4.93 ± 3.91
200nm-LNP	201 ± 10	0.142 ± 0.01	32 ± 10	4.17 ± 3.4
100nm-LPX	108 ± 2	0.133 ± 0.03	31 ± 3	2.59 ± 3.39
200nm-LPX	201 ± 9	0.141 ± 0.01	46 ± 1	3.82 ± 3.28

The resulting LNP particles exhibited a monodisperse particle size of 83 nm and 201 nm, with PdI inferior to 0.16. On the other hand, LPX formulations displayed a 108 nm and 201 nm diameter, with PdI lower than 0.14. It is worth noting that the LPX protocol did not enable the production of ~ 80 nm nanoparticles in these conditions. For simplification of results, herein referred to as 100 -nm-LNP. Further analysis revealed that 200 nm-particles showed higher mRNA accessibility to the RiboGreen dye than 100 nm-systems, independently of the manufacturing procedure. Nevertheless, all mRNA was bound to the lipid/particle when analyzed by agarose gel electrophoresis (Figure S 3). All systems exhibited similar neutral surface charges.

To gain further understanding of the molecular coherences, the particle surface was investigated by zeta potential and hemolysis assay (Figure 3.1-6). The surface charge was studied at a pH of 5.5 (pH < pKa of the ionizable lipid) in deionized water to reduce charge screening by negative counterions and evaluate the protonation level. The Zeta potential was significantly higher for LPX than from LNP, which could indicate a higher surface charge of LPX than LNP systems. Of note, the manufacturing procedure of LPX resulted in slightly more acidic RNA-lipid formulations than LNP method. Despite not significant, 200 nm-sized particles also displayed slightly higher zeta potential than 100 nm particles. In addition, the cationic charge of the lipid particles was assessed by a hemolytic assay based on the electrostatic interaction between the particles' positive surface and the anionic membranes of RBCs. In general, LPX induced a higher RBC lysis than LNP, which was statistically significant for 200 nm sizes (<0.0001), which is indicative of a higher surface charge. Furthermore, large particles induced higher hemolysis than small particles when prepared as LPX (p=0.0027), whereas no difference was obtained for LNP particles. Alternatively, RBC hemolysis can be used to surrogate for endosomal escape (pH 5.4) and toxicity (7.4)**.** The results indicated that LPX might cause a certain level of toxicity; however, it is worth noting that RBCs lysis by LPX was dose-dependent (data not shown). At endosomal pH (5.4),

both LPX and LNP systems displayed higher hemolytic activity than at pH 7; LPX systems still induced higher lyses than LNP formulations, which might indicate an increased endosomal release from late endosomes.

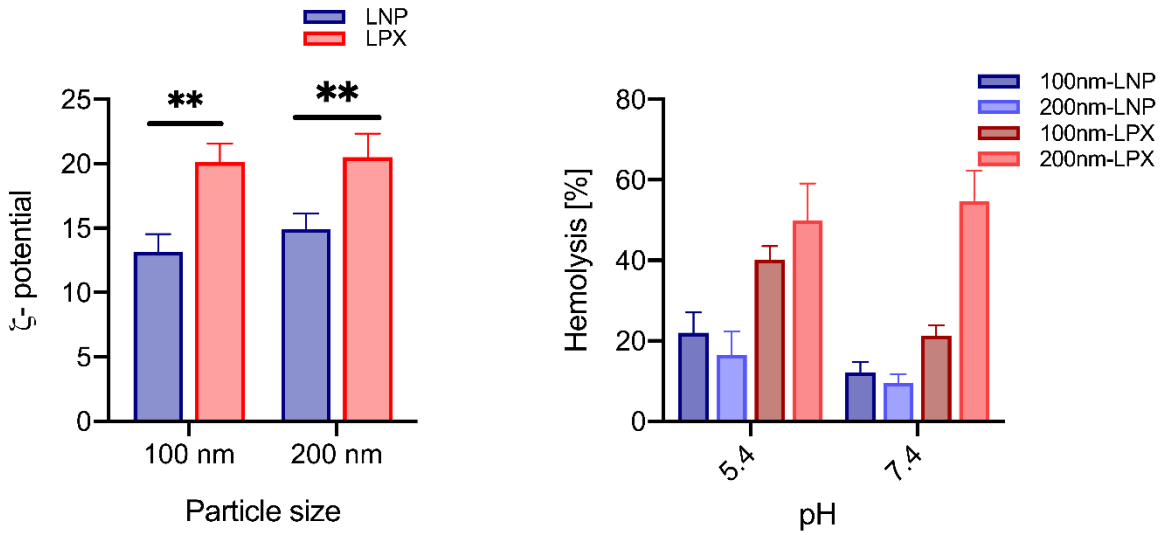

Figure 3.1-6 Surface charge of LPX and LNP nanocomplexes as a function of particle size.
A) Zeta potential of LPX and LNP nanoformulations. Zeta potential was measured at pH = 5.5 in RO/DI water. B) Hemolytic activity of LPX and LNP formulations as a function of pH. The relative hemolysis compared to complete hemolysis (100%) induced by Triton X-100 is shown.

The impact of the manufacturing procedure on the structure was further investigated by SAXS. Figure 3.1-7 shows the representative X-rays scattering profiles LPX and LNP nanocomplexes, as a function of particle size.

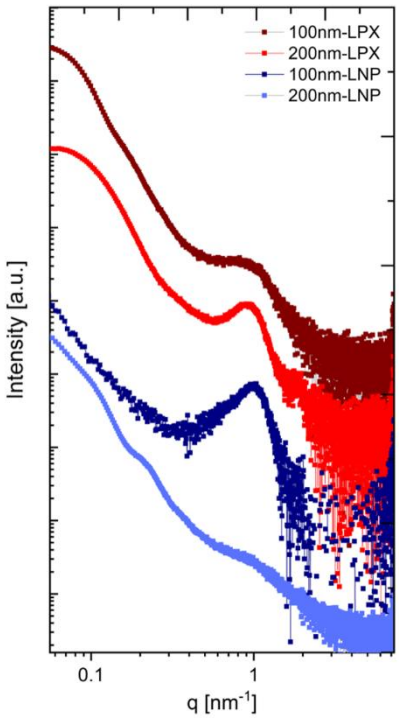

Figure 3.1-7 Small angle X-rays scattering data from LPX and LNP nanocomplexes as a function of size.

The mRNA-lipid formulations were manufactured as LNP (blue curve) and LPX (red curve) with a particle size of 100 (dark) and 200 nm (light).

In general, the scattering profile of LPX and LNP formulations is relatively similar, with a smooth and steep intensity decay in the q-range of 0.03 to 0.3, in the log-log scale, dominated by a maximum broad peak at the moment transfer around 1 nm^{-1} (quantitative analyses in Table S 2). The results are in agreement with those described previously by Kubota and colleagues. where ionizable lipid-based LPX (~150 nm) and LNP (~100 nm) adopted similar structures even though their diameters differed[127].

Surprisingly, the x-ray profile of 200nm- LNP showed no maximum broad peak, only very weak modulations, which could be indicative of an uncorrelated distribution of scattering units inside the particles. Further experiments will be necessary to reveal the foundation of this effect on the internal organization. Various conditions which were applied for manufacturing the different sample types may be correlated with these findings. Currently further systematic research, beyond the scope of the present thesis, is ongoing in order to elucidate these coherencies

Further experiments focused on the impact of the manufacturing procedure on the fate and potency of lipid nanoparticles. Data in Figure 3.1-8 shows the biodistribution of luciferase expression 24h after IV administration of 2 µg of mRNA-lipid systems into Balb/C mice. LPX and LNP formulations targeted mainly the liver and spleen. The luciferase expression of LPX and LNP with 100 nm sizes were similar in the liver and spleen, while 200 nm-LNP mediated significantly higher expression that 200nm-LPX in both liver and spleen ($P<0.01$). Moreover, nanoparticles with 100 nm sizes targeted the liver preferentially, whereas 200 nm sizes favored the spleen target. Surprisingly, the increase in LNP particle size mediated a 22- and 109- fold improvement in luciferase expression in the liver and spleen, respectively. It is also important to highlight that enlargement of LPX sizes resulted in improved protein expression in the liver and spleen, however, to a lesser extent than with LNP formulations.

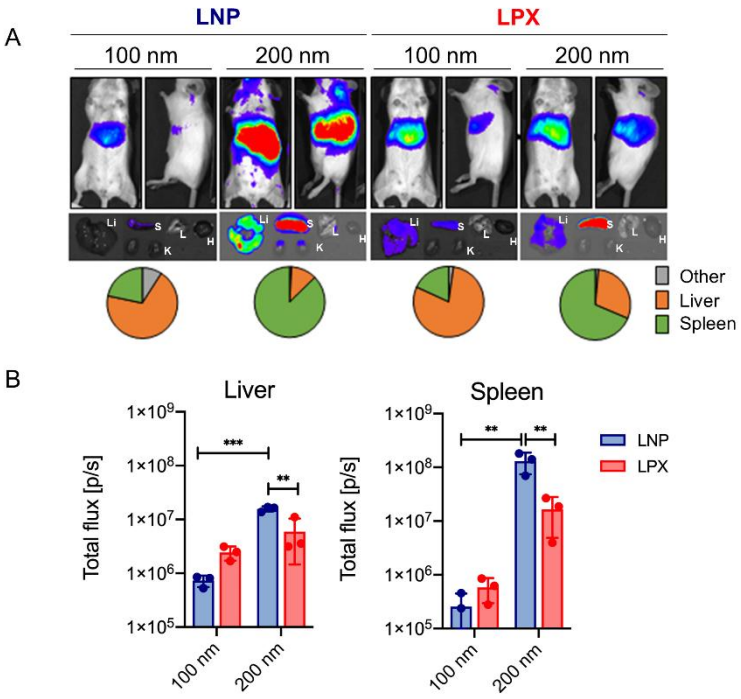

Figure 3.1-8 Biodistribution of luciferase expression of sized controlled mRNA-nanocarriers.

Luciferase expression measured 24 h after administering mRNA at 2 µg IV in Balb/C mice (n=3 per group). A) Representative images of the whole mice and extracted organs: heart (H), lung (L), liver (Li), spleen (S) and kidneys (K) and B) graphical display of luminescence in the liver and spleen. Data are presented as mean ± SD. Statistical analysis was performed with two-way ANOVA with Tukey's multiple comparison test (*P <0.05, ** P<0.01, ***P<0.001).

The kinetic profile and potency of mRNA-lipid formulations was investigated by using a relevant therapeutic mRNA encoding for EPO after IV injection (Figure 3.1-9). The resulting mRNA-lipid formulations showed similar physicochemical to those described previously for mRNA encoding luciferase (summarized in Table S 3). Figure 3.1-9A illustrates that levels of secreted EPO were dictated by the particle size, where enlargement of particle size significantly improved EPO secretion, independently of manufacturing protocol. A similar pattern was found for other administration routes such as IP, IM, and SC (Figure S 4).

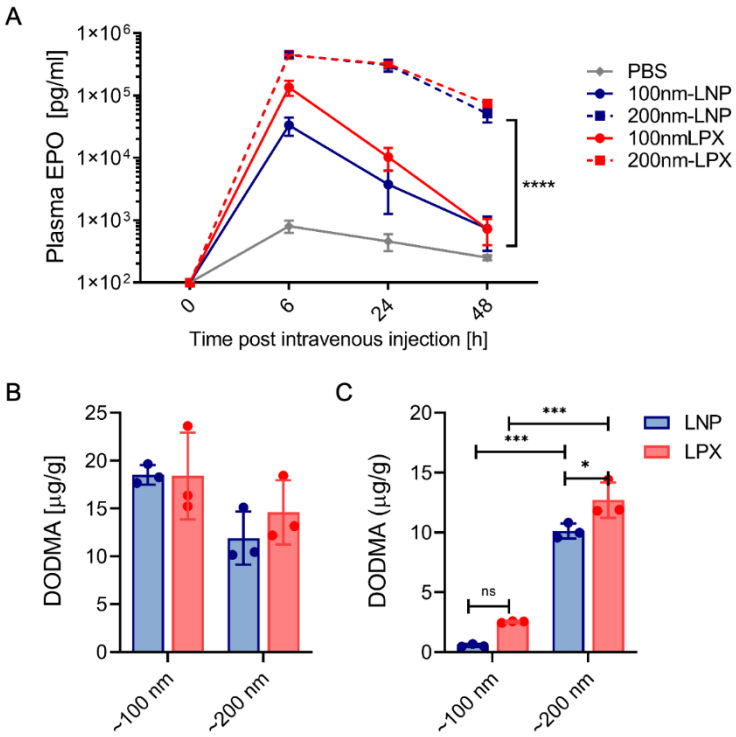

Figure 3.1-9 Kinetics profile of EPO encoded mRNA-nanoformulations.
A) EPO mRNA-complexes were IV administrated at mRNA concentration of 3 µg into Balb/C mice (n=3 per group). Data are presented as mean ± SD. Statistical analysis was performed with Two-way ANOVA with Tukey test (*P<0.05, **P<0.01, ***P<0.001). Lipid (DODMA) concentration (µg/g) after IV administration of mRNA in the (B) liver and C) spleen 24 h post-injection (n=3 per group). Data are presented as mean ± SD. Statistical analysis was performed with Two-Way ANOVA with Tukey test (*P <0.05, ** P<0.01, ***P<0.001).

The levels of ionizable lipid DODMA in the different tissues (heart, lungs, liver, spleen, and kidneys) were investigated by LC-MS measurements. The mRNA nanoformulations were injected at 2 µg of mRNA, which is equivalent to 120 µM of DODMA. In Figure 3.1-9B/C is depicted the amount of ionizable lipids detected in the liver and spleen since residual amounts were found in the lung, heart, and kidneys. A maximum of 44 µM of ionizable lipid was detected in the organs by LCMS, which corresponded to a lipid recovery of 36%.. Interestingly, slightly higher amounts of DODMA were found in the organs when mRNA was delivered as LPX compared to LNP (44 vs 35 µM) and with larger particle instead small

particles (33 vs 44 µM). Slightly lower amounts of cationic lipid were found for 200 nm nanocarriers in the liver, whereas significantly higher DODMA concentrations were found in the spleen for 200 nm vehicles compared to 100 nm counterpart. Besides, similar levels of DODMA were found in the liver and spleen when mRNA was delivered into 200 m nanocarriers, suggesting that large particles target simultaneously both organs. While 100 nm vehicles resulted in a higher concentration of DODMA in the liver and low in the spleen.

The *in vivo* cell biodistribution of LPX and LNP complexes was further explored with the help of miRNA target sequences. miRNA are non-coding RNA molecules that are cell type specific and post-transcriptionally repress gene expression; this is mediated by interaction with complementary target sites in the 3′ UTR of target mRNAs. Specific miRNA target sequences were included in the luciferase-encoding mRNA:

1) miR122, which specifically represses luciferase expression in hepatocytes.
2) miR142-3p, which reduces the expression in hematopoietic cells.
3) miR650, which is used as a negative control of luciferase activity.

The physicochemical characteristics of miRT-encoding mRNA nanocarrier are comparable to those described previously for mRNA encoding luciferase (data not shown). Figure 3.1-10 shows the cell biodistribution mediated by mRNA-loaded nanocarriers at 24h post-injection of 2 µg. Systems complexed with mRNA incorporating of miR-122 and miR143-3p significantly reduced the luciferase expression in the liver ($p<0.001$)**.** While only systems that contained the miR143-3p mediated a reduction in the spleen (not statistic significant). Furthermore, by incorporating miR122 binding sites, the expression was reduced significantly more with smaller than with larger formulations. In opposite, the expression was substantially reduced for large nanocarriers with the inclusion of miR143-ep binding sites. These data indicated that 100 nm formulations seem to target hepatocytes more efficiently, while 200mn-formulations target more prominently hematopoietic cells (thus probably Kupffer cells) in the liver.

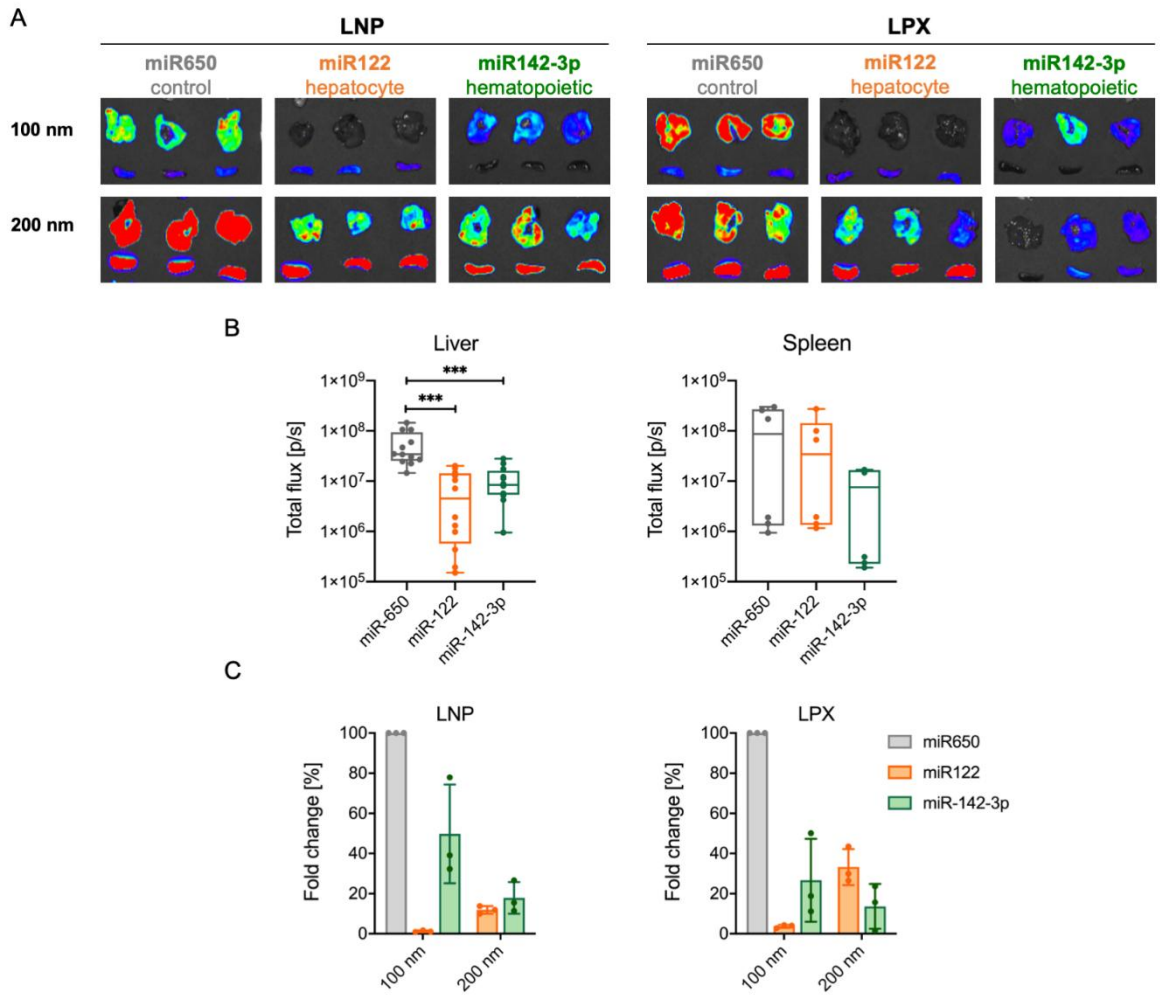

Figure 3.1-10 In vivo liver cell targeting of size controlled nanocarriers.
In vivo liver cell targeting was determined by injecting lipid systems formulated with mRNA containing miRNA target sequences specific for different liver cells. miRNA-loaded LNP were administrated IV at mRNA concentration of 2 µg into Balb/C mice (n=3 per group). A) Representative images of organs 24h after IV administration of LNP complexed mRNA encoding miR122, miR1435-3p, and miR650 binding sites. B) Graphical display of luciferase expression in the liver and spleen 24h after IV administration of LNP; Statistical analysis was performed with One-Way ANOVA compared to the control (miR650) (*P<0.05, ** P<0.01, ***P<0.001). C) Fold change of expression over the miRNA control (miR650) in the liver, as mean ± SD. Statistical analysis was performed with ANOVA with the Tukey test (*P<0.05, ** P<0.01, ***P<0.001).

Since hematopoietic cell transfection may be associated with proinflammatory cytokine release (inflammation), a preliminary analysis was conducted *in vitro* with macrophage RAW 264.7 cell line (Figure S 5). Preliminary results showed no increase in cytokine release (IL-6 and TNF-α) upon *in vitro* incubation with the macrophage cell line.

In summary, identically composed nanoformulations manufactured as LPX and LNP comprising ionizable lipid adopted similar structures. Lipid nanocarriers manufactured with LPX procedure showed higher zeta potential, hemolysis, and mRNA accessibility compared to LNP, supporting the hypothesis that the ionizable lipids might be more localized on the surface of the LPX, as previously described[127]. However, similar levels of secreted EPO were observed when LPX and LNP of similar sizes were administration to mice. A significant improvement in the potency was obtained by increasing the sizes of LNP and LPX from 100 to 200 nm. Biodistribution studies indicated that nanoparticles with 100 nm

target preferentially hepatocytes in the liver, while 200 nm-particles target simultaneously hematopoietic cells and hepatocytes, and thus both liver and spleen.

The results in this section indicated that particle size, rather than manufacture procedure, dictated the potency of lipid nanoparticles, allowing the use of alternative manufacturing procedures and according to good manufacturing practice (GMP) requirements for production of potent and safe lipid vehicles. Moreover, it expands accessible technological space for manufacturing of lipid nanoparticles for functional mRNA delivery (e.g., size control.

3.1.3.Structure-Function Correlations of Lipid Components in RNA-LNP

The lipid composition is another known factor that can determine physicochemical properties and lipid systems' biological fate and potency. In this section, the impact of ionizable lipid, helper lipids, and Chol, and finally, the stealth-lipids on the physicochemical properties and their effects on biological activity will be systemically investigated.

Ionizable lipids

The ionizable cationic lipid interacts with negatively charge mRNA enabling its encapsulation and fostering the endosomal release into the cytoplasm. Therefore, ionizable lipid design is a key parameter in nucleic acid delivery by lipid nanoparticles. To this end, a library of newly synthesized ionizable lipids was evaluated for mRNA delivery (Figure 3.1-11). Preliminary experiments showed that lower amounts of ionizable lipids were necessary to deliver mRNA compared to siRNA (40 vs 50 %) (data not shown). which could be explained by the smaller surface area per base of mRNA[195]. The molar % of ionizable cationic lipid was kept constant in further experiments. Each member of the lipid library (at 5.4 mM) was mixed with co-lipids DSPC, Chol, and PEG-CerC16 (40:10:48:2 mol %) and formulated with mRNA encoding luciferase protein by Nanoassemblr® device. As a control, the innovative ionizable lipids were compared with DODMA (internal control) and MC3 lipid[50].

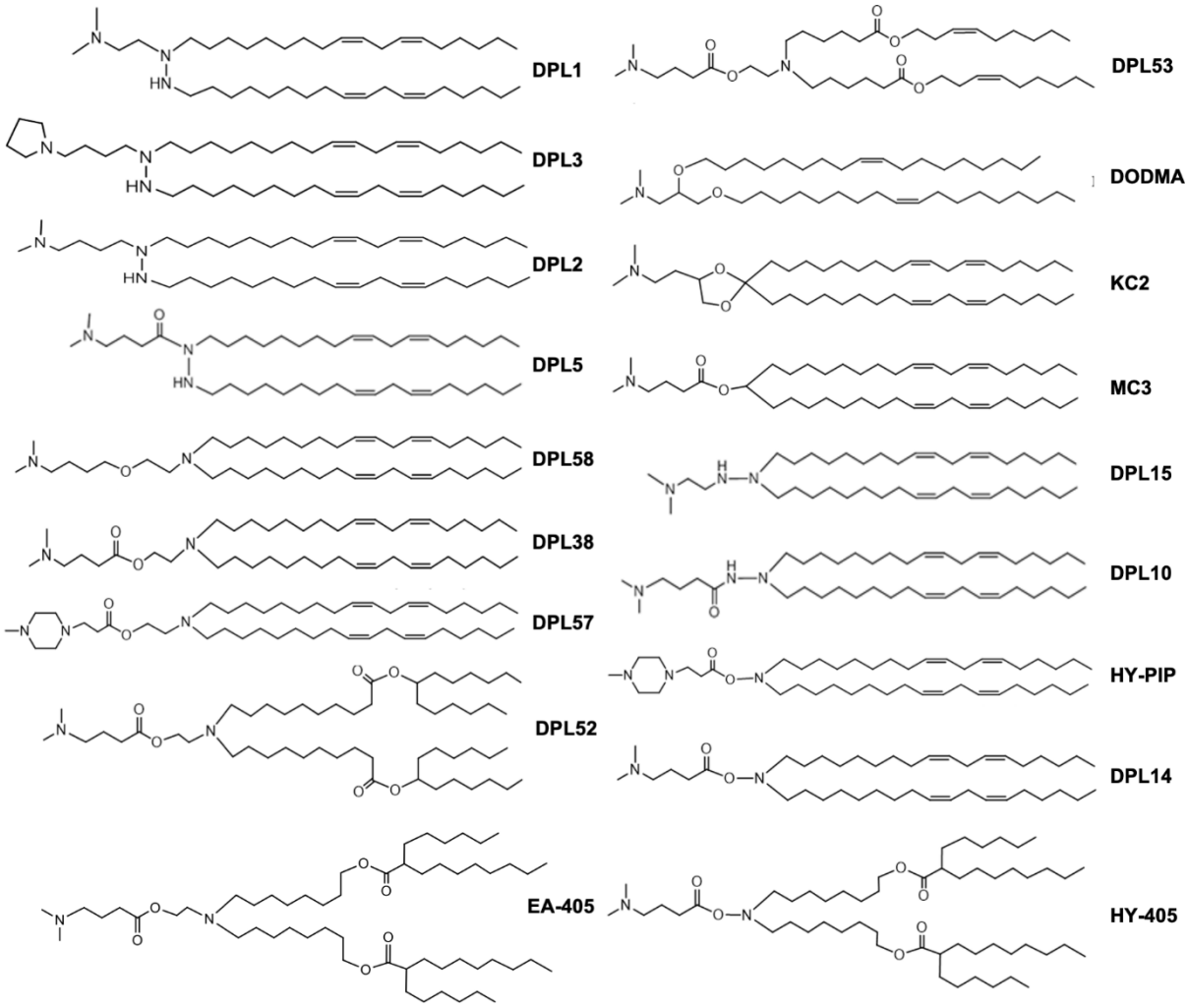

Figure 3.1-11 Structure of ionizable cationic lipids.

In Figure 3.1-12, particle size (top), mRNA accessibility (middle), and pKa (bottom) are plotted as a function of ionizable lipid. The majority of the ionizable lipids resulted in the formation of colloidally stable LNP, where a monodisperse particle distribution (PdI<0.25) with sizes ranging from 80 to 150 nm was obtained by DLS measurements. Interestingly, tail branching did not always result in increased particle size. Further analysis showed that the majority of ionizable lipids resulted in relatively low mRNA accessibility (<20 %) to the Ribogreen dye. Lastly, the pKa of the ionizable lipid was investigated using a TNS assay. TNS is a negatively charged fluorescent dye that only fluoresces when associated with the surface of positively charged membranes in aqueous solutions. In this study, empty LNP (without mRNA) were titrated in a series of buffers with pH ranging from 3.5 – 9. It worth highlighting that pKa herein represent the overall LNP formulation since co-lipids are considered. The pKa of the formulated LNP varied between 5.4 and 7.8. The LNP comprising MC3 lipid showed a pKa of 6.29, which is relatively similar to the 6.44 reported in the literature[71].

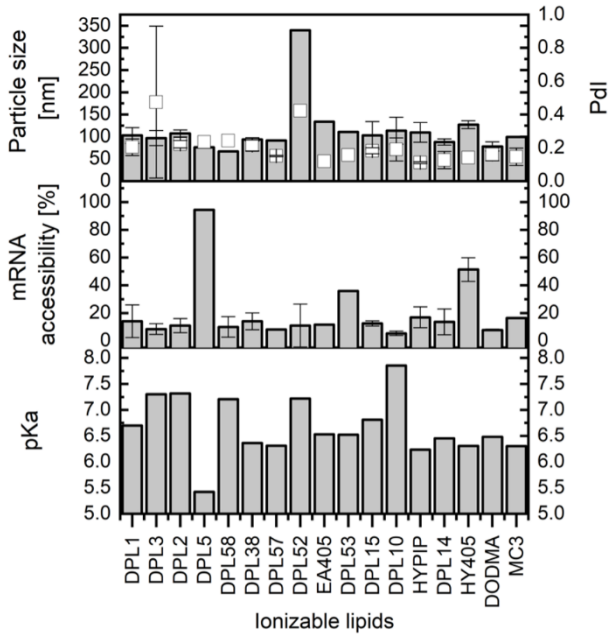

Figure 3.1-12 Physicochemical properties of LNP formulated with innovative ionizable lipids.
LNP were formulated with ionizable lipids, Chol, DSPC, and PEG CerC16 at respective 40/48/10/2 mol %. A) Particle size (bars) and PdI (scattering dots) of LNP formulations measured by DLS; B) mRNA accessibility of LNP formulations measured by the Ribogreen assay. C) pKa analysis of ionizable lipid by TNS assay.

The ability of the ionizable lipids to foster endosomal release was investigated by an RBC hemolysis assay. Figure 3.1-13 shows the hemolytic activity of ionizable lipids as a function of pH. Even though the majority of ionizable lipids were non-hemolytic at physiological pH, ionizable lipids 3, 10, 52, and 58 induced a substantial RBC hemolysis indicating potential systemic toxicity. At pH 5.5, the ionizable lipids EA405, DPL52, DPL53, DPL14, and DPL10 showed high hemolytic activity, and thus possible higher endosomal escape. Notably, LNP comprising lipid DPL14 and DPL53 showed a high hemolytic ratio, the ratio between the hemolysis at pH 5.4 and pH 7.4, which indicates potentially high endosomal release without mediating toxicity.

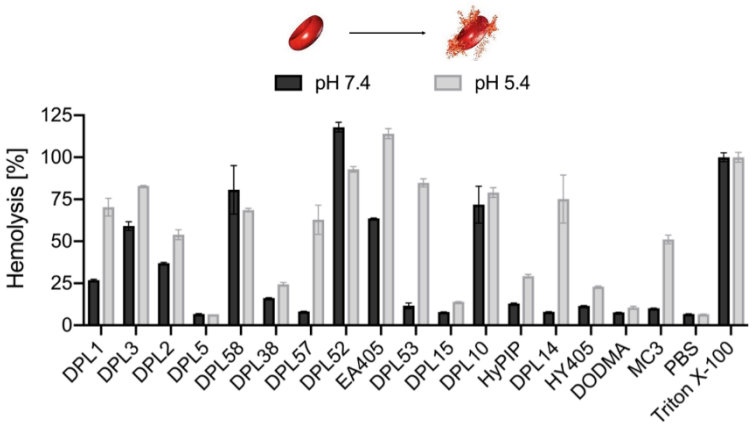

Figure 3.1-13 LNP-mediated hemolysis of RBCs at pH 5.5 (grey) and 7.4 (black).
Error bars represent SD, n = 1, with three technical replicates.

The potency of ionizable lipids was further analyzed in different cell lines representative of different tissues (HepG2 (hepatocytes), RAW 264.7 (macrophages), and C2C12 (myoblast). In Figure 3.1-14 is depicted the $\log_2$ fold change in luciferase expression compared to internal control. The

majority of ionizable lipids mediated luciferase expression in the various cell lines, where only a small number of formulated ionizable lipids mediated higher expression than the internal control. DPL14 ionizable lipid mediated up to 3-fold improvement over MC3 lipid. Of note, the DPL14 was included in the LNP at similar molar concentration than MC3, however DPL14 has 2 amines, therefore the overall N/P ratio of DPL14 is 8. While MC3 only displays 1 amine, and thus a N/P of 4 is obtained. In agreement with transfection efficiency *in vitro*, DPL14-based LNP showed the highest hemolytic ratio, (high endosomal escape associated with low toxicity), and pKa between 6.4-6.6. It is also essential to note that the ionizable lipids did not induce substantial cytotoxicity at the tested doses (data not shown).

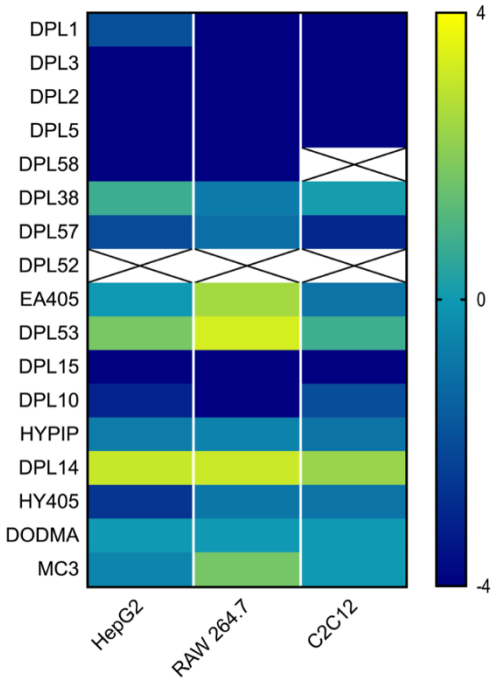

Figure 3.1-14 Activity of ionizable lipids in distinct types of cell lines.
Luciferase expression in transfected cells after 24 h incubation with 50 ng of mRNA. Data are represented as log_2 fold change compared to internal control (low expression (blue) and high expression(green).

For further studies, the *in vivo* performance of DPL14 ionizable lipid was evaluated under systemic and local applications. Data in Figure 3.1-15 shows the performance of the ionizable lipids after IV (via retro-orbital) and IM (via tibialis posterior) administration of the LNP in Balb/C mice. Luciferase activity was measured by whole mice imaging. The DPL14-based LNP target the liver when administrated IV, while both liver and injected muscle show luciferase expression after IM administration. Remarkably, DPL14 ionizable lipid-mediated a significant improvement in luciferase expression over our internal control in both liver and injected muscle (Figure 3.1-15A). In a more relevant therapeutic setting, DPL14-formulated LNP also resulted in high levels of EPO secretion under IV and IM application (Figure 3.1-15B). In opposite, DODMA-formulated LNP mediated protein levels below the detection limit of ELISA (data not shown).

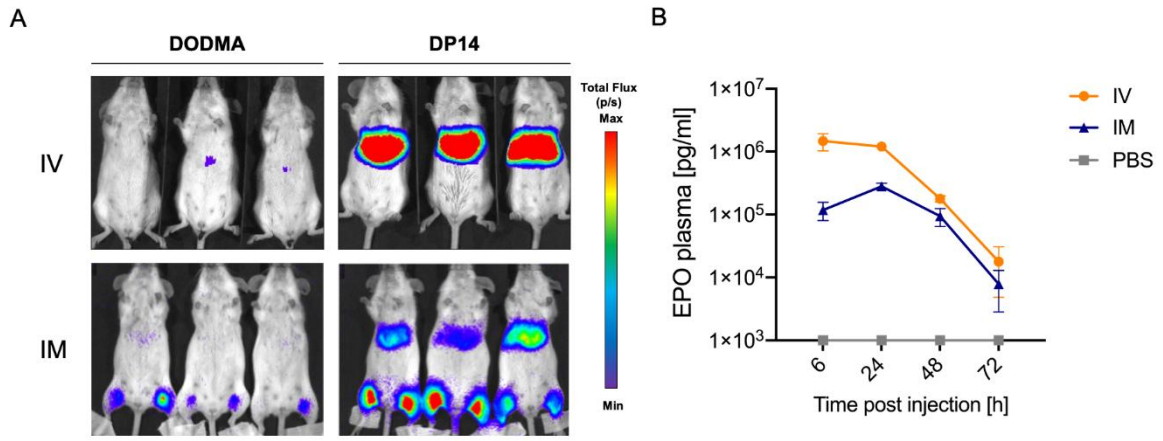

Figure 3.1-15 In vivo performance of ionizable DPL14.
A) Representative images of luciferase expression 6 h post IV and IM administration of 10 µg of mRNA-LNP into mice (n=3/group). B) EPO profile of DPL14-LNP after IV and IM administration of 3 µg of mRNA-LNP. Data is presented as average of n=3, with SD.

Finally, structure-activity relationships were investigated between the physicochemical properties of the LNP formulations, including particle size, mRNA accessibility, and pKa, and biological activity (Figure S 6). No correlations were found for LNP particle size and mRNA accessibility. A nonlinear correlation was found between LNP pKa, hemolytic ratio, and *in vitro* expression. All the top performers exhibited pKa between 6.2 and 6.6, which also showed high hemolytic ratio (>2) and mediated the highest expression in three different cell lines. Similar optimal pKa was obtained for the different cell lines (data not shown). These data indicate that the charge state of the LNP has an influence on the performance of LNP, which are in line with recent publications[104,181].

In summary, these results indicated that ionizable lipids play a crucial role in LNP potency. Besides, it showed that the charge state of LNP formulation influences the transfection efficiency, and thereby pKa and hemolytic ratio might be suitable parameters for potency prediction. Finally, these results illustrated that DPL14 ionizable lipid is a promising candidate for mRNA delivery.

Helper Lipids and Cholesterol

In addition to ionizable lipid, LNP are typically composed of helper lipids (phospholipids) and cholesterol that contribute to LNP stability and delivery efficiency. Phospholipids with cone-shape geometry that favors the formation of hexagonal phase II (such as DOPE) can foster endosomal release, while cylindrical-shaped lipid phosphatidylcholine that promotes bilayer structures (DSPC) can provide greater bilayer stability Cholesterol is often included to fill up the spaces between the lipids in the LNP and therefore contributes to LNP stability and activity. Therefore, a set of experiments was conducted to determine the impact of the helper lipids on the mRNA-based LNP physicochemical properties and biological performance and identify the ideal helper lipid for optimal mRNA delivery. For this purpose, commonly used phospholipids such as DSPC, DOPC, and DOPE were incorporated into the LNP by the gradual replacement of Chol. To this aim, LNP were formulated using DODMA, Chol, phospholipid (DOPC, DSPC, DOPE), and PEG-DMG at 40/50-x/x/2, where x represents the mol % of helper lipid, at N/P ratio 4, by microfluidic mixing.

In Figure 3.1-16, particle size (top), mRNA accessibility (middle), and the luciferase activity (bottom) are plotted together as a function of the molar fraction (%) of the helper lipid. For the particle size**,** the progressive incorporation of DSPC and DOPC resulted in the enlargement of the particle size, while for DOPE, the particle size only increased up to 30 mol % followed up by a reduction in the size with further addition of phospholipid. Similarly, an increment in mRNA accessibility to the RiboGreen dye was observed upon the progressive incorporation of DSPC and DOPC, and therefore lower encapsulation efficiency. In the case of phospholipid DOPE, the mRNA accessibility increased only up to 30 %, which was followed by a slight reduction with additional phospholipid content. Finally, the bottom graph depicts the luciferase expression in RAW 264.7 cells transfected with mRNA-LNP at 50 ng/well. Notably, the progressive incorporation of DOPE improved the luciferase activity, while incorporating increased mol % of DOPC and DSPC leads to a reduction in the protein expression, more prominently for the phospholipid DSPC. In all the conditions, DOPE formulations lead to improved luciferase expression *in vitro*.

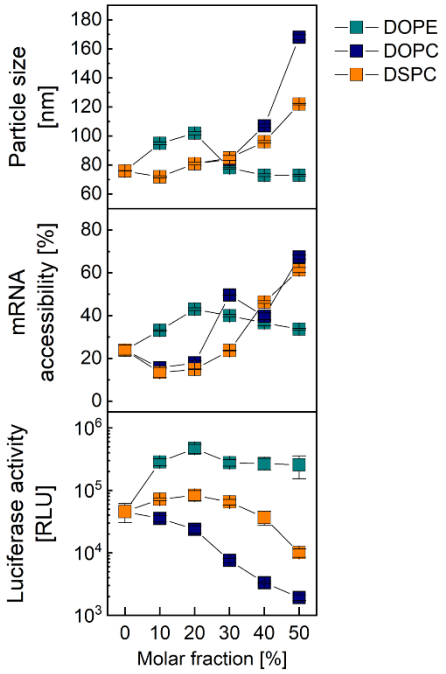

Figure 3.1-16 Analytical characteristics of LNP with various helper lipids.
LNP were prepared with distinct types of helper lipids: DOPE (Green), DOPC (yellow), and DSPC (blue) at varying molar fraction (0 – 58 %). Particle size measured by DLS is given in upper graph. mRNA accessibility measured by RiboGreen assay is given in the middle graph. Data are presented as mean ± SD, for n=1, for 2 technical replicates. Representative luciferase activity measured 24h after transfection with LNP in RAW 264.7 cells is given in the bottom graph. Data are presented as mean ± SD, for n=1 with three technical replicates.

To gain further understanding on internal structure, formulations containing DSPC, DOPC, and DOPE at varying mol % (0 to 50, top-down) were analyzed by SAXS (Figure 3.1-17). The scattering profiles display similar features to those previously described, with a single broad maximum at the momentum transfer of 1 nm^{-1} and a steep intensity decay as a function of q, where a region of linear slope in the q range inferior to the main peak can be observed. Remarkably, some scattering curves exhibited a further modulation of intensity at higher q, with a maximum at about 1.39 nm^{-1}, which is more evident for higher fractions of DOPC and DSPC.

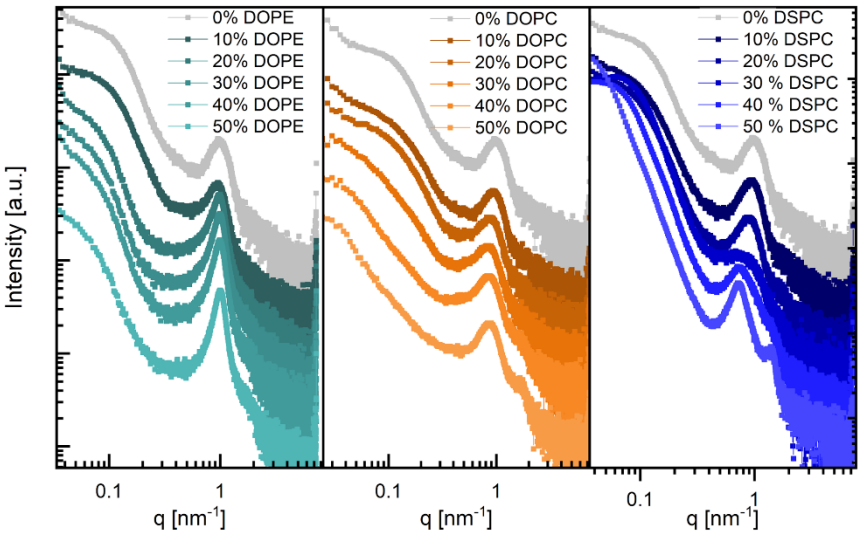

Figure 3.1-17 Representative scattering profile of LNP comprising different helper lipids obtained by Small-Angle X-rays scattering (SAXS).
LNP were formulated with DODMA, Chol, helper lipids (DOPC, DSPC, DOPE), and PEG-CerC16 at a respective molar fraction of 40/50-x/x/2, where x represents the helper lipid mol %, at N/P ratio 4.

Further quantitative analyses on peak positions, peak width, and peak area are given in Figure 3.1-18. A shift of the peak position (top diagram) as a function of molar fraction of helper lipid, corresponding to an increase of the repeat distance, can be identified. Interestingly, for DOPE, the increase in the repeat distance was obtained by substituting the Chol by 10 % of DOPE and was abrogated with increasing fraction of DOPE in the system. In case of DOPC, an increase of repeat distance was obtained up to 30 % which was slightly reduced with further increased fraction. While a monotonously and steep increase in the repeat distance was obtained by increasing DSPC fraction. The peak width (middle diagram) decreased with an increasing fraction of helper lipids, with most pronounced effects for DOPE. Therefore, the correlation length increased with increasing molar fraction of helper lipids, mostly pronounced for DOPE than DOPC and DSPC.

The peak area (bottom diagram) increased with an increasing fraction of helper lipids, which indicates an increase in the number of repeat units per stack as well the material contributing to the diffraction pattern was again more evident for DOPE than DOPC and DSPC. In case of DSPC, an exception was found 30 % of DSPC, where an abrupt decrease in the peak area as well an increase in peak with was observed, followed by a relaxation to previous values with acquired with 40 mol %.

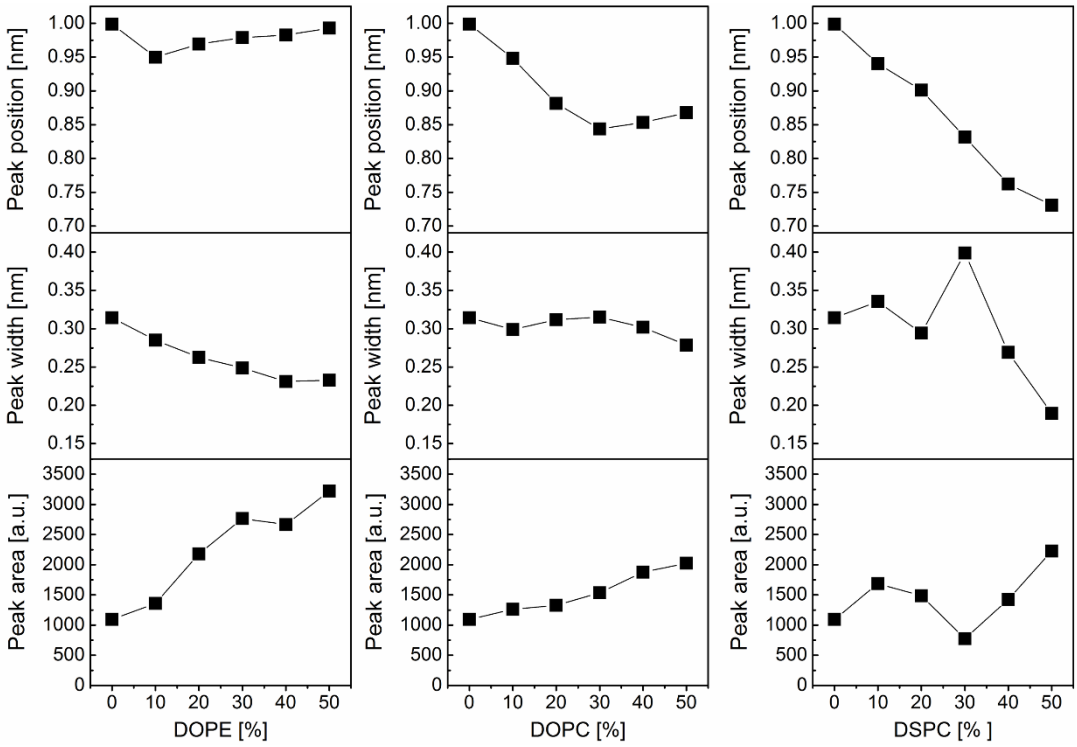

Figure 3.1-18 Quantitative analysis of peak properties of helper lipids.
Peak position, peak width, and peak area (top to bottom) as a function of the helper lipid DOPE (left column), DOPC (middle column) and DSPC (right column).

Altogether, the results points toward an insertion of the helper lipids by replacing cholesterol in the stacks leading to an increased level of organization which could be derived by the shift of the peak positions toward a lower q (larger spacing), in combination with increased number of repeat units per stack as well the material contributing to the diffraction pattern. The insertion of DOPE, cone-shaped lipid with saturated aliphatic chains, and therefore low T_m, is independently of the mol %. In opposite, DSPC with unsaturated aliphatic chains and high T_m leads to a membrane phase transition when it is present in the formulation above ~20-30 % mol. Moreover, it could be observed from previous data (Figure 3.1-16) that by increasing of mol % DSPC and DOPC, but not DOPE, lead to a progressive increase in mRNA accessibility, and thus lower encapsulation efficiency. Altogether, these data could indicate the presence of packing constraints within the lipid formulation, which were reduced when lipids with saturated aliphatic chains and more pronounced 'cone shape' like structures were present. Thereby, DOPE formulations exhibited improved particle characteristics and activity *in vitro*.

Based on efficacy data, DOPE as helper lipid was selected for further experiments. The effect of gradual incorporation of DOPE on LNP performance was further investigated *in vivo*. Data in Figure 3.1-19 shows the biodistribution of luciferase expression 6 h after IV and IM administration of LNP comprising 10, 20, 30, 40, 50 mol % of DOPE.

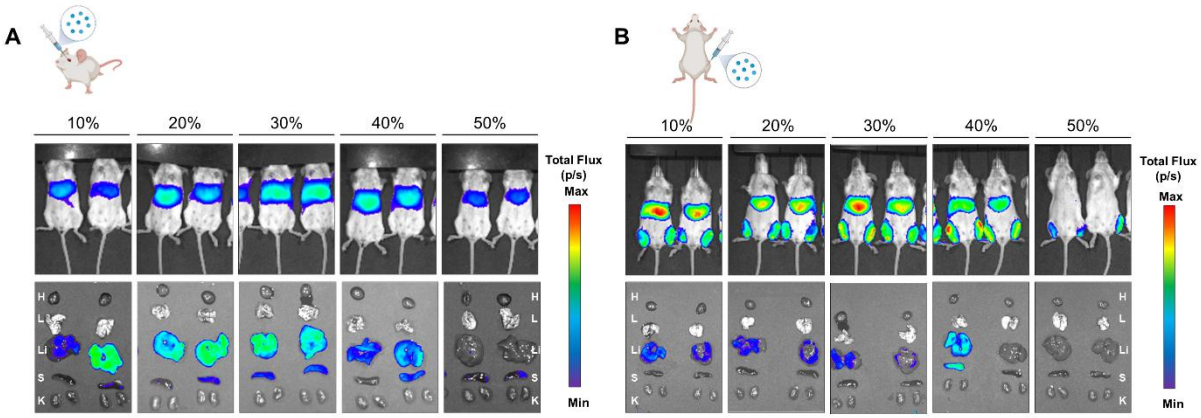

Figure 3.1-19 Firefly luciferase profile in Balb/C mice injected systemically and locally with mRNA-LNP.
Balb/C mice were injected with LNP formulated with increasing DOPE molar fraction Representative luciferase expression 6h after A) IV (via retro-orbital) and B) IM (tibialis posterior) application of 10 µg of mRNA. Organs represented as heart (H), lung (L), liver (Li), spleen (S) and kidneys (K).

Intravenous injection of DOPE-based LNP formulations targets mainly the liver and spleen, independently of DOPE mol % (Figure 3.1-19A). Notably, increasing DOPE up to ~30 % improved up to 3.5-fold the luciferase expression, while further DOPE mol % negatively impacted the luciferase expression. On the other hand, the intramuscular application resulted in luciferase activity not only in the injection muscle (tibialis posterior) but also in the liver and spleen (Figure 3.1-19B). Increased contents of DOPE (30-40 %) improved the signal in the injection area but also in the liver and spleen. Surprisingly, high contents of DOPE (40-50 mol %) abrogated the liver and spleen expression, and also the off-target effects. Nevertheless, the expression in the injection area reduced significantly, which could be a result of the high instability of the particles.

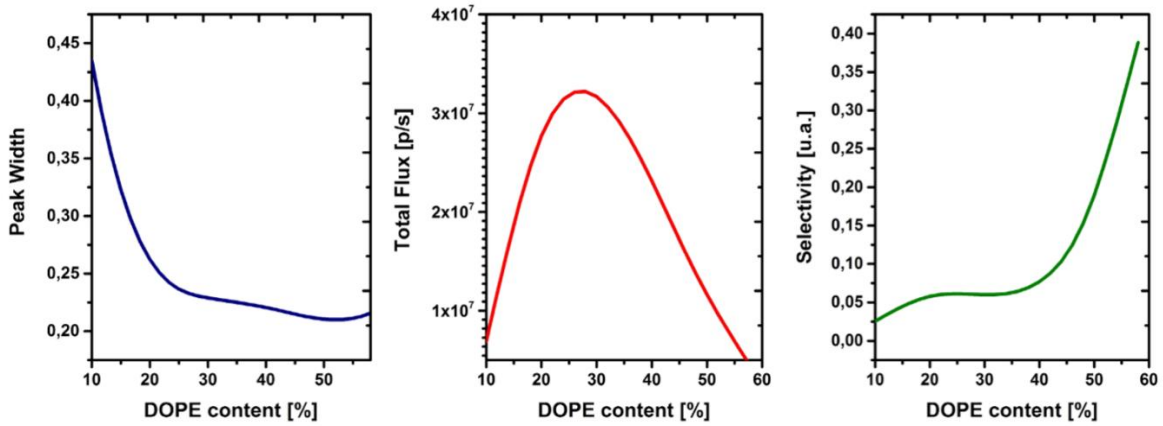

Figure 3.1-20 Representative scheme of the impact of DOPE mol % in the structure, expression and selectivity.

Figure 3.1-20 summarizes and illustrates the impact of the DOPE content in the structure, efficacy, and selectivity of the LNP. The progressive insertion of DOPE in the LNP leads to an abrupt decrease in the peak area, and thus an increase in the correlation of the lipid bilayers in the particle. On the other hand, the presence up to ~30 mol % of DOPE in the LNP benefits the overall expression, independently of the injection route. Finally, the selectivity is improved by the progressive content of DOPE, herein described for intramuscular purposes. Further fine-tuning of formulations (e.g., smaller

steps between 30 to 50 mol %) taking in account the choice of the ionizable lipid and other components must be carried out to design improved formulations for specific mRNA delivery to a given indication.

Overall, these results indicate that the helper lipids play a role in the structure, particle characteristics, biodistribution and efficacy. The phospholipid DOPE, with saturated aliphatic chains and a'cone shape' like structure, which adopts non-bilayer inverted hexagonal HII phase, improves the LNP properties and efficacy. Furthermore, LNP comprising ~ 30 % improves overall expression, whereas high mol % of DOPE (>40%) could be used to improve targeting selectivity towards the injection area. The identity and molar composition of the helper lipid can be used to improve the efficacy and selectivity of the LNP formulations for a given indication.

Grafted lipids for particle engineering

Polyethylene glycol is the most used stealth moiety in the pharmaceutical industry. Its principal role in LNP preparation is to reduce inter-particle interactions during particle nucleation to enable controlled manufacturing of particles with defined diameters in the range between 50 and 150 nm. However, the PEGylation of nanoparticles can also have substantial disadvantages concerning activity and safety, which is named the "PEG dilemma"[196,197].

Initial experiments focused on developing alternative strategies to formulate PEG-free lipid nanoparticles by rapid mixing protocol in one step. One of the first strategies used to prepare nucleic acid nanoparticulates (e.g., LPX) in the absence of PEG-grafted lipids was using the electrostatic repulsion principle. The principle states that opposite charges will result in attractive interactions, whereas equivalent charges will result in repulsive interactions. Thus, colloidally stable nanoparticulates can form in excess of net charge (positive or negative), whereas in the range of charge neutralization, particles display a polydisperse particle size and, often, aggregate[198].

In this thesis, formulations composed of ionizable lipid DODMA, Chol, and DOPE (45:35:20 mol %) at a total lipid concentration of 1.6 mM were mixed to a citrate solution containing mRNA (0.15 mg/ml), to reach an N/P of 0.5, using a Nanoassemblr® device. The resulting formulation, **mRNA-functionalized LNP**, exhibited a monodisperse particle size distribution of 118 nm, PdI of 0.2, and mRNA accessibility of 30%. In another approach, human serum albumin (HSA), which has an isoelectric point (pI) of ~ 7, and thus display a neutral to slightly positive net charge at the acidic pH (e.g., pH used for particle formulation), could be used to formulate LNP. For this purpose, lipid formulations composed of DODMA and DOPE (50:50 mol %) were mixed with a citrate solution (100 mM CB at pH 5.4) containing mRNA and HSA at 20 mg/mL, at N/P 3 by a microfluidic mixing (Spark® device). The resulting formulations, **protein-functionalized lipid nanoparticles**, or HSA-coated LNP**,** exhibited a particle size distribution around 200 nm, with PdI of 0.123, and a mRNA accessibility of 30%.

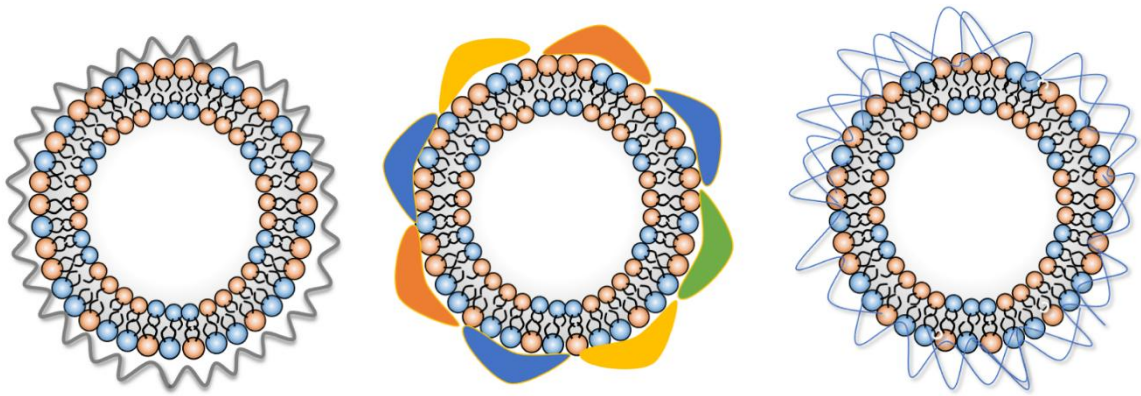

Figure 3.1-21 Strategies to formulate PEG-free lipid nanoparticles.
Lipid nanoparticles can be prepared by using an excess of mRNA (left), and proteins (center), or non-ionic surfactants (right).

Other molecules, non-ionic surfactants, might be used for particle preparation. Poloxamer, also known as Pluronic®, is composed of a block of poly(propylene oxide) (PPO), hydrophobic surrounding by two blocks of poly(ethylene oxide) (PEO, hydrophilic). For example, **poloxamer-functionalized LNP** formulations were formulated by mixing a lipid mixture of DODMA, Chol, DOPE, and Poloxamer P338 (45:44:10:1 and 45:43:10:2 mol %) with mRNA in 10 mM CB at pH 4 solution, at N/P 3, using the Nanoassemblr® device. The poloxamer-LNP displayed a particle size ranging from 150 to 200 nm, with a PdI around 0.2, and mRNA accessibility inferior to 30 %. Other Poloxamers, such as L61, P188, or P407, resulted in visible aggregation during LNP formation. In another instance, polypeptoids such as pSar has been explored as a substitute for PEG since it showed comparable stealth-like properties[144,148,199]. In this case, **Polysarcosine-functionalized LNP** formulations were formulated by mixing a lipid mixture of DODMA, Chol, DSPC, and $pSar_{34}$ (40:48:10:2 %) with an mRNA solution (100 mM CB at pH 5.4), at N/P 3, using the Nanoassemblr® device. The **Polysarcosine-functionalized LNP** displayed a particle size of ~ 100 nm, with a PdI around 0.2, and mRNA accessibility inferior to 30 %.

In summary, different technologies were conceptualized and developed in this section to manufacture PEG-free and ionizable-based LNP to design improved and safer lipid vehicles. Preliminary studies with pSar-grafted lipids showed that pSar-grafting enabled robust particle engineering and it can be heavily modified (e.g., endgroups, number of sarcosines units, and targeting moieties). In the next section, pSar-grafted lipids as a tool for engineering for RNA delivery will be further explored.

Polysarcosinylated Lipid as a Tool for Particle Engineering

Initial experiments focused on investigating pSar lipid for engineering mRNA nanoparticles using LNP rapid mixing protocol (described in Section 2.3.2). pSarcosinylated lipids with different pSar chain lengths (average of 11 to 65 sarcosine repeats units) and at different molar fractions (0-10%) were used for LNP manufacturing. In addition to pSar lipids, the cationic ionizable lipid DODMA, the helper lipid DSPC, and Chol at respective molar fractions 40/10/(50-x) were used, where x is the fraction of pSar lipid (Figure 3.1-22). Ethanolic solutions containing the lipid mixture were mixed to an aqueous phase containing modified mRNA, at N/P ratio of 4, using a microfluidic mixing device . For comparison, nanoparticles with the same lipid composition were assembled with PEG-DMG, a commercially available PEG lipid, instead of the pSar lipids.

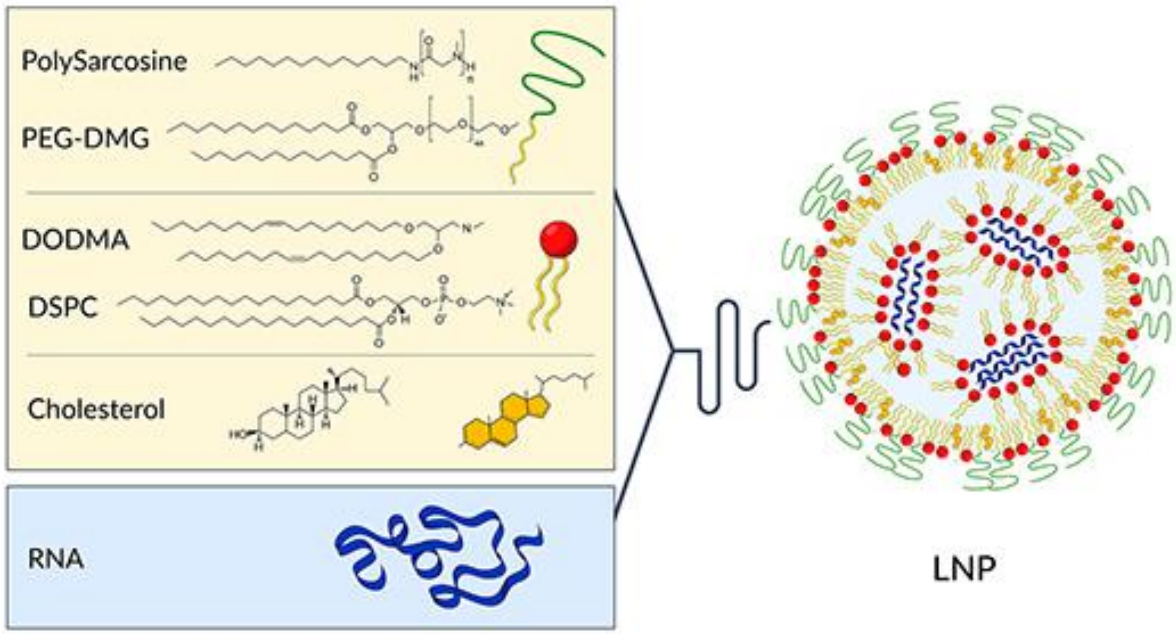

Figure 3.1-22 Lipids used for LNP manufacturing.
Lipid nanoparticles are generally composed of ionizable amino lipids, helper lipids, cholesterol, and a stealth moiety. The composition of the LNP was 40/10/50-x/x (DODMA/DSPC/cholesterol/grafted lipid, molar ratio), where x is the fraction of the grafted lipid. For pSar, n represents the number of sarcosine repeating unit. The cartoon at the right shows an artistic representation of the LNP: the RNA is thought to be present embedded in the excess lipid matrix, in the form of organized stacks of few repeat units, complexed with lipid membranes.

Lipid particles formulations containing no grafted lipid aggregated immediately post-production (data not shown). In contrast, however, the incorporation of pSar lipid enabled the formation of colloidally stable lipid nanoparticles, where the size depended on the chain length and the molar fraction of pSar lipids (Figure 3.1-23A). For all pSar chain lengths, the particle sizes decreased monotonously with the increased amounts of pSar lipid in LNP compositions, similar to PEGylated systems (Figure 3.1-23B). The particle size decreased also with increasing pSar length. In absolute numbers, the particles comprising pSar were larger than those obtained with PEG lipids at a similar molar fraction. For instance, LNP formed with 1.5 mol % $pSar_{34}$ (which has an equivalent molecular weight to PEG-DMG) exhibited a diameter of about 150 nm, while with PEG-DMG, it was 90 nm. All particles exhibited a PdI inferior to 0.25 and a close to neutral ζ-potential in physiological conditions (data not shown).

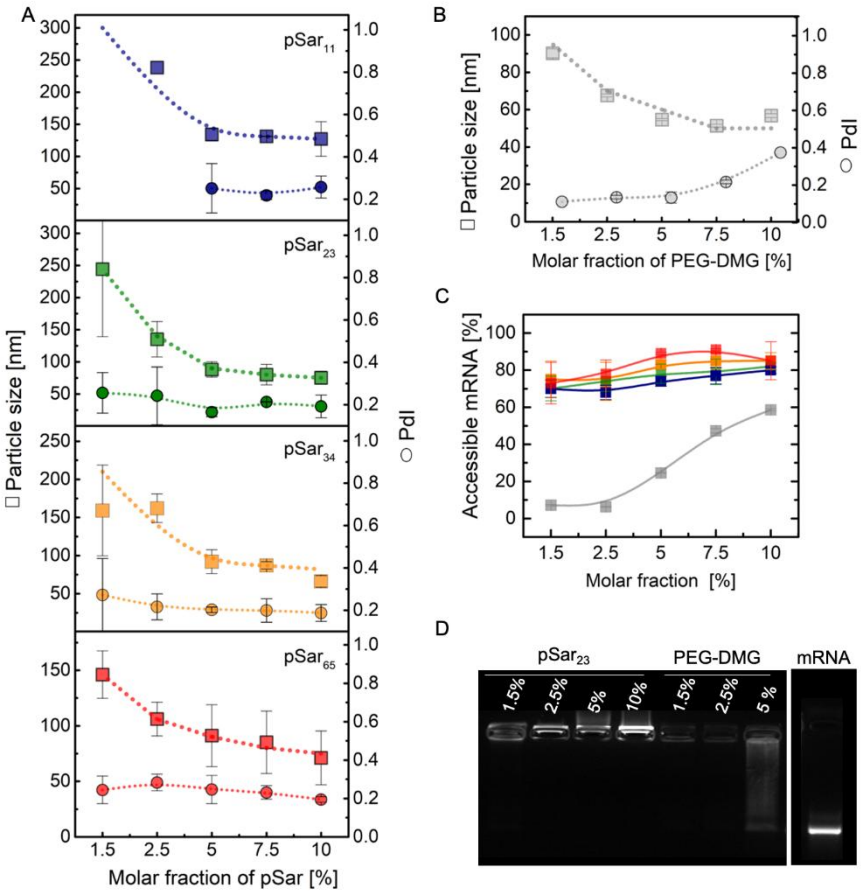

Figure 3.1-23 Effect of pSar lipid on LNP particle size compared to PEG lipid
(A) Size (hydrodynamic diameter, □) and polydispersity index (PdI, ○) as obtained from dynamic light scattering measurements of LNP as a function of molar fraction (1.5, 2.5, 5, 7.5, and 10%) of the pSar moieties with varying degrees of polymerization (blue squares, 11; green squares, 23; orange squares, 34; red squares, 65). Data are presented as mean ± standard deviation for n = 2−3. (B) Size and PdI of LNP as a function of molar fraction of PEG-DMG (gray squares, PEG-DMG). (C) Accessibility of the RNA to dye molecules using the Ribogreen kit. Systematically higher accessibility is measured for the pSar LNP than for those comprising PEG. (D) Determination of free RNA by the agarose gel assay. Both LNP with PEG and pSar show equally low values for free RNA. All LNP had the same basic composition, with the molar ratios DODMA/DOPE/cholesterol/grafted lipid 40/10/50-x/x. In all cases, the N/P ratio (DODMA to RNA) was 4. Data presented as mean ± standard deviation, n = 1.

Further differences between the PEG and the pSar LNP could be observed for the accessibility of the particle-bound RNA to Ribogreen assay (Figure 3.1-23C). Although, for the particles formed at this N/P ratio and with this lipid composition, in general, no substantial amounts of free RNA were determined, here exemplary demonstrated by agarose gel measurements for a pSar and a PEG system, (Figure 3.1-23D) the RNA in the pSar particles showed a systematically higher accessibility to the dye than that in the particles formed with PEG.

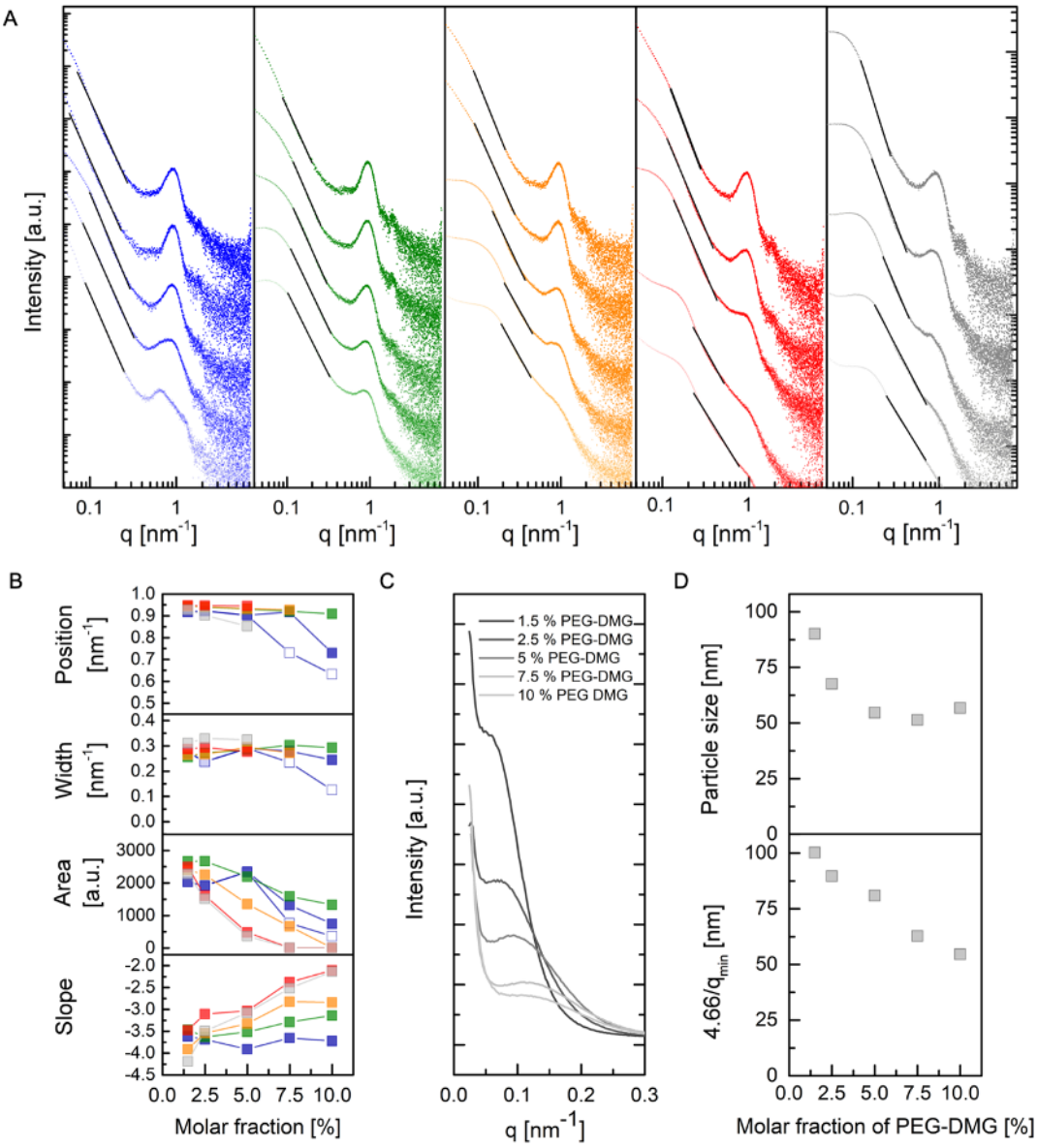

Figure 3.1-24 Small angle X-ray scattering (SAXS) data from pSar and PEG formulations.
A) pSarx LNP, from left to right $pSar_{11}$ (blue), $pSar_{23}$ (green), $pSar_{34}$ (orange), $pSar_{65}$ (red), and PEG-DMG (grey). For clarity the data sets are multiplied by constant factors. The fraction of grafted lipid increases from top to bottom (1.5, 2.5, 5, 7.5 and 10%). Slopes according to Porod power law were fitted the q range between 0.02 and 0.6 nm-1 and are drawn as solid lines. B) Peak position, peak width, peak area and Porod slope as a function of the increased molar fraction of pSarx, and PEG-DMG. For pSar11 a peak splitting at higher molar fractions was considered (open and closed blue squares). C) Scattering curves from PEG-DMG formulations in the q range between 0 to 0.3 nm-1. D) Particle size from dynamic light scattering measurements (top) and reciprocal qmin value, obtained from the curves in C, as a function of the PEG-DMG molar fraction. For ideal solid spheres the maximum and minimum positions would allow direct calculation of the diameter, for example the first minimum should be at r*q = 4.66.

The internal organization of the pSarcosinylated and PEGylated LNP was investigated by SAXS measurements (Figure 3.1-24). The scattering profiles display similar features to those described previously in this section, in which a single broad maximum dominates the curves at the momentum transfer, q, of about 1 nm^{-1}. In all cases, the peaks became less pronounced with increasing fractions of grafted lipid. Interestingly, some curves display a further modulation of intensity at a very low q, with a maximum at about 0.01 nm^{-1}, which is most clearly visible for the data from the PEG systems (Figure

3.1-24C). Such a pattern could result from the overall particle form factor. With a model of a solid sphere, one would expect oscillations with the first minimum at q × R = 4.49. Estimating the minimum position before the maximum to q = 0.05−0.09 nm−1, one obtains R = 90−50 nm, which is roughly in the order of the DLS results (taking also into account that anisotropy and surface roughness of the particles lead to deviations from the solid sphere model) (Figure 3.1-24D).

Quantitative data analysis by using Lorentzian functions underlines these qualitative observations shown in Figure 3.1-24B (Supporting Information shown in Table S 4). A slight shift of peak positions as a function of the molar fraction of the grafted lipid, corresponding to an increase of the repeat distance, is discernible. This could be due to partial insertion of the bulky stealthy lipids into the ordered stacks. The peak width increased slightly, and therefore the correlation length slightly decreased. As was already visible by the eye, the peak area decreased with increasing fraction and chain length of the grafted lipid, with most pronounced effects observed for the PEG-DMG data. Data sets from samples where no more peaks are discernible are indicative of the absence of ordered structures. Accordingly, calculation of the correlation length from the peak widths using a model for liquid crystals results in correlation lengths in the same order of magnitude as the repeat distance itself. This conjecture is further underlined by comparison of the experimental data with simulations using very basic assumptions for form factor and structure factor (*Figure S 7*). The scattering curves can be fairly well represented by organizing only two to three repeat units at the distances indicated by the peak position.

The Porod exponents decreased with increasing fractions of grafted lipid, and therefore, the surface and/or the mass fractal dimension increased. As previously described, higher surface roughness, changes in packing, or higher anisotropy could account for such change in slope.

Transfection of pSar In Vitro

To investigate the pSar LNP potency, mRNA expression was evaluated *in vitro* using HepG2 cell line. For this purpose, LNP comprising luciferase-encoding mRNA were assembled using either pSar or PEG lipids. Figure 3.1-25 shows the luciferase expression 24 h post-incubation with LNP manufactured with pSar lipids of different chain lengths or with the PEGylated lipid as a function of their molar fraction. In absolute numbers, the luciferase expression with the pSar systems was lower than with PEGylated systems; however, remarkably, for the pSar LNP, the luciferase expression increased with increasing pSar lipid content, as can be most clearly seen for the $pSar_{23}$ formulations (Figure 3.1-25A). In contrast, the activity of PEGylated systems decreased with increased PEG lipid fraction (Figure 3.1-25B). The reduction of luciferase expression with increasing PEG fractions is in accordance with the literature, where here the increased stealthy effect of PEG has been correlated with reduced cellular uptake and processing[196].

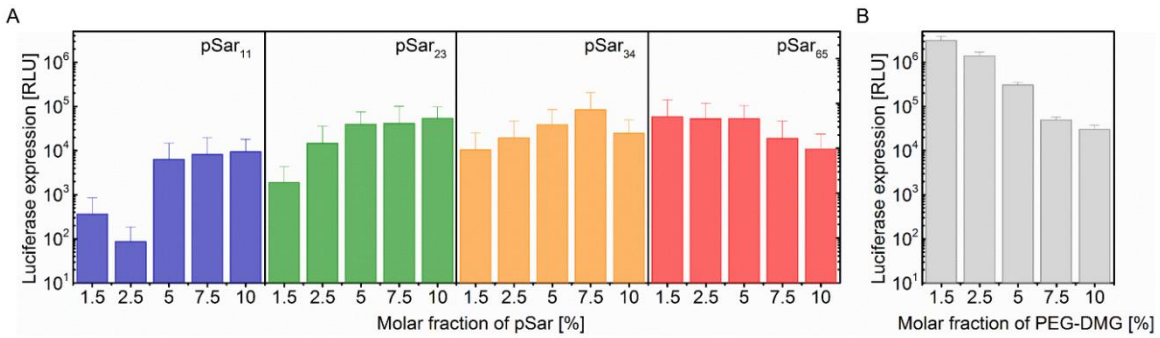

Figure 3.1-25 In vitro expression profile of pSar$_x$ and PEG LNP in a human hepatocyte cell line. Firefly luciferase expression 24h post-incubation with 250 ng/ml of mRNA-loaded LNP comprising increased molar fractions of A) pSar$_x$ and B) PEG-DMG. Data are represented as mean ± standard deviation, n=3.

The results illustrated the novel opportunities using pSar technology for the combination of particle engineering and optimization of biological activity, since the LNP activity increased with an increasing molar fraction.

Performance of pSar In Vivo

To investigate the ability of pSar LNP to safely and efficiently deliver the mRNA in vivo, Balb/C mice were intravenously injected with 10 µg of luciferase-encoding mRNA formulated into pSar LNP. The whole animal and extracted organs were analyzed for bioluminescence. In the primary experiments, the fraction of pSar lipid in the LNP was kept constant at 5 mol % whilst the chain length of pSar was varied from 11 to 65 units. As shown in Figure 3.1-26A, 6 h post-injection, all pSar LNP mediated high mRNA expression in the liver and spleen. Differences in the targeting selectivity and efficacy for the different pSar chain lengths were observed. While with pSar$_{11}$ the luciferase signal from the spleen was the highest, the signal decreased monotonously with increasing the chain length, and the targeting selectivity shifted toward the liver (Figure 3.1-26 B). It is important to note that the modulation of the spleen signal could have been impacted by the particle size, since large particles are known to target more efficiently toward the spleen[198]. As reported above, the particle size decreased with increasing pSar chain length (Figure 3.1-23), with the pSar$_{11}$ LNP being substantially larger than those with a higher chain length. For liver expression, here no such strong modulation was observed, although small particles are considered to be preferential for liver targeting[126].

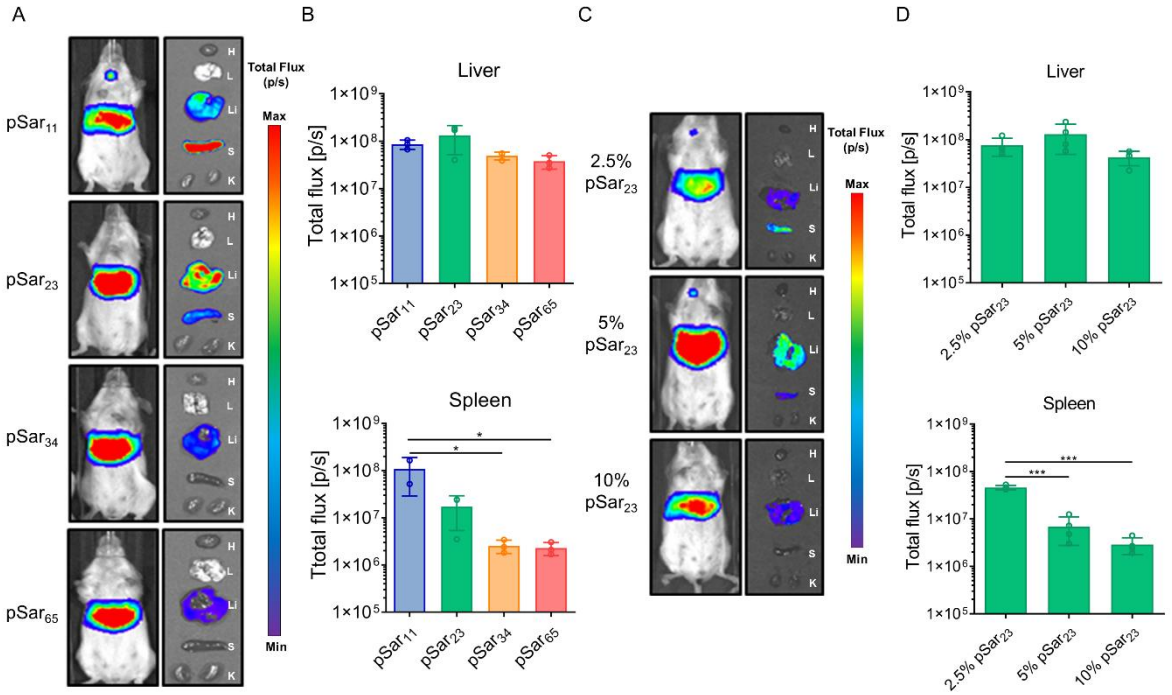

Figure 3.1-26 Firefly luciferase expression in Balb/C mice injected intravenously with pSar-LNP. Transfection at 6 h post-injection of LNP with an mRNA dose of 10 µg. (A) Representative bioluminescence of whole mice and extracted organs (*heart (H), lung (L), liver (Li), spleen (S) and kidneys (K)*) and (B) graphical display of ex vivo luciferase expression in the liver and spleen upon injection with LNP comprising 5% pSar lipid with increasing chain length (11−65 sarcosine units). Data are presented as the mean of total flux (photons/second (p/s)) ± standard deviation for n = 3. (C) Representative bioluminescence of whole mice and extracted organs (heart, lung, liver, spleen, and kidneys from top to bottom) and (D) graphical display of ex vivo luciferase expression in the liver and spleen upon injection with $pSar_{23}$ LNP comprising increased molar fraction (2.5−10%). Data are presented as the mean of total flux (p/s) ± standard deviation, n = 4. Statistical significance was calculated with one-way ANOVA with multiple comparisons (*p < 0.05; **p < 0.01; ***p < 0.001).

Based on efficacy, the $pSar_{23}$ was selected for further investigation, where the molar fraction of pSar lipid in the LNP was varied from 2.5 to 10 %. As previously shown for chain length, the molar fraction also has an impact on the biodistribution of the protein expression (Figure 3.1-26C,D). Formulations with 2.5 % $pSar_{23}$ resulted in an increased expression in the spleen, likely caused by a larger particle size (135 nm), whereas 10 % $pSar_{23}$ exhibited a specific expression toward the liver as a result of a small particle size (75 nm), reducing then off-target effects. Additionally, LNP comprising 5 % $pSar_{23}$ resulted in the highest expression in the liver (Figure 3.1-26D). While the transfection efficiency of optimized formulations reached the level of PEGylated LNP (Figure S 8), it appears important to investigate differences in safety and biomarker expression. To this aim, the potential systemic toxicity of pSar LNP was addressed through the analysis of global toxicity markers such as serum liver enzymes. The concentrations of ALT, AST, and LDH in the serum were determined 6 h after a single administration of LNP (n=3/group). Figure S 9 and Figure S 10 show that only $pSar_{11}$ and lower molar fractions induced a significant release of liver enzymes above the reference levels obtained for healthy mice, possibly associated with low density of pSar lipid. Furthermore, $pSar_{23}$ LNP and PEG-DMG induced similar levels of complement C3a at theoretical plasma concentrations *in vitro (*Figure S 11). However, at higher doses

(5X), pSar-based LNP resulted in substantially lower complement activation when compared to PEG-DMG LNP.

Altogether, the data confirm that pSar lipids might allow the assembly of potent lipid nanoparticles for intravenous mRNA delivery with an improved safety profile. The particles can be engineered toward optimized targeting selectivity and activity in the liver and, potentially, other organs (e.g., spleen). Besides, pSarcosinylated nanocarriers seem to be less immunogenic than PEGylated systems of comparable composition. In summary, pSar formulations are promising for RNA delivery in settings where immunogenicity needs to be avoided or precisely controlled by the mRNA itself.

3.2 Development of Improved pSar LNP for Hepatic Delivery

3.2.1. Screening of Ionizable Lipids to Improve pSar Technology

To further improve the overall therapeutic efficacy pSar LNP technology, several novel ionizable lipids previously tested in section 3.1.3 were formulated using pSar technology. In this section, LNP were formulated with ionizable lipid, helper lipid DSPC, Chol, and $pSar_{23}$, at 40/10/45/5 mol % respective molar fractions. The summary of LNP formulations characteristics and biological potency is displayed in Figure 3.2-1 and Table S 6.

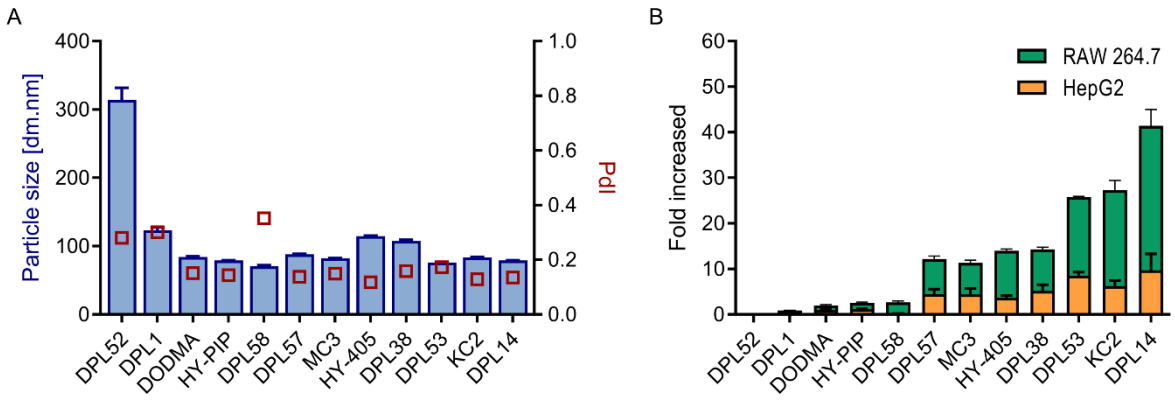

Figure 3.2-1 Optimization of ionizable lipid within pSar lipid nanoparticles.
A) Particle size and PdI of pSar LNP comprising different ionizable lipids measured by DLS. B) Protein expression of ionizable lipids in RAW 267.4 and HepG2 cell line. Data are presented as fold increase of the protein expression normalized against DODMA lipid, mean ± SD, for n=1 with three technical replicates.

The majority of resulting LNP formulations exhibited a particle size around ~ 100 nm, with a PdI inferior to 0.3 (Figure 3.2-1A). Despite the high mRNA accessibility (Table S 6), no free mRNA was detected by agarose gel electrophoresis (data not shown). In Figure 3.2-1B is depicted the fold increase in protein expression 24 h post incubation with LNP at 50 ng/well in RAW267.4 and HepG2 cell line, respectively. The ionizable lipid DODMA was used as control. The majority of ionizable lipids improved the protein expression over the control DODMA, used previously to optimize the pSar LNP formulations. The ionizable lipid DPL14 improved the potency of pSar LNP in both hepatocytes and macrophages cell lines, similarly to the previous results described in section 3.1.3.

Based on the efficacy, the DPL14 ionizable lipid was selected for further investigations, where the biodistribution of DPL14 ionizable lipid formulated LNP was investigated after IV administration. DODMA and the United States of Food and Drug Administration (FDA)-approved MC3 lipid were used

as control. The LNP from the novel lipids have been demonstrated to be stable and appropriate in all aspects for intravenous application of the mRNA (Table S 7). The *in vivo* expression profile of the pSar-LNP is shown in Figure 3.2-2. For all ionizable lipids the luciferase expression was highest in the liver and spleen. Here, the luciferase signals from pSar LNP comprising either DPL14 or Dlin-MC3-DMA were significantly higher than those with DODMA. LNP with DPL14 mediated the highest signal, with up to 100-fold increase in liver expression when compared to DODMA, and up to 2- to 4-fold higher compared to DLin-MC3- DMA.

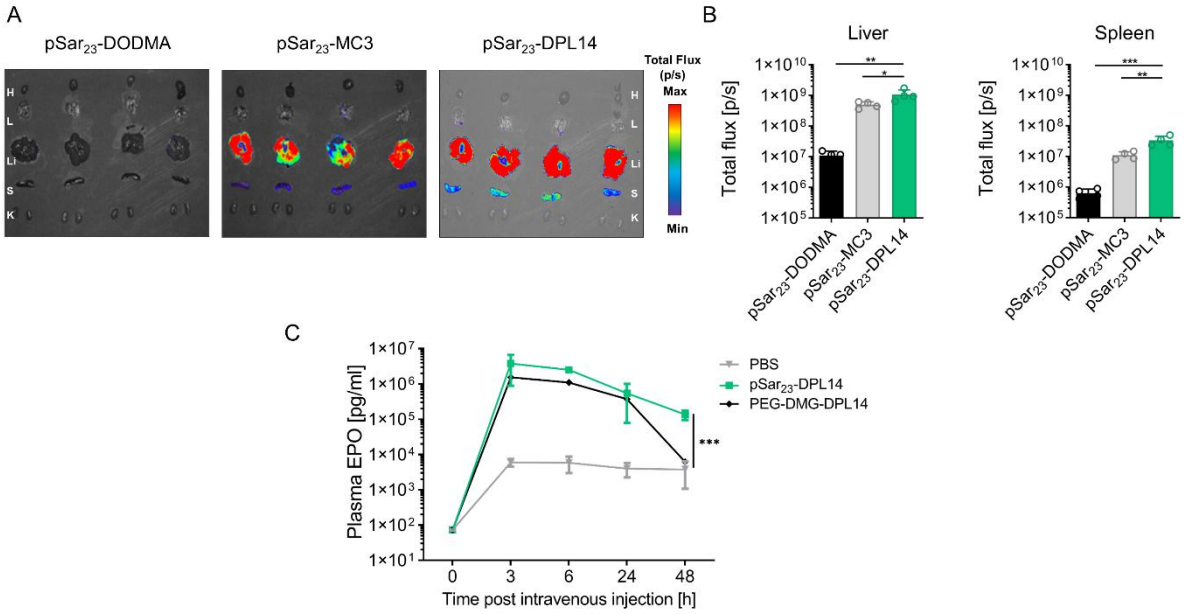

Figure 3.2-2 pSar LNP potency with different ionizable lipids.
A) Representative bioluminescence images of extracted organs (heart (H), lung (L), liver (Li), spleen (S) and kidneys (K)) at 6h post-injection of pSar-LNP comprising the ionizable lipids DODMA, DLin-MC3-DMA, and DPL14 with 2 µg of luciferase mRNA each for n=4/group; B) Luciferase expression in liver and spleen. Data are presented as the mean of total flux (p/s) ± standard deviation for n=4. Statistical significance was calculated with two-way ANOVA with multiple comparisons (* p< 0.05; ** p<0.01; *** p<0.001). C) Expression profile of EPO plasma concentrations after intravenous injection of 3 µg of EPO mRNA-loaded into DPL14-based LNP comprising 5% $pSar_{23}$ or 1.5% PEG-DMG, mean ± standard deviation for n=5. Statistical significance was calculated with two-way ANOVA with multiple comparisons (* p< 0.05; ** p<0.01; *** p<0.001.

For the ionizable lipid with the highest signals, DPL14 lipid, the activity of LNP with $pSar_{23}$ and PEG-DMG were directly compared. Table S 8 summarizes the physicochemical characteristic of both systems. The resulting LNP exhibited very similar sizes (90 nm), however $pSar_{23}$ displayed higher mRNA accessibility than PEG-DMG. As previously observed for DODMA, pSarcosinylated and PEGylated LNP containing DPL14 promoted comparable luciferase expression *in vivo* (Figure S 12). To further analyze the potency of pSar LNP, mRNA encoding the secreted protein EPO was formulated and intravenously injected. Remarkably, $pSar_{23}$ LNP showed higher and prolonged EPO secretion compared to PEG-DMG LNP (Figure 3.2-3), although, the performance of luciferase expression from PEG-DMG and $pSar_{23}$ LNP was similar. The higher durability of the EPO secretion for the pSar LNP may be related to differences in cellular uptake and processing of these two LNP types.

To gain further understanding, functional *in vivo* cell distribution experiments were performed after IV administration (Figure 3.2-3). As described previously, LNP formulated with DPL14 ionizable lipid were complexed with luciferase encoding miRNA target sites, which specifically silences the

luciferase expression in determined types of cells (miR-650-control, miR-122-hepatocytes and miR-42-3p-hematopoietic cells).

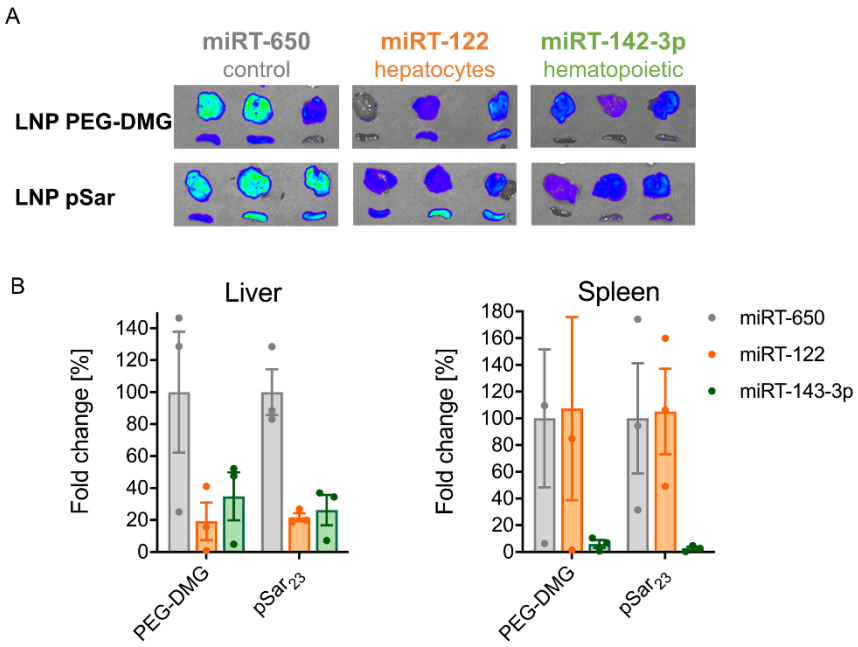

Figure 3.2-3 In vivo cell distribution of LNP formulated with pSar$_{23}$ and PEG-DMG.
LNP comprising pSar$_{23}$ (5%) or PEG-DMG (1.5%) were formulated with luciferase mRNA containing miR122, miR145-3p and miR650 target binding sites. Balb/C mice were injected with 2 µg of mRNA-LNP, and luciferase expression was measured in extracted organs after 24 h. A) Representative bioluminescense images of liver and spleen after 24 h. B) Fold change in luciferase expression to miR650 mRNA (control miR). Data are presented as mean ± SD, n=3.

The inclusion of miR-122 reduced the expression in the liver, whereas the expression of liver and spleen was abrogated by inclusion of miR-142-3p for both LNP. Similarly, the effect of miR was equivalent for both pSar and PEG LNP in the liver and spleen, suggesting similar *in vivo* cell distribution. Interestingly, pSar-LNP showed to interact more efficiently with cell membranes than PEGylated LNP, particularly with hepatocytes when measured by flow cytometer (Figure S 13).

In summary, several ionizable lipids were screened using the pSar technology platform. Ionizable lipid DPL14 showed great effectiveness in delivery of mRNA to the liver, validating previous results. This potent lipid, in combination with pSar LNP, mediated prolonged EPO expression when compared to PEGylated LNP, which seemed to be not a result of different cellular biodistribution *in vivo*.

3.2.2.Safety Profile of Improved pSarcosinylated LNP

Toxicity and immunostimulation can be a limiting factor for clinical translation of LNP comprising novel components[138,172]. To approach anti-drug antibody (ADAs) production and toxic effects, dose titration of EPO mRNA formulated in the pSar and PEGylated LNP in delivery vehicles were administrated via intravenous injection to Balb/C mice (n = 5/group) once weekly for four weeks followed by blood withdraw after 3, 6, 24 and 48h after injection. The body weight did not alter upon multiple injections (data not shown). Data in Figure 3.2-4 shows the protein secretion over 48 h after upon each weekly single intravenous injection over four weeks for a high (30 µg) and moderate (3 µg) dose of EPO mRNA. The overall protein expression decreased upon injection of each mRNA-LNP, in a similar trend for both pSar and PEG-DMG, which may be an indication of anti-drug antibody formation against both

LNP formulations. The liver enzyme profile (e.g., AST, ALT, LDH, and total Bilirubin) revealed that the IV administration of LNP induced an increase in the release of liver enzymes compared to the vehicle buffer. Notably, pSar-based LNP induced similar or lower levels of enzymes when compared with PEG-LNP counterpart.

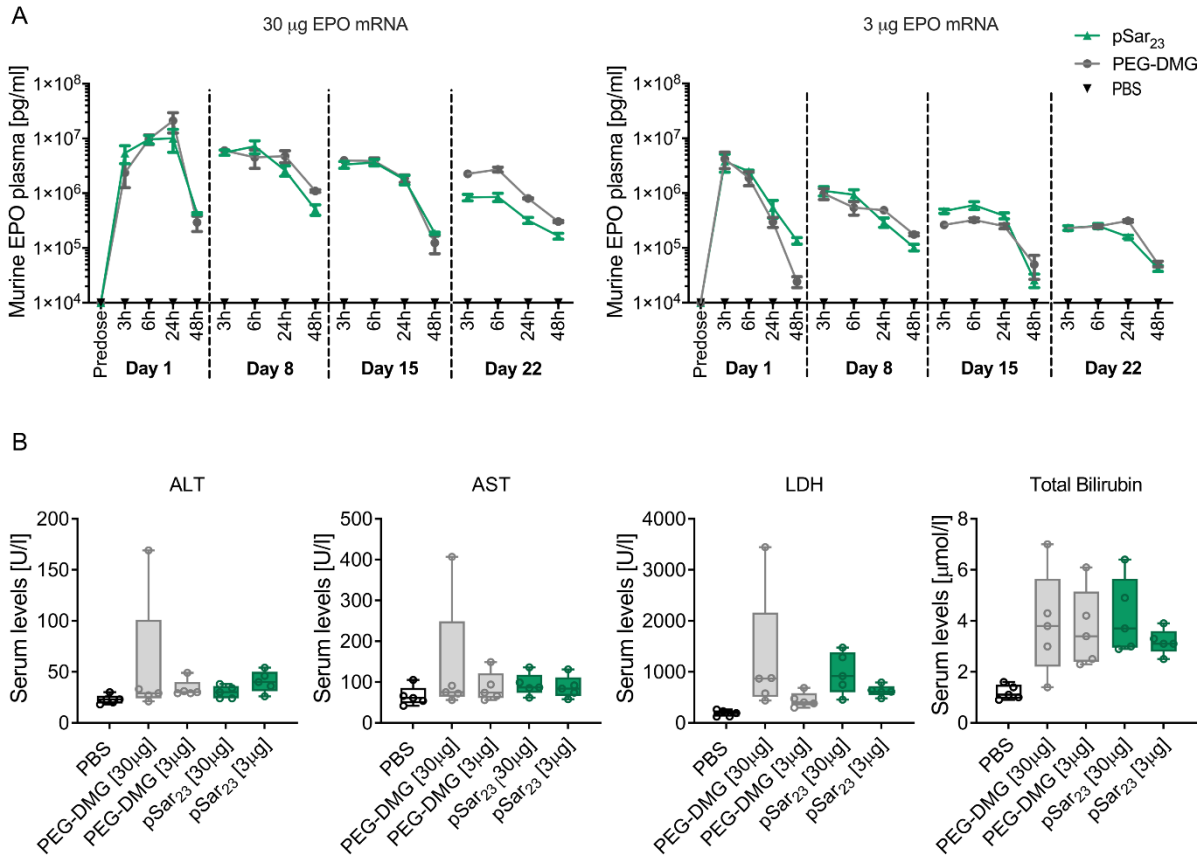

Figure 3.2-4 Safety profile of pSar LNP upon multiple intravenous injections.
Balb/C mice were weekly injected (total of 4 injections) with LNP-formulated with EPO encoding mRNA at 30 and 3 μg. A) Expression profile and B) Liver enzyme release profile up on multiple, mean ± standard deviation for n=5.

Finally, the capabilities of pSarcosinylated LNP to activate the innate immune system were further examined in an *in vitro* human model. Whole blood from three healthy human donors was treated with mRNA formulated LNP, including the positive controls LPS (Lipopolysaccharides) and R-848 (Resiquimod).

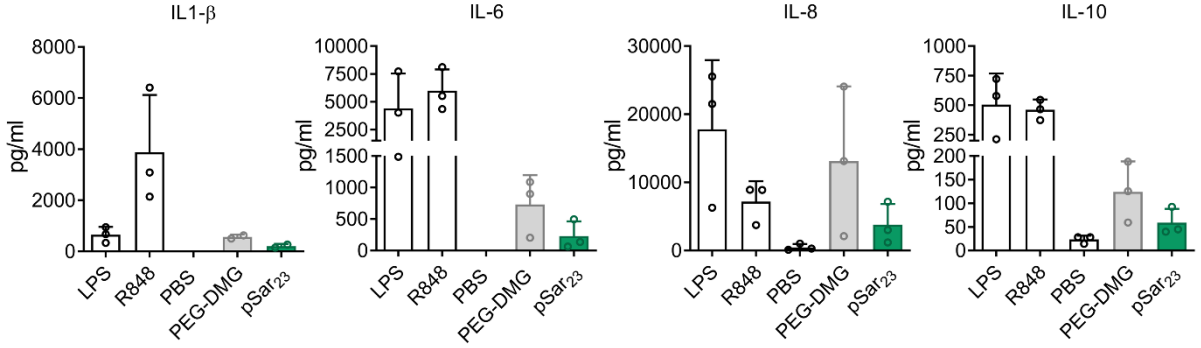

Figure 3.2-5 Human plasma cytokine profile in whole blood.

Cytokines were analysed using blood from three donors. The shown analytes include IL-6, IL-8, IL-1B, IL-10, the other cytokines showed either overall low expression or minor changes upon treatment were IL-4, IL-5, IL-2, GM-CSF, IFN-γ, TNF-α (data not shown). Data are shown as mean ± standard deviation.

Plasma was collected after 24 h and analysed using Cytokine 10-Plex Human Panel. Analytes included IL-8, IL-6, IL1-B, INF-γ, TNF-α, IL-2, IL-10, IL-4, IL-5, GM-CSF. A selection of four analytes (IL-6, IL-8, IL-1B, IL-10) is shown in Figure 3.2-5. The other analyzed cytokines showed either overall low expression or only minor changes upon treatment (data not shown). LNP formulated with $pSar_{23}$ showed a reduced cytokine induction when compared with those prepared with PEG-DMG.

Polysarcosine-functionalized LNP, in combination with novel ionizable lipids, showed improved potency and tolerability. It is important to note that pSar LNP showed prolonged EPO secretion compared to PEG-DMG LNP, despite the distribution of luciferase expression from PEG-DMG and $pSar_{23}$ LNP was similar. The higher durability of the EPO secretion for the pSar LNP at the lower doses may be related to differences processing of these two LNP types, where the lower toxicity of the pSar systems compared to PEG systems may be of significance. These results are line with previous reported data on the low immunogenicity of polysarcosine in zebrafish embryos and mice[200], rabbits, and rats[201]. Nevertheless, a decrease in expression of EPO for both pSar and PEGylated LNP after multiple injections in mice was observed, suggesting accelerated clearance of both systems. Such phenomenon has been described previously by Sebin and colleagues in PEGylated LNP in mice[202]. The authors argued that PC lipids in the formulation firstly drive the induction of IgM which, upon repeated dosing, binds to the LNP leading to formation of anti-PEG Immunoglobulin M (IgM) and anti-PEG Immunoglobulin G (IgG) responses. It may be plausible to suggest that the reduced expression upon multiple injections of pSar and PEG LNP could be driven by other components on LNP formulations. Further studies, such as investigation of the tolerability in other animal models like rat or non-human primates, will be necessary to fully elucidate the applicability of the pSar LNP as RNA delivery systems with improved safety profile.

3.3 Development of LNP for saRNA Vaccines

3.3.1. Optimization of saRNA-loaded LNP by *In vitro* Evaluation

Emerging worldwide pandemics urged the development of fast and inexpensive vaccines. Self-amplifying RNA shows great potential towards that goal due to its self-amplifying properties, which allows for lower doses to be administered possible reducing secondary effects[176]. This section aimed to rationally design LNP formulations for intramuscular application of saRNA. A luciferase-encoding saRNA was used for the initial optimization of LNP for intramuscular delivery of saRNA. To establish a baseline from which to improve, saRNA was first formulated using the original formulation parameters, previously described for mRNA delivery. A liposomal formulation, prepared by ethanol injection, composed of DOTMA and DOPE (50:50), was mixed with a saRNA solution, resulting in particle aggregation in few hours (data not shown).

The optimization of LNP for saRNA was based on a rational approach by varying a low number of parameters each time. In total, three libraries (A, B, and C) were sequentially designed based on experimental results and summarized in Table 3.3-1.

Table 3.3-1 Summary of formulation library.

Parameter	**Original formulation**	**Library A**	**Library B**	**Library C**
Phospholipid	DOPE	DOPE	DOPE, DSPC, DOPC	DOPE
Cationic lipid	DOTMA	DOTMA, DODAP, DPL52 DPL38, DPL14, KC2, MC3, DODMA	DODMA	DODMA
Phospholipid molar fraction	33,7%	10%	10 %- 50%	10%
Cationic molar fraction	66,3%	40%	20 – 60%	40%
Chol molar fraction		48%	0-58%	40-50%
Stealth lipid		PEG-CerC16	PEG-CerC16, PEG-DSG PEG-DMG, $pSar_X$	PEG-DMG, $pSar_X$
Stealth lipid molar fraction		2%	2 %	1.5 to 10%
N/P ratio	4	4	1.5-6	4

For simplification, each LNP was named after the corresponding library letter: formulations A-1 to A-8 correspond to library A; formulations B-9 to B-27 correspond to library B; and formulations from C-28 to C-33 correspond to library C. The detailed composition and physicochemical characteristics ratio of LNP formulations are described in Table 3.3-2. Due to the high number of formulations herein tested, the initial optimization of LNP was based on luciferase expression in C2C12 cell line, relevant for intramuscular application (Figure 3.3-1).

The first library (A) was designed to improve the overall potency of saRNA-LNP by varying the cationic lipid identity. Seven different cationic lipids were assessed to optimize saRNA-LNP formulation (A-1 to A-8). DLin-MC3-DMA was included as a control. Formulation A-8 comprising ionizable cationic DODMA mediated the highest expression in C2C12 cell line. Notably, MC3 (A-7) did not lead to substantial transfection efficiency *in vitro.* From a physicochemical point of view, the LNP characteristics, such as particle size, were remarkably similar with a monodisperse size distribution between 80 to 120 nm. Regarding mRNA accessibility, formulation A-5 and A-7 showed relatively higher mRNA accessibility when compared to the other formulations (>20 %). In library A*,* four formulations (A-3, A-4, A-5, A-8) out of eight were selected for *in vivo* testing. Formulation A-8 was used as a basis to design library B since it resulted in higher transfection efficiency.

Table 3.3-2 Lipid composition and N/P ratio of LNP formulations in the A, B and C libraries.

LNP ID	%	IL	%	Chol	%	Phosp.	%	Grafted-lipid	N/P ratio	Size [nm]	PDI	mRNA Acces.[%]
A-1	40	DOTMA	48	Chol	10	DOPE	2	PEG-CerC16	4	73	0.195	3
A-2	40	DODAP	48	Chol	10	DOPE	2	PEG-CerC16	4	89	0.125	19
A-3	40	DPL52	48	Chol	10	DOPE	2	PEG-CerC16	4	69	0.213	2
A-4	40	DPL38	48	Chol	10	DOPE	2	PEG-CerC16	4	88	0.226	1
A-5	40	DPL14	48	Chol	10	DOPE	2	PEG-CerC16	4	88	0.211	29
A-6	40	KC2	48	Chol	10	DOPE	2	PEG-CerC16	4	84	0.189	10
A-7	40	MC3	48	Chol	10	DOPE	2	PEG-CerC16	4	122	0.153	22
A-8	40	DODMA	48	Chol	10	DOPE	2	PEG-CerC16	4	86	0.210	20
B-9	40	DODMA	48	Chol	10	DOPC	2	PEG-CerC16	4	86	0.203	19
B-10	40	DODMA	48	Chol	10	DSPC	2	PEG-CerC16	4	106	0.194	21
B-11	40	DODMA	28	Chol	30	DOPE	2	PEG-CerC16	4	84	0.178	19
B-12	40	DODMA	28	Chol	30	DOPC	2	PEG-CerC16	4	88	0.190	31
B-13	40	DODMA	28	Chol	30	DSPC	2	PEG-CerC16	4	117	0.180	38
B-14	40	DODMA	0	Chol	58	DOPE	2	PEG-CerC16	4	85	2.051	24
B-15	40	DODMA	48	Chol	10	DOPE	2	PEG-DMG	4	85	0.176	24
B-16	40	DODMA	48	Chol	10	DOPE	2	PEG-DSG	4	75	0.156	16
B-17	40	DODMA	48	Chol	10	DOPE	2	PEG-DSPE	4	82	0.182	16
B-18	40	DODMA	45	Chol	10	DOPE	5	$Psar_{23}$	4	129	0.153	36
B-19	40	DODMA	45	Chol	10	DOPE	5	$pSar_{11}$	4	125	0.244	47
B-20	40	DODMA	45	Chol	10	DOPE	5	$pSar_{34}$	4	105	0.239	106
B-21	40	DODMA	45	Chol	10	DOPE	5	$pSar_{65}$	4	105	0.205	93
B-22	20	DODMA	64.6	Chol	13.4	DOPE	2	PEG-CerC16	4	98	0.149	15
B-23	60	DODMA	31.4	Chol	6.6	DOPE	2	PEG-CerC16	4	115	0.213	50
B-24	40	DODMA	48	Chol	10	DOPE	2	PEG-CerC16	2	161	0.237	60
B-25	40	DODMA	48	Chol	10	DOPE	2	PEG-CerC16	3	96	0.189	29
B-26	40	DODMA	48	Chol	10	DOPE	2	PEG-CerC16	5	83	0.191	18
B-27	40	DODMA	48	Chol	10	DOPE	2	PEG-CerC16	6	82	0.192	19
C-28	40	DODMA	48.5	Chol	10	DOPE	1.5	$pSar_{23}$	4	169	0.496	5
C-29	40	DODMA	47.5	Chol	10	DOPE	2.5	$pSar_{23}$	4	139	0.253	12
C-30	40	DODMA	40	Chol	10	DOPE	10	$pSar_{23}$	4	90	-	97
C-31	40	DODMA	48.5	Chol	10	DOPE	1.5	PEG-DMG	4	109	0.175	9
C-32	40	DODMA	47.5	Chol	10	DOPE	2.5	PEG-DMG	4	88	0.215	23
C-33	40	DODMA	45	Chol	10	DOPE	5	PEG-DMG	4	71	0.192	47

Legend: Ionizable lipid (IL), Phospholipid (Phosp.), Cholesterol (Chol), mRNA accessibility (mRNA access.)

The second library, Library B, was designed with a large space design to evaluate the impact of the individual parameters, such as N/P ratio, molar composition, helper lipid identity on the biodistribution and potency of the LNP (B-10 to B-27). Increasing the N/P ratio up to 4 improved the transfection potency, whereas further excess of lipids did not alter the activity (B-24, B-25, A-8, B-26 and B-27 corresponding to NP 2, 3, 4 ,5 and 6). However, the particle size was reduced from ~160 to 80 nm, while the mRNA accessibility increased from ~ 60 to 19 %. Interestingly, the maximum protein expression was achieved with 40 % of ionizable lipid (B-22, 20 %; A-8, 40 %; B-23, 60 %). In that respect, these formulations displayed similar particles sizes ~ 100 nm, however increased mol % of ionizable cationic lipid led to an enhanced mRNA accessibility. Another interesting finding was that increased DOPE molar fraction reduced the protein expression when saRNA was delivered *in vitro* (with A-8, B-11, and B-14 corresponding to 10, 30 and 58 % of DOPE mol %). Nevertheless, it is important to highlight that the helper lipid identity influenced luciferase expression. For instance, the protein expression was reduced when DOPE (A-8) was substituted by DOPC (B-9). In this case, where all formulations showed similar characteristics. Notably, the stealth lipid had the highest impact on transfection efficiency. Substitution of PEG-cerC16 by pSar (B-18, B-19, B-20) and PEG-DMG (B-15) improved the protein expression, whereas the replacement by PEG-DSG (B-16) or PEG-DSPE (B-17) reduced the biological activity. It is worth noting that herein pSar was tested with increased chain length (in average 11 to 65 units), where only pSar with 65 units (B-20) led to a reduction in expression, as previously described for mRNA. Moreover, pSar LNP displayed large particle sizes and higher saRNA accessibilities compared to PEGylated formulations. Based these interesting findings, pSar formulations B-18, B-19, B-20, and B-21 were selected for further *in vivo* studies.

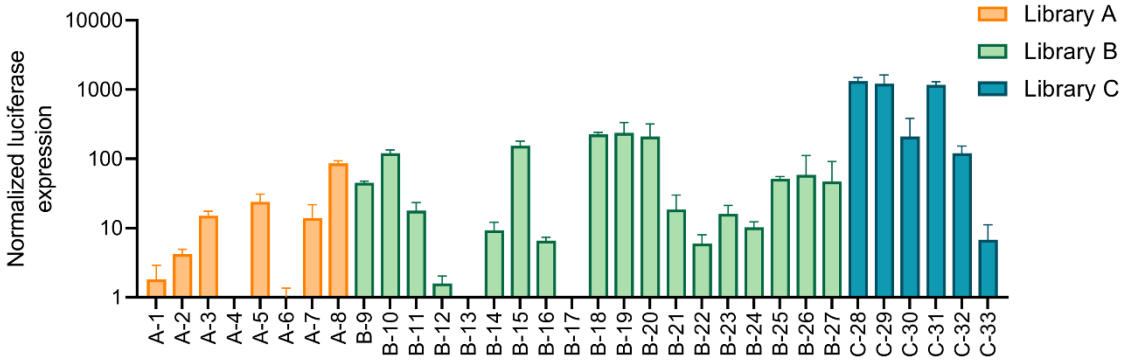

Figure 3.3-1 Normalized protein expression of saRNA-LNP from Library A, B and C.
Luciferase expression in murine myoblast (C2C12) cell line, 24 h post-transfection with 50 ng/ well of each formulation from Library A, B and C, normalized to an internal control.

In the Library C, we aimed to further investigate the impact of type and molar composition of $pSar_{23}$ and PEG-DMG on saRNA delivery (C-28 to C-33). In this case, $pSar_{23}$ (corresponding to 23 units) was selected based on previous data. With exception of C-33 formulations, all LNP evaluated in Library C outperformed formulation A-8, which comprises PEG-CerC16 as stealth lipid. Notably, pSar-LNP (C-28 to 30) mediated increased expression compared to PEG-DMG (C-31 to 33) counterpart. However, pSar-LNP displayed larger particle sizes compared to PEG-DMG formulations (e.g., 5% pSar and 5% PEG-DMG corresponding to 129 nm and 71 nm), whereas a higher mRNA accessibility was shown for

PEG-DMG in comparison to pSar formulations. Moreover, increased molar fraction of pSar LNP (C-28, C-29, B-18 and C30 corresponding to 1.5, 2.5, 5 and 10%) did not lead to a strong reduction *in vitro* expression compared to PEG-DMG formulations (C-31, B-, C32 and C-33 corresponding to 1.5, 2, 2.5, and %). In both cases, the reduction of expression was accompanied with a decrease in particle size and increase in mRNA accessibility. Due to the complexity of library C, all formulations were selected for further *in vivo* testing.

In summary, optimization of different parameters was used to develop a saRNA-based LNP for intramuscular application for vaccination purposes. These results indicated there is little to no correlations between particle characteristics, such as particle size or mRNA accessibility, and protein expression mediated by saRNA-LNP. Nevertheless, a great improvement *in vitro* was attained by optimizing cationic component, helper lipid, and grafting-moiety.

3.3.2.Evaluation of Optimized LNP for Intramuscular Delivery of saRNA in vivo

Fourteen out of the thirty-three formulations were selected for biodistribution of protein expression and immunogenicity studies upon intramuscularly injection in BALB/C mice (Figure 3.3-2**).** Further analysis was performed by quantifying the luciferase activity in the injection area for 14 days (AUC). In addition, splenocytes were collected 20 days post-IM injection and assayed for luciferase immunogenicity. Unexpectedly, formulation A-8 (from library A) promoted the highest protein expression in the injection area. None of the following optimizations in library B and C, mediated an improvement in protein expression in the muscle. However, two out (B-29 and C-32) of fourteen formulations improved the immunogenicity of the formulation, where the stealth lipid identity and the molar fraction were varied. No strict correlation was found between physicochemical parameters (e.g., particle size, mRNA accessibility, and surface charge) and immunogenicity *in vivo* (data not shown).

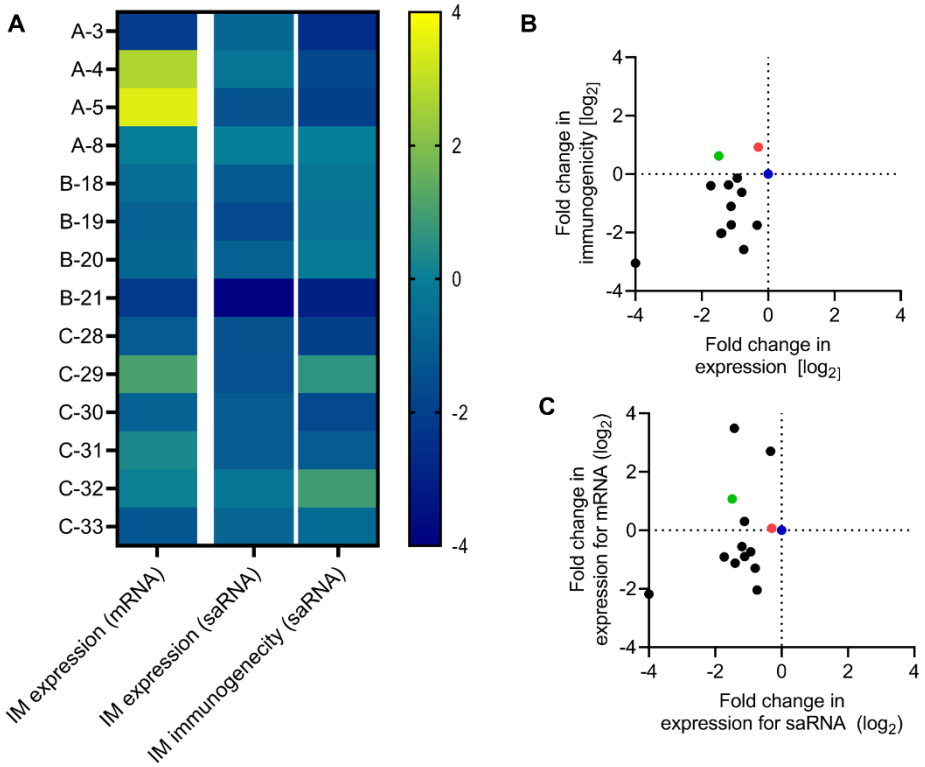

Figure 3.3-2 Expression and immunogenicity of LNP in mice.

Fourteen LNP formulations selected from previous *in vitro* studies were compared with benchmark (A-8) for expression and immunogenicity. Expression measured by luminescence in total flux (photon/sec) over 14 days after IM administration of 0.2 µg of saRNA-LNP and 2 µg of mRNA-LNP was expressed as area under curve (AUC). Mean ± standard deviation, for 3 mice per group. Data are represented as log2 fold change compared to A-8 formulation. (B) Log2 fold increase in expression was compared to the log2 fold change in immunogenicity for saRNA. C) Log2 fold in expression was compared for saRNA-LNP versus mRNA LNP formulations. The lead formulations are labeled accordingly: A-8 (blue), B-29 (green), and C-32 (red).

Next, it was investigated whether the result of formulation optimization would be similar or distinct for both saRNA and mRNA formats. There was no correspondence in rank between the LNP formulated with saRNA and with mRNA (Figure 3.3-2A). In LNP formulated with mRNA, four out of fourteen lipids improved the protein expression, caused by an exchange in ionizable lipid or stealth lipid identity (Figure S 14). The improved protein expression for the ionizable lipid was accompanied by an increased off-target effects. Notably, pSar-conjugated lipid mediated up to 2- fold increase in protein expression with reduced off-target effects; the most significant improvement made without exchanging the identity of the cationic lipid (Figure S 15). Notably, pSar LNP formulated with HA-encoding mRNA mediated slightly increased immune response when administrated intramuscularly (Figure S 16).

Overall, these results showed that protein expression does not strictly correlate with immunogenicity after IM application. Moreover, these data demonstrate that ideal formulations for mRNA might not be optimal for saRNA delivery showing the importance of screening and optimization of LNP for each payload and therapeutic application. Finally, it was shown that pSar LNP can efficiently deliver mRNA in an intramuscular setting.

3.3.3.Immunogenicity of saRNA-LNP encoding a model antigen

To further study their immunogenicity, the three best LNP formulations for saRNA (A-8, C-29, and C-32) were formulated with a H1N1-Hemagglutinin (HA)-encoding saRNA. The physicochemical characteristics are summarized in Table S 9. The formulation C-39 showed an increased particle size in comparison with A-8 and C-29 (~ 140 vs ~ 90 nm). Balb/C mice were injected with a single injection of 0.2 µg of saRNA-formulated LNP. The serum was collected after 14, 28, and 50 days after IM administration. Figure 3.3-3 shows the HA IgG titers and VNT over 50 days (AUC), and T cell responses after IM administration of the following saRNA-complexed formulations: A-8, C-29, and C-32. All formulations induced comparable protection, but only A-8 showed a significant increase in VNT titers compared to vehicle buffer. Regarding IgG responses, formulation A-8 induced higher IgG antibody titers compared to other formulations and buffer. Finally, a higher CD4+ T cells were induced by C-29 and C-32 formulations, whereas CD8+ T cells were significantly increased for A-8 formulation. Despite trending differences between the formulations, none of the groups were significantly different when assessed by ANOVA adjusted for multiple comparisons.

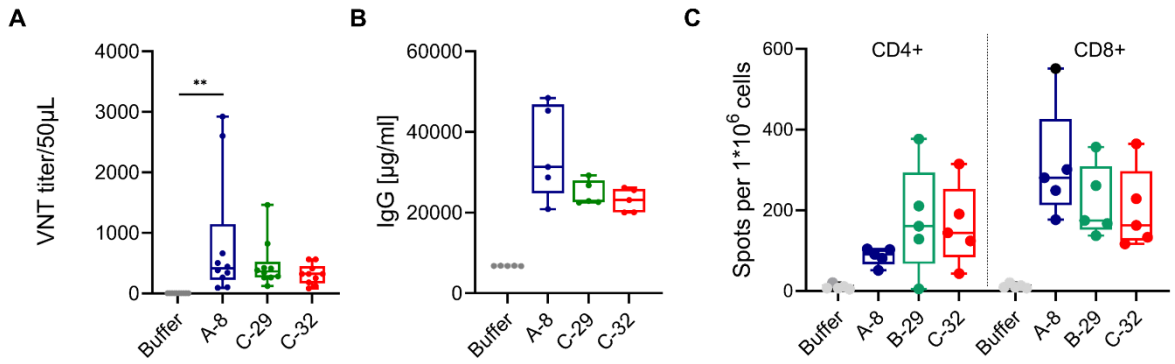

Figure 3.3-3 HA-specific immunogenicity of saRNA-LNP.
BALB/c mice were immunized IM with 0.2 µg of H1N1-HA coding saRNA or buffer solution only (PBS). H1N1-specific antibody was measured by ELISA (A) and VNT (B) 14-, 28- and 50-days weeks after IM LNP administration at 0.2 µg. Immunogenicity is represented as area under curve (AUC), with 5 mice per group. C) T cell response after 50 days post-immunization, with 5 mice per group. Statistical analysis was performed with ordinary one-way ANOVA with Dunnett's multiple comparisons test of LNP formulations vs buffer * - P <0.05, ** P<0.01, ***P<0.001, ****P<0.0001.

These data indicated that the immune responses depend on the lipid composition; the grafted-lipid moieties seem to have an impact on the immunogenicity. Further experiments would be required to fine tune those formulations for efficient saRNA delivery. Nevertheless, our results suggested that formulation A-8 might be a promising candidate for saRNA vaccination against infectious diseases.

3.3.4.Immunogenicity of LNP loaded with an EBOV-GP encoding saRNA

After optimizing the formulation immunogenicity with a model antigen, we investigated the potential of A-8 formulation in a therapeutic setting. To this end, Balb/C mice were injected with A-8 LNP formulated with saRNA encoding for Ebolavirus glycoprotein (EBOV-GP). A polyplex (PLX) formulation composed of polyethylenimine (PEI) was used as a formulation control. Mice received a single IM immunization with 0.2 µg of saRNA-LNP. EBOV-GP specific antibodies and VNT titters were quantified 14, 28, and 50 days after IM immunization. T cell responses (CD4+ and CD8+) were analysed 50 days after the IM immunization.

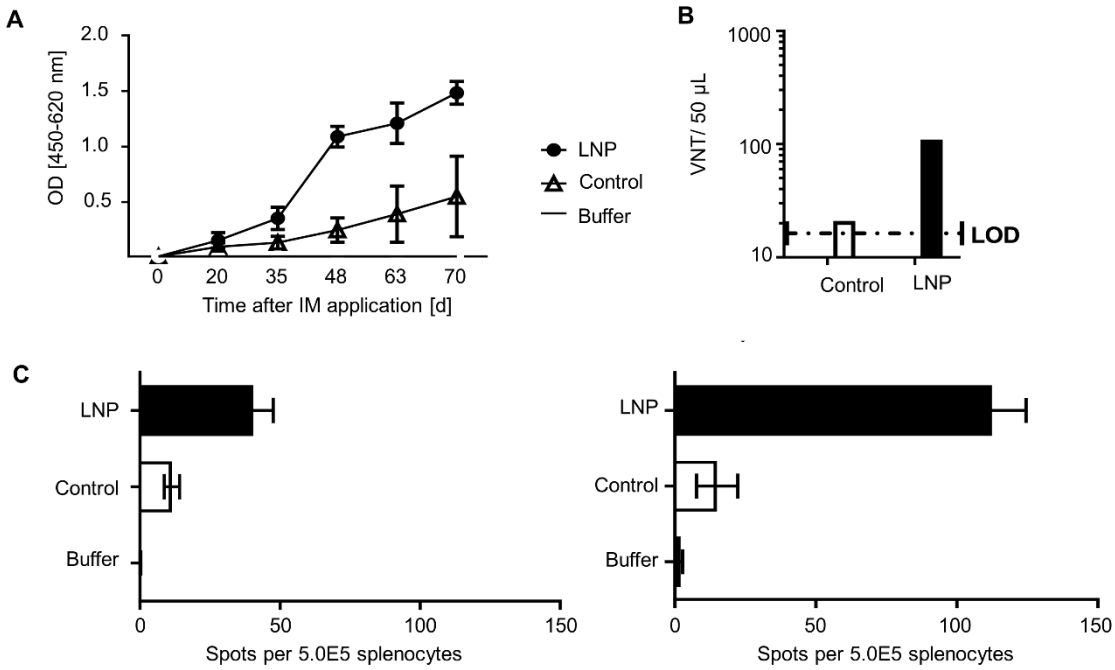

Figure 3.3-4 Immunogenicity of EBOV-GP saRNA-LNP.
BALB/c mice were immunized IM with 0.2 µg of EBOV-GP coding mRNA or buffer solution only (PBS). EBOV-GP antibody was measured by ELISA (A) and VNT (B) 20, 35, 48, 53 and 70 days after IM LNP administration at 0.2 µg. Immunogenicity is represented as area under curve (AUC), with 5 mice per group. C) T cell response after 70 days post-immunization, with 5 mice per group. Statistical analyzes was performed with ordinary one-way ANOVA with Dunnett's multiple comparisons test of LNP formulations vs buffer * - P <0.05, ** P<0.01, ***P<0.001, ****P<0.0001.

The LNP A-8 formulation induced increased IgG and VNT titers as well as T cell responses when compared to the buffer and control PEI formulation. These data indicated that formulation A-8 enabled both innate and adaptive specific response against EBOLA.

In summary, a wide range of parameters were investigated for the developed of improved saRNA vaccine formulations. We found little correlation between expression and immunogenicity, indicating that immunogenicity is required to identify improved saRNA vaccine formulations. Finally, optimized saRNA LNP elicited EBOV-GP specific antibody and neutralization titers, and T cell responses, suggesting this RNA-lipid formulation might be a promising candidate for vaccination against infectious diseases.

CHAPTER 4 | Discussion

In this thesis, fundamental aspects of lipid nanoparticle technologies for mRNA delivery were thoroughly investigated using a wide range of physicochemical and biological methods. Technical aspects of particle engineering and design, such as manufacturing technology, helper lipid selection, ionizable lipid characteristics, functionality of grafted lipids, particle engineering and targeting, were investigated and evaluated in order to develop the next generation of lipid nanoparticles for improved efficacy and tolerability.

4.1 mRNA-Lipid Nanoparticles Manufacture Procedure

Alternative Manufacturing Procedure Open Novel Opportunities in the mRNA Delivery

Regarding the manufacturing technology, it could be shown that the structure of the lipid-based systems depends more significantly on the lipid composition design than on the manufacturing procedure (Figure 3.1-7, Figure 3.1-17, Figure 3.1-24). Lipid nanoparticles comprising ionizable lipids have been initially designed for hepatic delivery. LNP are mostly composed of phospholipids, cholesterol, and PEG-grafted lipid, and often display particle sizes sub-100 nm[76,97]. Therefore, the structure of ionizable-based LNP formulations substantially differs from conventional cationic-lipoplex systems, which may comprise similar lipids, but where lipids in an aqueous phase (liposomes) instead of the ethanolic lipid solution are mixed with the RNA[203–208].

Studies with a wide variety of lipid compositions in combination with different types of nucleotides (i.e., DNA, siRNA, mRNA) have been performed on cationic-lipoplex systems, resulting in a profound understanding of structural coherencies and internal phase properties. For these lipoplexes, typically much narrower Bragg peaks up to several orders can be observed, often pointing toward lamellar organization[209,210]. On the other hand, ionizable-LNP exhibit an organization between a hexagonal organization or in the form of individual inverse micelles (or ‘current bun’) organization[76,211].

Little research has been done investigating the impact of these manufacturing procedures in the properties and activity of identically composed lipid nanocarriers[127]. Multiple authors have suggested that the LNP manufacturing process, where an ethanolic mixture is mixed with mRNA aqueous phase, is beneficial for nucleic acid delivery[89]. In a recent head-to-head comparison, Kubota *et al.* suggested that LNP assembly protocol would be preferable to LPX procedure since siRNA in LNP is localized more in the core and less susceptible to degradation[127]. Identically composed ionizable lipid comprising LPX and LNP exhibits a low internal organization, where only a few repeat units, presumably RNA lipid complexes, are present in arrays with the corresponding repeat distance (Figure 3.1-2, Figure 3.1-7, Figure 3.1-17, Figure 3.1-24). LPX showed increased zeta potential, hemolytic rate, and lower mRNA encapsulation efficiency supporting the hypothesis that the ionizable lipids might be more localized on the surface, as previously described[127]. Nevertheless, LPX and LNP mediated similar biodistribution and potency in mice (Figure 3.1-8,Figure 3.1-9). It is plausible to assume that on the one hand, the higher disposition of cationic lipids on the surface of LPX could result in less tight RNA binding, thereby

improving the mRNA release in the cytosol. On the other hand, the higher surface charge might foster cell interactions, resulting in higher uptake and improved protein expression.

Both technologies can be used for manufacturing successful ionizable-based lipid nanoparticles, according to the type of payload, dose, performance, and GMP requirements. Particularly, the liposome technology offers flexibility in the development of novel mRNA-drugs. For example, pre-formed liposomes can be manufactured at large scales and stored for extended period of time. In one approach, these stored-liposomes can be used to manufacture locally RNA-LPX in individual doses for personalized nanomedicines (such as cancer vaccines). On the other hand, these stored-liposomes can also be mixed with RNA using rapid mixing technologies to produce RNA-formulations, overcoming certain drawbacks associated with dialyzes processes, storage, and time. The possibility of using different technologies may provide novel opportunities in drug delivery and mRNA therapy.

4.2 Fine Tuning of Lipid Nanoparticle for Improved and Safer mRNA Delivery

Optimal size Depends on the Functionality of the mRNA

The majority of reports suggest a sub-100 nm LNP as the optimal particle size for RNA intracellular delivery. Indeed, the vast number of reports aims to deliver specifically to hepatocytes in the liver[68,71,89,212]. The optimal particle size for successful protein expression was achieved with 200 nm rather than with 100 nm nanoparticles (Figure 3.1-8, Figure 3.1-9 and Figure S 4).

Particle size plays an important role in targeting specific organs and cell types within the organs [68,71,126,213]. For instance, Akinc *et al.* showed that sub-100 nm particles could interact more readily with hepatocytes resulting in improved liver silencing [68]. In another report, Sago et al. showed that different types of cells in the liver (Kupfer cells, parenchymal hepatocytes, and LSECS) were targeted in a particle-sized manner[214]. On the another hand, Kranz *et a*l showed that negatively charged liposomes of 200 nm sized efficiently target the spleen[198]. Lipid nanoparticles with 100 nm preferentially target hepatocytes and thus, the liver, in line with previous results[68,71]. While, hematopoietic cells and hepatocytes were efficiently target by 200 nm-particles, and therefore target both liver and spleen (Figure 3.1-8 and Figure 3.1-10). The positive effect of particle size on the functional mRNA expression could be in part attributed to the targeting of hematopoietic cells besides hepatocytes, which could account for the increase in the overall expression. However, the interaction of RNA formulations with hematopoietic cells may trigger a generalized inflammatory response, which is undesirable in protein replacement therapy. In this case, relevant toxicologic studies are required to further evaluate this approach. Nevertheless, certain mRNA therapies require maximum protein expression, which may be independent of the specific target cell type, and thus this approach could be of relevance.

On the other hand, particles with larger size may also contain a higher number of mRNA copies per nanoparticle[215]. A higher number of copies of mRNA could, in part, contribute for increased expression in the liver and spleen observed in mice when comparing 100 nm to 200 nm nanoparticles. Similar observations were reported previously *in vitro*, where expression was increased when LNP size was incremented from 50 to 130 nm[156]. Further studies beyond the scope of this thesis are required to further elucidate this coherencies.

Optimal particle size may vary within payload, organ, tissue, or specific cell type. Even though sub-100 nm particles offer GMP advantages (such as sterile filtration), larger particles may substantially

improve the mRNA functionality offering several benefits: go beyond liver, enable lower doses to be administered, and thus safety. Particle size needs to be carefully engineered accordingly the tissue and/organ desired for each type of therapeutic application for optimal LNP performance.

Screening is Unavoidable in Designing Improved Lipid Nanoparticles

The majority of the studies focuses on the development of ionizable lipids based on structure-activity relationships of ionizable lipids to improve LNP efficacy[104,181,216–218].Our results showed that pKa value and hemolytic rate (pH5.4/pH7.4) is strongly correlated with the *in vitro* potency. The pKa of ionizable lipid is a crucial property of the ionizable headgroups of the LNP, which determines the ionization behavior and surface charge of the nanoparticles, which substantially influences their stability, potency, and toxicity. the charge state of the amine headgroups play a role in the interaction with negatively charged blood proteins, cellular uptake, endosomal escape and biodistribution[105,181]. An optimal pKa range for delivery of mRNA has been found between 6.2 - 6.8[104]. A novel ionizable lipid, DPL14 with a pKa ~6.4 mediated improved potency and safety (Figure 3.1-15, Figure 3.2-2, Figure 3.2-2). Other factors which were not investigated in this thesis, such as cell uptake, mRNA release, and LNP stability may have played a role. The evaluation of multiple parameters can be used as reliable tool for prescreening LNP for *in vivo* administration, and thus reduce the animals used in preclinical studies and minimize false negatives by improving *in vitro- in vivo* correlations.

In addition of ionizable lipid, a concise data base for the effect of selected helper lipids (DSPC, DOPC and DOPE) on the particle properties and biological performance of the LNP was generated in this thesis. The choice of the helper lipid with dictate particle properties, potency, biodistribution and stability (Figure 3.1-16, Figure 3.1-19). SAXS investigations revealed the presence of packing constraints within the lipid formulation) leading to poor particle formation, diminished mRNA encapsulation and reduced potency, particularly at high contents of saturated PC, such as DSPC, since it adopts lamellar structures and high T_m leading to stable lipid nanoparticles for successful hepatic silencing. It is important to highlight that the majority of LNP for NA comprised only 10 mol % of DSPC. The packing constraints could be reduced by the presence of unsaturated aliphatic chains and a more pronounced ‘cone shape’ like structures, such as DOPE, which adopts non-bilayer inverted hexagonal HII phase, thus improving characteristics of DOPE formulations[106,219,220]. The overall expression significantly increased with up to 30 mol % of DOPE, independently of administration route. It has been suggested that DOPE might reduce the membrane stability, resulting in a looser complexation of the mRNA, thereby promoting endosomal escape of mRNA and release into the cytosol[106]. On the other hand, extremely high contents in DOPE (> 50 mol %) reduced substantially the protein expression in the injected area, however also reduced off-target effects (herein described for IM applications). DOPE in high contents can also substantially reduce the stability of the membrane due to the low T_m and non-bilayer inverted hexagonal HII phases, that were often associated with protein opsonization[106]. An optimal balance between the fraction of DOPE might yield optimal performance and specificity for a given indication. Further optimization of those LNP with novel ionizable lipids for intramuscular application may help to improve the potency without increasing the off-target effects.

The targeting and efficacy are a result of the synergism of the lipid composition design. A multiparametric analysis may help to identify the relevant relationships between structure, biological

function, and potency. Moreover, it may improve the *in vitro* screening reducing false positives, and facilitate the design. Despite complex coherencies, data can serve as a good basis for selecting formulations for a specific therapeutic application. Nevertheless, screening and optimization is unavoidable in engineering and designing the next generation of lipid nanoparticles for NA delivery. Novel strategies are remain required to further expand the knowledge and accelerate the screening procedure.

Alternatives to PEGylated Lipid Nanoparticle for Functional mRNA Delivery

PEG-lipids enable both engineering and improved particle pharmacokinetics. However, PEGylation has substantial disadvantages concerning activity and safety[139]. In this thesis, various alternative approaches were used to formulate non-PEGylated LNP by rapid mixing. In one approach, mRNA was used to formulate negatively charged LNP, where high electrostatic repulsion enabled the colloidal stability. Indeed, previously mRNA-decorated LPX were used to specifically target the spleen and inducing immune response showing the beneficial properties of mRNA-decorated nanocarriers[198].A In another approach, proteins have been widely used in the drug delivery field for engineering nanoparticles for the delivery of alternative moieties[221]. In a similar manner, proteins (e.g., BSA) were used to decorate lipid nanocarriers, a common strategy in the field to target specific diseases[222]. S surfactants, such as poloxamers, consisting of a hydrophilic head group and a hydrophobic tail, which have no charge and are relatively non-toxic, also enabled the formulation of mRNA-LNP by rapid mixing. Polyppetoids, such as pSar-conjugated lipids, which was investigated into more detail, showed promising results on the engineering robustness and potency of LNP formulated in the absence of PEG-conjugated lipids. To our knowledge, these data are the first evidence that alternative moieties could be used to formulate mRNA-loaded LNP in absence of PEG-conjugated lipid by rapid mixing techniques.

The novel approaches described in this thesis for LNP manufacturing and design, despite preliminary data, may open novel possibilities for engineering novel formulations for RNA delivery. Further experiments are required to evaluate the feasibility and performance of these novel PEG-free LNP for drug delivery.

4.3 Polysarcosine-functionalized Lipid Nanoparticles for Therapeutic mRNA delivery

pSarcosinylated Lipids as a Tool for Particle Engineering and Improved Efficacy and Tolerability

pSar-conjugated lipids, made of repetitive units of the endogenous amino acid sarcosine (N-methylated glycine), demonstrated to be a promising strategy for manufacturing non-PEGylated nanoparticles[148,149,199,223]. The incorporation of pSar lipid enabled the formation of colloidal stable lipid nanoparticles, where the size decreased with increased pSar lipid surface density (through increasing pSar chain length and the molar fraction of the lipid) (Figure 3.1-23). Moreover, pSar lipids seemed to disturb at a lower extent the internal organization of LNP than PEG lipids; since a loss of organization at much lower molar fractions was observed when PEG lipids were used. Finally, pSar lipid density has a positive effect on the *in vitro* performance, whereas the activity of PEGylated systems decreased with increased PEG lipid fraction (Figure 3.1-25)[196].

These results can be explained in part by the fact that, in opposite to PEG-DMG, pSar lipids have a single aliphatic chain, resulting in lower disturbance of the lipid bilayer. Furthermore, the single aliphatic chain of pSar lipid could increase the exchangeability rate, and thus facilitate the electrostatic binding and uptake by the cell membranes. Sakurai *et al*. previously reported that monoalkyl *PEG* (PEG-MO) did not hamper the uptake and activity due to its rapid desorption[224]. On the other hand, the increase of activity with the pSar fraction might be a result of the chemical nature of this grafting moiety, where the secondary amine as an end group seemed to facilitate the electrostatic binding with negatively charged cell membranes (Figure S 13).

pSar technology may open novel options for the combination of particle engineering and optimization of biological activity. pSar lipids are versatile, where the easy variation of lipophilic and hydrophilic moieties, or end-group modification, allows to tailor nanoparticles according to the desired targeting functions (Figure 3.1-8). Indeed, optimized polysarcosine-functionalized LNP, in combination with novel ionizable lipid, showed improved hepatic potency and safety (Figure 3.2-2, Figure 3.2-4 and Figure 3.2-5)[196,225]. Nevertheless, decrease in expression of EPO for both pSar and PEGylated LNP after multiple injections in mice, suggesting, suggesting accelerated clearance of both systems. Several reports demonstrated the low immunogenicity of polysarcosine in different animal models (zebrafish embryos and mice[200], rabbits and rats[201]). Moreover, ABC phenomenon could be also attributed to other lipids or components, such PC lipids, in the formulation, which firstly induce IgM and then, upon repeated dosing, binds to the LNP leading to formation of anti-PEG IgM and anti-PEG IgG responses[202].

The development of effective and safe lipid-based formulations for mRNA delivery is one of the biggest challenges for nucleic acid therapy[226]. For therapeutic purposes, high protein expression is critical specifically when lower doses are required to be administered into patients in order to reduce undesirable toxic effects. Further studies, such as investigation of the tolerability in other animal models like rat or non-human primates, will be necessary to fully elucidate the applicability of the pSar LNP as RNA delivery systems with improved safety profile.

4.4 Self-amplifying RNA-LNP as a vaccine against infectious diseases

Self-amplifying RNA systems needs to be tailored independently of mRNA carriers

Self-amplifying RNA vaccines have been a promising strategy due to the RNA's self-amplifying properties, which allows for lower doses to be administered possible reducing secondary effects [176]. The majority of reports focused on the identification of cationic lipid for improved saRNA vaccine formulations [227–229]. The design and optimization of saRNA nanoparticles in this section was based on the strategies applied and lessons learned from the mRNA optimization. As a result, it could be shown that saRNA systems need to be independently tailored of mRNA nanocarriers (Figure 3.3-2). Self-amplifying RNA constructs are 4.5x larger than mRNA (9000 nt vs 2000 nt), which results in higher instability of saRNA constructs. mRNA and saRNA have completely distinct translation procedures. And, finally, little is known about RNA construct performance on different types of cells (such as DCs or skeletal muscle).

In addition, our results illustrated the importance to formulate the disease-relevant payload for the evaluation and screening in early preclinical settings. Little correlation between expression and immunogenicity was found in this study, even though the expression and immunogenicity were addressed by measuring luciferase expression and specific cell responses against luciferase peptides

through ELISpot assay (Figure 3.3-2). This method was slightly different than the one implemented by Hasset *et al*, where HA and LUC-encoding mRNA have been co-formulated in the LNP, despite the similar findings[104]. Indeed, we found that highly expressed formulations in luciferase setting lead to reduced HA-specific immunogenicity, which was lipid dependent (Figure 3.3-2), reinforcing the need for a balance between expression and immune stimulation for optimal RNA vaccine[104,230,231]. For example, increased immune stimulation obtained via production of type I interferon could reduce the expression of RNA vaccines[231]. Besides, increased concentration of saRNA-formulation resulted in diminished protein expression and immune response[176].

Higher protonation level was required for vaccination, which can boost the immune system and increased response (Figure 3.3-2)[232]. The ionizable lipid DODMA (pKa ~7) showed increased immunogenicity compared to other ionizable lipids (Figure 3.3-2). Hassett et al. also reported that ionizable lipids with pKa of around 6.6 and 6.8 were optimal for intramuscular vaccination, which is slightly elevated when compared to optimal pKa for liver targeting[104]. Indeed, the mRNA construct and delivery system are both important for adjuvant for inducing immune responses from an mRNA vaccine. It is worth mention that several reports have demonstrated the immunostimulatory potential of the formulations [69, 234, 235)].

Beyond ionizable lipid, grafted-lipid had the highest impact on formulation performance. pSar-lipids and PEG-DMG improved the immunogenicity compared to C16 PEG cer lipid *in vivo (*Figure 3.3-3*)*. When these formulations were complexed with HA-specific saRNA, lower antibody responses and comparable virus neutralization titers were obtained for both pSar and PEG-DMG. Notably, A-8 formulation induced higher CD8+ T cells while pSar and PEG-DMG generated more efficiently CD4+ T cell, illustrating that formulations have the capabilities to shape the type of immune reaction. To clarify the immunostimulatory potential of lipid formulations, it would be required to administrate empty lipid formulations (no mRNA). However, empty formulations might not resemble a lipid-complex since empty formulations may have a different lipid disposition, size, structure, and others. Therefore, it is overly complex to have a deep understanding of the immunostimulatory potential of the lipids alone.

Self-amplifying mRNA vaccines modalities are especially advantageous in the infectious disease field due to their ability to be rapidly tailored to sequences of outbreak viruses and new emergent strains. However, the tolerability determines the success of a new vaccine, since vaccines are administrated to healthy individuals throughout different stages of life, from 1-day-old neonates to the elderly. saRNA-LNP could elicit EBOV-GP specific antibody and neutralizing responses in mice. Nevertheless, further experiments are required to investigate the tolerability of this new vaccine.

4.5 Considerations to engineer the next generation of delivery vehicles

Future delivery vehicles need to be carefully engineered and characterized for each payload, administration route and therapeutic application. Novel approaches can be explored to gain an understanding on the relationship between formulation properties and diseases, predict novel components or refine formulations for specific disease. To achieve clinical translation, GMP is necessary to ensure drug quality and therapeutic effects, taking in account considerations such as storage conditions and safety profiles.

Good manufacturing practice

All formulation components and materials are required to be RNase free since mRNA is easily degraded. A series of GMP standard tests, including evaluation of physical parameters, compendial and quality testing are required for release drug products. Therefore, development of drug delivery system having in consideration the GMP requirements will accelerate the translation of novel mRNA therapies.

Screening and evaluation

The lipid components and the lipid nanoparticle properties must be engineered and refined taking into consideration the payload, disease, administration route and tissue or organ-target. Further understanding on nanoparticle cell-interaction, uptake mechanism and endosomal escape may help to redesign novel formulations for efficient intracellular delivery of mRNA.

Novel materials and formulation, such as polymer-lipid hybrid particles, may offer several advantages to improve targeting selectivity and potency. For example, the incorporation of poly (β-amino ester) into lipid nanoparticles facilitated the endosomal escape and improved the overall potency in the lungs[233]. Other polymers, such as PEI, could confer several benefits in the endosomal release, and, thus, in the performance of LNP. Additionally, naturally derived membrane lipids (exosomes and cell membranes) can also be applied for RNA delivery to achieve organ-targeted delivery[234].

Screening and evaluation of emerging novel biomaterials and lipid nanoparticles is unavoidable... Barcoded mRNA techniques that allow in vivo high-throughput profiling of lipid nanoparticle distribution at the cellular level has been developed[235]. Also, novel strategies have been developed to overcome the limitations of in vitro systems, such 'organ-on-a-chip' tools[236]. Finally, data mining can help to explore the complex relationships between formulation properties and diseases through machine learning, which potentially will help us to gain further understanding of formulation behaviors of interest. Such techniques can predict novel components or refine formulations for specific diseases[237,238]

Stability upon storage

Although stability upon storage was not address in this thesis, this is a crucial factor for a successful clinical translation, since lipid nanoparticle–mRNA formulations stored in aqueous media have a short-term stability. Different storage conditions (e.g., frozen or freeze-dried), as well as cryoprotectants (e.g., sucrose, trehalose or mannitol) can be used to improve the long-term stability of lipid nanoparticle–mRNA formulations[239]. For example, 5% (w/v) sucrose or trehalose was included into the formulation, stored in liquid nitrogen, to maintain its efficacy in vivo after 3 months storage. The recent pandemics also highlighted the importance of investigating the factors which impact long-term storage and develop mRNA formulations that do not require cold or frozen storage. Such attributes would decrease the production and transportation cost, expedite the process, and increase the availability in emerging countries.

Safety profile

The lipid components and particle morphology dictate the safety profile of RNA therapeutics. Therefore, biocompatibility and biodegradability must be considered when designing and screening lipids and formulations for RNA therapeutics. In addition, synergistic effects between components and

API must be addresses in pre-clinical settings, in preference in relevant models, to avoid safety-related failures in later clinical stages.

The inclusion of natural-derived or biodegradable components could improve the fast elimination of lipid nanoparticles from plasma and tissues, improving their safety and tolerability. In another approach, self-adjuvant and targeted-lipids might help to boost efficacy and targeting, while other lipids components may allow the incorporation of chemotherapies or other small molecules to enable dual-therapies[240,241].

CHAPTER 5 | Conclusion

RNA-LNP formulations hold great promise against unmet medical needs. Minor alterations, such as RNA type, in the LNP formulation might have an impact on physicochemical characteristics and, thus, in the performance of the mRNA therapeutic.

In this thesis, a comprehensive picture of the state-of-the-art design of lipid nanoparticles for mRNA delivery was drawn. The internal organization of mRNA lipid formulations obtained from different manufacturing protocols, comprising different lipid mixtures and RNA formats was investigated and correlated with activity. mRNA lipid-based therapeutics manufactured using either the LPX or the LNP manufacturing process mediated similar levels of protein secretion, widening the range of possibilities and opportunities in RNA therapeutic field. The different protocols allowed to accurately control particle size in a wider range, allowing to determine the RNA-lipid formulation biodistribution and potency. Apart from the physicochemical properties of the formulation, it was further shown that the combination with other components, such the selection of helper lipids and grafting moieties, can enable targeting different cell types inside the liver and organs beyond the liver.

For the first time non-PEGylated LNP were successfully engineered for mRNA delivery. Among those, pSar grafted lipids showed promising results by enabling particle size control without diminishing the activity of the formulations, opening novel possibilities for the combination of particle engineering and optimization of biological activity. In combination with novel ionizable lipids, pSar LNP displayed improved hepatic potency and tolerability, illustrating that pSar-based nanoparticle technology is promising for the development of next-generation potent and safe RNA therapeutics for clinical translation.

Finally, throughout this thesis, LNP formulations were developed for intramuscular application of saRNA vaccines against infectious diseases – an important field nowadays since the self-replicative properties of these vaccines allow for lower doses to be administered, possibly reducing secondary effects. Three of the thirteen *in vivo* candidates showed high antibody and neutralization titers against HA-specific antigens. Optimized saRNA LNP elicited EBOV-GP specific antibody and neutralization titers, and T cell responses, and thus poses as a promising candidate for vaccination against infectious diseases.

Overall, the results demonstrate that fine tuning of formulations is required for each payload, administration route, and disease for optimal performance. For example, an ideal formulation for intravenous application of mRNA for RNA therapeutics is not optimal for intramuscular administration of saRNA for vaccination purposes. Other considerations, such as stability upon storage, and safety profile, must be considered for designing the next generation of lipid nanoparticles for RNA therapy.

REFERENCES

1. Wolff J, Malone R, Williams P, Chong W, Acsadi G, Jani A, et al. Direct gene transfer into mouse muscle in vivo. Science. 1990;247(4949):1465–8.

2. Sahin U, Karikó K, Türeci Ö. mRNA-based therapeutics — developing a new class of drugs. Nat Rev Drug Discov. 2014;13(10):759–80.

3. Brenner S, Jacob F, Meselson M. An Unstable Intermediate Carrying Information from Genes to Ribosomes for Protein Synthesis. Nature. 1961;190(4776):576–81.

4. Baiersdörfer M, Boros G, Muramatsu H, Mahiny A, Vlatkovic I, Sahin U, et al. A Facile Method for the Removal of dsRNA Contaminant from In Vitro-Transcribed mRNA. Mol Ther - Nucleic Acids. 2019;15:26–35.

5. Pardi N, Hogan MJ, Porter FW, Weissman D. mRNA vaccines — a new era in vaccinology. Nat Rev Drug Discov. 2018;17(4):261–79.

6. Zhang C, Maruggi G, Shan H, Li J. Advances in mRNA Vaccines for Infectious Diseases. Front Immunol. 2019;10:594.

7. Abudayyeh OO, Gootenberg JS, Essletzbichler P, Han S, Joung J, Belanto JJ, et al. RNA targeting with CRISPR–Cas13. Nature. 2017;550(7675):280–4.

8. Zhang HX, Zhang Y, Yin H. Genome editing with mRNA encoding ZFN, TALEN and Cas9. Mol Ther. 2019;27(4):735–46.

9. Pardi N, Muramatsu H, Weissman D, Karikó K. Synthetic Messenger RNA and Cell Metabolism Modulation, Methods and Protocols. Methods Mol Biology. 2012;969:29–42.

10. Weissman D, Pardi N, Muramatsu H, Karikó K. Synthetic Messenger RNA and Cell Metabolism Modulation, Methods and Protocols. Methods Mol Biology. 2012;969:43–54.

11. Kormann MSD, Hasenpusch G, Aneja MK, Nica G, Flemmer AW, Herber-Jonat S, et al. Expression of therapeutic proteins after delivery of chemically modified mRNA in mice. Nat Biotechnol. 2011;29(2):154–7.

12. Karikó K, Muramatsu H, Keller JM, Weissman D. Increased Erythropoiesis in Mice Injected With Submicrogram Quantities of Pseudouridine-containing mRNA Encoding Erythropoietin. Mol Ther. 2012;20(5):948–53.

13. Levy O, Zhao W, Mortensen LJ, LeBlanc S, Tsang K, Fu M, et al. mRNA-engineered mesenchymal stem cells for targeted delivery of interleukin-10 to sites of inflammation. Blood. 2013;122(14):e23–32.

14. Kaczmarek JC, Kowalski PS, Anderson DG. Advances in the delivery of RNA therapeutics: from concept to clinical reality. Genome Med. 2017;9(1):60.

15. Kowalski PS, Rudra A, Miao L, Anderson DG. Delivering the Messenger: Advances in Technologies for Therapeutic mRNA Delivery. Mol Ther. 2019;27(4):710–28.

16. Aberle JH, Aberle SW, Kofler RM, Mandl CW. Humoral and Cellular Immune Response to RNA Immunization with Flavivirus Replicons Derived from Tick-Borne Encephalitis Virus. J Virol. 2005;79(24):15107–13.

17. Cox D, Platt R, Zhang F. Therapeutic genome editing: prospects and challenges. Nat Med. 2015;21(2):121–31.

18. Yin H, Kauffman KJ, Anderson DG. Delivery technologies for genome editing. Nat Rev Drug Discov. 2017;16(6):387–99.

19. Cheng Q, Wei T, Farbiak L, Johnson LT, Dilliard SA, Siegwart DJ. Selective organ targeting (SORT) nanoparticles for tissue-specific mRNA delivery and CRISPR–Cas gene editing. Nat Nanotechnol. 2020;1–8.

20. Finn JD, Smith A, Patel MC, Shaw L, Youniss MR, Heteren J van, et al. A Single Administration of CRISPR/Cas9 Lipid Nanoparticles Achieves Robust and Persistent In Vivo Genome Editing. Cell Reports. 2018;22(9):2227–35.

21. Houseley J, Tollervey D. The Many Pathways of RNA Degradation. Cell. 2009;136(4):763–76.

22. Kawai T, Akira S. Innate immune recognition of viral infection. Nat Immunol. 2006;7(2):131–7.

23. Heil F, Hemmi H, Hochrein H, Ampenberger F, Kirschning C, Akira S, et al. Species-Specific Recognition of Single-Stranded RNA via Toll-like Receptor 7 and 8. Science. 2004;303(5663):1526–9.

24. Diebold SS, Massacrier C, Akira S, Paturel C, Morel Y, Reis e Sousa C. Nucleic acid agonists for Toll-like receptor 7 are defined by the presence of uridine ribonucleotides. Eur J Immunol. 2006;36(12):3256–67.

25. Alexopoulou L, Holt AC, Medzhitov R, Flavell RA. Recognition of double-stranded RNA and activation of NF-κB by Toll-like receptor 3. Nature. 2001;413(6857):732–8.

26. Karikó K, Muramatsu H, Ludwig J, Weissman D. Generating the optimal mRNA for therapy: HPLC purification eliminates immune activation and improves translation of nucleoside-modified, protein-encoding mRNA. Nucleic Acids Res. 2011;39(21):e142–e142.

27. Karikó K, Ni H, Capodici J, Lamphier M, Weissman D. mRNA Is an Endogenous Ligand for Toll-like Receptor 3. J Biol Chem. 2004;279(13):12542–50.

28. Yoneyama M, Kikuchi M, Natsukawa T, Shinobu N, Imaizumi T, Miyagishi M, et al. The RNA helicase RIG-I has an essential function in double-stranded RNA-induced innate antiviral responses. Nat Immunol. 2004;5(7):730–7.

29. Hervas-Stubbs S, Perez-Gracia J, Rouzaut A, Sanmamed MF, Bon A, Melero I. Direct Effects of Type I Interferons on Cells of the Immune System. Clin Cancer Res. 2011;17(9):2619–27.

30. Verbeke R, Lentacker I, Smedt SCD, Dewitte H. Three decades of messenger RNA vaccine development. Nano Today. 2019;28:100766.

31. Devoldere J, Dewitte H, Smedt SC, Remaut K. Evading innate immunity in nonviral mRNA delivery: don't shoot the messenger. Drug Discov Today. 2016;21(1):11–25.

32. Niessen AGO von, Poleganov MA, Rechner C, Plaschke A, Kranz LM, Fesser S, et al. Improving mRNA-based therapeutic gene delivery by expression augmenting 3'-untranslated regions identified by cellular library screening. Mol Ther. 2018;27(4):824–36.

33. Jemielity J, Fowler T, Zuberek J, Stepinski J, Lewdorowicz M, Niedzwiecka A, et al. Novel "anti-reverse" cap analogs with superior translational properties. Rna. 2003;9(9):1108–22.

34. Grudzien-Nogalska E, Kiledjian M. New insights into decapping enzymes and selective mRNA decay: mRNA Decapping Enzymes in mRNA Decay. Wiley Interdiscip Rev Rna. 2016;8(1):e1379.

35. Jeught KV der, Koker SD, Bialkowski L, Heirman C, Joe PT, Perche F, et al. Dendritic Cell Targeting mRNA Lipopolyplexes Combine Strong Antitumor T-Cell Immunity with Improved Inflammatory Safety. Acs Nano. 2018;12(10):9815–29.

36. Rosigkeit S, Meng M, Grunwitz C, Gomes P, Kreft A, Hayduk N, et al. Monitoring Translation Activity of mRNA-Loaded Nanoparticles in Mice. Mol Pharmaceut. 2018;15(9):3909–19.

37. Johanning FW, Conry RM, LoBuglio AF, Wright M, Sumerel LA, Pike MJ, et al. A sindbis virus mRNA polynucleotide vector achieves prolonged and high level heterologous gene expression in vivo. Nucleic Acids Res. 1995;23(9):1495–501.

38. Zhou X, Berglund P, Rhodes G, Parker SE, Jondal M, Liljeström P. Self-replicating Semliki Forest virus RNA as recombinant vaccine. Vaccine. 1994;12(16):1510–4.

39. Pamudurti NR, Bartok O, Jens M, Ashwal-Fluss R, Stottmeister C, Ruhe L, et al. Translation of CircRNAs. Mol Cell. 2017;66(1):9-21.e7.

40. Wesselhoeft RA, Kowalski PS, Anderson DG. Engineering circular RNA for potent and stable translation in eukaryotic cells. Nat Commun. 2018;9(1):2629.

41. Thi TTH, Suys EJA, Lee JS, Nguyen DH, Park KD, Truong NP. Lipid-Based Nanoparticles in the Clinic and Clinical Trials: From Cancer Nanomedicine to COVID-19 Vaccines. Nato Adv Sci Inst Se. 2021;9(4):359.

42. Bangham AD, Standish MM, Watkins JC. Diffusion of univalent ions across the lamellae of swollen phospholipids. J Mol Biol. 1965;13(1):238-IN27.

43. Bangham AD, Horne RW. Negative staining of phospholipids and their structural modification by surface-active agents as observed in the electron microscope. J Mol Biol. 1964;8(5):660-IN10.

44. Gier JD, Mandersloot JG, Deenen LLMV. Lipid composition and permeability of liposomes. Biochimica Et Biophysica Acta Bba - Biomembr. 1968;150(4):666–75.

45. Gregoriadis G, Ryman BE. Liposomes as carriers of enzymes or drugs: a new approach to the treatment of storage diseases. Biochem J. 1971;124(5):58P-58P.

46. Gregoriadis G. Drug entrapment in liposomes. FEBS Letter. 1973;3(36):292–6.

47. Gregoriadis G. Liposome Technology. Vol. Volume 3. CRC press; 1992.

48. Bulbake U, Doppalapudi S, Kommineni N, Khan W. Liposomal Formulations in Clinical Use: An Updated Review. Pharm. 2017;9(2):12.

49. Semple SC, Klimuk SK, Harasym TO, Santos ND, Ansell SM, Wong KF, et al. Efficient encapsulation of antisense oligonucleotides in lipid vesicles using ionizable aminolipids: formation of novel small multilamellar vesicle structures. Biochimica Et Biophysica Acta Bba - Biomembr. 2001;1510(1–2):152–66.

50. Akinc A, Maier MA, Manoharan M, Fitzgerald K, Jayaraman M, Barros S, et al. The Onpattro story and the clinical translation of nanomedicines containing nucleic acid-based drugs. Nat Nanotechnol. 2019;14(12):1084–7.

51. Israelachvili JN, Mitchell DJ, Ninham BW. Theory of self-assembly of hydrocarbon amphiphiles into micelles and bilayers. J Chem Soc Faraday Transactions 2 Mol Chem Phys. 1976;72(0):1525–68.

52. Kulkarni CV, Wachter W, Iglesias-Salto G, Engelskirchen S, Ahualli S. Monoolein : a magic lipid? Phys Chem Chem Phys. 2010;13(8):3004–21.

53. Wang N, Chen M, Wang T. Liposomes used as a vaccine adjuvant-delivery system: From basics to clinical immunization. J Control Release. 2019;303:130–50.

54. Zhang J, Fan H, Levorse DA, Crocker LS. Interaction of Cholesterol-Conjugated Ionizable Amino Lipids with Biomembranes: Lipid Polymorphism, Structure–Activity Relationship, and Implications for siRNA Delivery. Langmuir. 2011;27(15):9473–83.

55. Wasungu L, Hoekstra D. Cationic lipids, lipoplexes and intracellular delivery of genes. J Control Release. 2006;116(2):255–64.

56. Dimitriadis GJ. Entrapment of ribonucleic acids in liposomes. Febs Lett. 1978;86(2):289–93.

57. Malone R, Felgner P, Verma I. Cationic liposome-mediated RNA transfection. Proc National Acad Sci. 1989;86(16):6077–81.

58. Zhi D, Bai Y, Yang J, Cui S, Zhao Y, Chen H, et al. A review on cationic lipids with different linkers for gene delivery. Adv Colloid Interfac. 2017;253(Chem Rev 115 2015):117–40.

59. Martinon F, Krishnan S, Lenzen G, Magné R, Gomard E, Guillet J, et al. Induction of virus-specific cytotoxic T lymphocytes in vivo by liposome-entrapped mRNA. Eur J Immunol. 1993;23(7):1719–22.

60. Karikó K, Muramatsu H, Welsh FA, Ludwig J, Kato H, Akira S, et al. Incorporation of Pseudouridine Into mRNA Yields Superior Nonimmunogenic Vector With Increased Translational Capacity and Biological Stability. Mol Ther. 2008;16(11):1833–40.

61. Felgner JH, Kumar R, Sridhar CN, Wheeler CJ, Tsai YJ, Border R, et al. Enhanced gene delivery and mechanism studies with a novel series of cationic lipid formulations. J Biological Chem. 1994;269(4):2550–61.

62. McManus MT, Sharp PA. Gene silencing in mammals by small interfering RNAs. Nat Rev Genet. 2002;3(10):737–47.

63. Buyens K, Demeester J, Smedt SSD, Sanders NN. Elucidating the Encapsulation of Short Interfering RNA in PEGylated Cationic Liposomes. Langmuir. 2009;25(9):4886–91.

64. Landesman-Milo D, Peer D. Toxicity profiling of several common RNAi-based nanomedicines: a comparative study. Drug Deliv Transl Re. 2014;4(1):96–103.

65. Jeffs LB, Palmer LR, Ambegia EG, Giesbrecht C, Ewanick S, MacLachlan I. A Scalable, Extrusion-Free Method for Efficient Liposomal Encapsulation of Plasmid DNA. Pharmaceut Res. 2005;22(3):362–72.

66. Semple SC, Akinc A, Chen J, Sandhu AP, Mui BL, Cho CK, et al. Rational design of cationic lipids for siRNA delivery. Nat Biotechnol. 2010;28(2):172–6.

67. Mahon KP, Love KT, Whitehead KA, Qin J, Akinc A, Leshchiner E, et al. Combinatorial Approach to Determine Functional Group Effects on Lipidoid-Mediated siRNA Delivery. Bioconjugate Chem. 2010;21(8):1448–54.

68. Akinc A, Goldberg M, Qin J, Dorkin JR, Gamba-Vitalo C, Maier M, et al. Development of Lipidoid–siRNA Formulations for Systemic Delivery to the Liver. Mol Ther. 2009;17(5):872–9.

69. Geall AJ, Verma A, Otten GR, Shaw CA, Hekele A, Banerjee K, et al. Nonviral delivery of self-amplifying RNA vaccines. Proc National Acad Sci. 2012;109(36):14604–9.

70. Pardi N, Tuyishime S, Muramatsu H, Kariko K, Mui BL, Tam YK, et al. Expression kinetics of nucleoside-modified mRNA delivered in lipid nanoparticles to mice by various routes. J Control Release. 2015;217(Science 255 1992):345–51.

71. Jayaraman M, Ansell SM, Mui BL, Tam YK, Chen J, Du X, et al. Maximizing the Potency of siRNA Lipid Nanoparticles for Hepatic Gene Silencing In Vivo. Angewandte Chemie Int Ed. 2012;51(34):8529–33.

72. Maier MA, Jayaraman M, Matsuda S, Liu J, Barros S, Querbes W, et al. Biodegradable Lipids Enabling Rapidly Eliminated Lipid Nanoparticles for Systemic Delivery of RNAi Therapeutics. Mol Ther. 2013;21(8):1570–8.

73. Sedic M, Senn JJ, Lynn A, Laska M, Smith M, Platz SJ, et al. Safety Evaluation of Lipid Nanoparticle–Formulated Modified mRNA in the Sprague-Dawley Rat and Cynomolgus Monkey. Vet Pathol. 2018;55(2):341–54.

74. Nabhan JF, Wood KM, Rao VP, Morin J, Bhamidipaty S, LaBranche TP, et al. Intrathecal delivery of frataxin mRNA encapsulated in lipid nanoparticles to dorsal root ganglia as a potential therapeutic for Friedreich's ataxia. Sci Rep-uk. 2016;6(1):20019.

75. Pardi N, Hogan MJ, Pelc RS, Muramatsu H, Andersen H, DeMaso CR, et al. Zika virus protection by a single low-dose nucleoside-modified mRNA vaccination. Nature. 2017;543(7644):248–51.

76. Leung AKK, Tam YYC, Cullis PR. Lipid nanoparticles for short interfering RNA delivery. Adv Genet. 2014;88:71–110.

77. Kulkarni JA, Darjuan MM, Mercer JE, Chen S, Meel R van der, Thewalt JL, et al. On the Formation and Morphology of Lipid Nanoparticles Containing Ionizable Cationic Lipids and siRNA. Acs Nano. 2018;12(5):4787–95.

78. Polack FP, Thomas SJ, Kitchin N, Absalon J, Gurtman A, Lockhart S, et al. Safety and Efficacy of the BNT162b2 mRNA Covid-19 Vaccine. New Engl J Med. 2020;383(27):2603–15.

79. Meure LA, Foster NR, Dehghani F. Conventional and Dense Gas Techniques for the Production of Liposomes: A Review. Aaps Pharmscitech. 2008;9(3):798.

80. Weissig. Liposomes: Methods and protocols. Vol. 606. Humana Press; 2010.

81. Mayer LD, Hope MJ, Cullis PR. Vesicles of variable sizes produced by a rapid extrusion procedure. Biochimica Et Biophysica Acta Bba - Biomembr. 1986;858(1):161–8.

82. Jr FS, Papahadjopoulos D. Comparative Properties and Methods of Preparation of Lipid Vesicles (Liposomes). Annu Rev Biophys Bio. 1980;9(1):467–508.

83. Mayhew E, Lazo R, Vail WJ, King J, Green AM. Characterization of liposomes prepared using a microemulsifier. Biochimica Et Biophysica Acta Bba - Biomembr. 1984;775(2):169–74.

84. D'Souza GGM. Liposomes, Methods and Protocols. D'Souza GGM, editor. Humana Press,; 2016.

85. Wagner A, Vorauer-Uhl K, Kreismayr G, Katinger H. The crossflow injection technique: an improvement of ethanol injection method. J Liposome Res. 2002;12(3):259–70.

86. Patil YP, Jadhav S. Novel methods for liposome preparation. Chem Phys Lipids. 2014;177:8–18.

87. Hirota S, Ilarduya CT de, Barron LG, Szoka FC. Simple Mixing Device to Reproducibly Prepare Cationic Lipid-DNA Complexes (Lipoplexes). Biotechniques. 1999;27(2):286–90.

88. Davies LA, Nunez-Alonso GA, Hebel HL, Scheule RK, Cheng SH, Hyde SC, et al. A novel mixing device for the reproducible generation of nonviral gene therapy formulations. Biotechniques. 2010;49(3):666–8.

89. Evers MJW, Kulkarni JA, Meel R der, Cullis PR, Vader P, Schiffelers RM. State-of-the-Art Design and Rapid-Mixing Production Techniques of Lipid Nanoparticles for Nucleic Acid Delivery. Small Methods. 2018;2(9):1700375.

90. Cullis PR, Hope MJ. Lipid Nanoparticle Systems for Enabling Gene Therapies. Mol Ther. 2017;25(7):1467–75.

91. Andreussi T, Galletti C, Mauri R, Camarri S, Salvetti MV. Flow regimes in T-shaped micro-mixers. Comput Chem Eng. 2015;76:150–9.

92. Williams MS, Longmuir KJ, Yager P. A practical guide to the staggered herringbone mixer. Lab Chip. 2008;8(7):1121–9.

93. Jahn A, Vreeland WN, Gaitan M, Locascio LE. Controlled Vesicle Self-Assembly in Microfluidic Channels with Hydrodynamic Focusing. J Am Chem Soc. 2004;126(9):2674–5.

94. Carugo D, Bottaro E, Owen J, Stride E, Nastruzzi C. Liposome production by microfluidics: potential and limiting factors. Sci Rep-uk. 2016;6(1):25876.

95. Zhigaltsev IV, Belliveau N, Hafez I, Leung AKK, Huft J, Hansen C, et al. Bottom-Up Design and Synthesis of Limit Size Lipid Nanoparticle Systems with Aqueous and Triglyceride Cores Using Millisecond Microfluidic Mixing. Langmuir. 2012;28(7):3633–40.

96. Stroock AD, Dertinger SKW, Ajdari A, Mezić I, Stone HA, Whitesides GM. Chaotic Mixer for Microchannels. Science. 2002;295(5555):647–51.

97. Belliveau NM, Huft J, Lin PJ, Chen S, Leung AK, Leaver TJ, et al. Microfluidic Synthesis of Highly Potent Limit-size Lipid Nanoparticles for In Vivo Delivery of siRNA. Mol Ther - Nucleic Acids. 2012;1(Science 303 2004):e37.

98. Garg S, Heuck G, Ip S, Ramsay E. Microfluidics: a transformational tool for nanomedicine development and production. J Drug Target. 2016;24(9):1–15.

99. Lee JN, Park C, Whitesides GM. Solvent Compatibility of Poly(dimethylsiloxane)-Based Microfluidic Devices. Anal Chem. 2003;75(23):6544–54.

100. Blanco E, Shen H, Ferrari M. Principles of nanoparticle design for overcoming biological barriers to drug delivery. Nat Biotechnol. 2015;33(9):941–51.

101. Adams D, Gonzalez-Duarte A, O'Riordan WD, Yang CC, Ueda M, Kristen AV, et al. Patisiran, an RNAi Therapeutic, for Hereditary Transthyretin Amyloidosis. New Engl J Med. 2018;379(1):11–21.

102. An D, Schneller JL, Frassetto A, Liang S, Zhu X, Park JS, et al. Systemic Messenger RNA Therapy as a Treatment for Methylmalonic Acidemia. Cell Reports. 2017;21(12):3548–58.

103. Sabnis S, Kumarasinghe ES, Salerno T, Mihai C, Ketova T, Senn JJ, et al. A Novel Amino Lipid Series for mRNA Delivery: Improved Endosomal Escape and Sustained Pharmacology and Safety in Non-human Primates. Mol Ther. 2018;26(6):1509–19.

104. Hassett KJ, Benenato KE, Jacquinet E, Lee A, Woods A, Yuzhakov O, et al. Optimization of Lipid Nanoparticles for Intramuscular Administration of mRNA Vaccines. Mol Ther - Nucleic Acids. 2019;15:1–11.

105. Jayaraman M, Ansell SM, Mui BL, Tam YK, Chen J, Du X, et al. Maximizing the Potency of siRNA Lipid Nanoparticles for Hepatic Gene Silencing In Vivo. Angew Chem-ger Edit. 2012;124(34):8657–61.

106. Kauffman KJ, Dorkin JR, Yang JH, Heartlein MW, DeRosa F, Mir FF, et al. Optimization of Lipid Nanoparticle Formulations for mRNA Delivery in Vivo with Fractional Factorial and Definitive Screening Designs. Nano Lett. 2015;15(11):7300–6.

107. DeRosa F, Guild B, Karve S, Smith L, Love K, Dorkin JR, et al. Therapeutic efficacy in a hemophilia B model using a biosynthetic mRNA liver depot system. Gene Ther. 2016;23(10):699–707.

108. Oberli MA, Reichmuth AM, Dorkin JR, Mitchell MJ, Fenton OS, Jaklenec A, et al. Lipid Nanoparticle Assisted mRNA Delivery for Potent Cancer Immunotherapy. Nano Lett. 2016;17(3):1326–35.

109. Fenton OS, Kauffman KJ, McClellan RL, Appel EA, Dorkin RJ, Tibbitt MW, et al. Bioinspired Alkenyl Amino Alcohol Ionizable Lipid Materials for Highly Potent In Vivo mRNA Delivery. Adv Mater. 2016;28(15):2939–43.

110. Heyes J, Palmer L, Bremner K, MacLachlan I. Cationic lipid saturation influences intracellular delivery of encapsulated nucleic acids. J Control Release. 2005;107(2):276–87.

111. Fenton OS, Kauffman KJ, Kaczmarek JC, McClellan RL, Jhunjhunwala S, Tibbitt MW, et al. Synthesis and Biological Evaluation of Ionizable Lipid Materials for the In Vivo Delivery of Messenger RNA to B Lymphocytes. Adv Mater. 2017;29(33):1606944.

112. Cheng X, Lee RJ. The role of helper lipids in lipid nanoparticles (LNPs) designed for oligonucleotide delivery. Adv Drug Deliver Rev. 2016;99:129–37.

113. Dabkowska A, Barlow D, Hughes A, Campbell R, Quinn P, Lawrence M. The effect of neutral helper lipids on the structure of cationic lipid monolayers. J Roy Soc Interface. 2011;9(68):548–61.

114. Thewalt JL, Bloom M. Phosphatidylcholine cholesterol phase diagrams. Biophys J. 1992;63(4):1176–81.

115. Semple SC, Chonn A, Cullis PR. Influence of Cholesterol on the Association of Plasma Proteins with Liposomes †. Biochemistry-us. 1996;35(8):2521–5.

116. Ellens H, Bentz J, Szoka FC. Destabilization of phosphatidylethanolamine liposomes at the hexagonal phase transition temperature. Biochemistry-us. 1986;25(2):285–94.

117. Du Z, Munye MM, Tagalakis AD, Manunta MDI, Hart SL. The Role of the Helper Lipid on the DNA Transfection Efficiency of Lipopolyplex Formulations. Sci Rep-uk. 2014;4(1):7107.

118. Yan X, Scherphof GL, Kamps JAAM. Liposome Opsonization. J Liposome Res. 2005;15(1–2):109–39.

119. Hafez IM, Ansell S, Cullis PR. Tunable pH-Sensitive Liposomes Composed of Mixtures of Cationic and Anionic Lipids. Biophys J. 2000;79(3):1438–46.

120. Maiseyeu A, Mihai G, Kampfrath T, Simonetti OP, Sen CK, Roy S, et al. Gadolinium-containing phosphatidylserine liposomes for molecular imaging of atherosclerosis. J Lipid Res. 2009;50(11):2157–63.

121. Geelen T, Yeo SY, Paulis LE, Starmans LW, Nicolay K, Strijkers GJ. Internalization of paramagnetic phosphatidylserine-containing liposomes by macrophages. J Nanobiotechnol. 2012;10(1):37.

122. Patel S, Ashwanikumar N, Robinson E, Xia Y, Mihai C, Griffith JP, et al. Naturally-occurring cholesterol analogues in lipid nanoparticles induce polymorphic shape and enhance intracellular delivery of mRNA. Nat Commun. 2020;11(1):983.

123. Paunovska K, Sanchez AJ, Sago CD, Gan Z, Lokugamage MP, Islam FZ, et al. Nanoparticles Containing Oxidized Cholesterol Deliver mRNA to the Liver Microenvironment at Clinically Relevant Doses. Adv Mater. 2019;31(14):1807748.

124. Bilensoy E. Cationic nanoparticles for cancer therapy. Expert Opin Drug Del. 2010;7(7):795–809.

125. Suk JS, Xu Q, Kim N, Hanes J, Ensign LM. PEGylation as a strategy for improving nanoparticle-based drug and gene delivery. Adv Drug Deliver Rev. 2016;99(Pt A):28–51.

126. Chen S, Tam YC, Lin P, Sung M, Tam YK, Cullis PR. Influence of particle size on the in vivo potency of lipid nanoparticle formulations of siRNA. J Control Release. 2016;235(Nat. Rev. Drug Discov. 6 2007):236–44.

127. Kubota K, Onishi K, Sawaki K, Li T, Mitsuoka K, Sato T, et al. Effect of the nanoformulation of siRNA-lipid assemblies on their cellular uptake and immune stimulation. Int J Nanomed. 2017;12:5121–33.

128. Ishida T, Masuda K, Ichikawa T, Ichihara M, Irimura K, Kiwada H. Accelerated clearance of a second injection of PEGylated liposomes in mice. Int J Pharmaceut. 2003;255(1–2):167–74.

129. Ishida T, Ichihara M, Wang X, Yamamoto K, Kimura J, Majima E, et al. Injection of PEGylated liposomes in rats elicits PEG-specific IgM, which is responsible for rapid elimination of a second dose of PEGylated liposomes. J Control Release. 2006;112(1):15–25.

130. Semple SC, Harasym TO, Clow KA, Ansell SM, Klimuk SK, Hope MJ. Immunogenicity and Rapid Blood Clearance of Liposomes Containing Polyethylene Glycol-Lipid Conjugates and Nucleic Acid. J Pharmacol Exp Ther. 2005;312(3):1020–6.

131. Garay RP, Labaune JP. Immunogenicity of Polyethylene Glycol (PEG). In The Open Conference Proceedings Journal. 2011;2:104–7.

132. Lila AS, Kiwada H, Ishida T. The accelerated blood clearance (ABC) phenomenon: Clinical challenge and approaches to manage. J Control Release. 2013;172(1):38–47.

133. Chen BM, Su YC, Chang CJ, Burnouf PA, Chuang KH, Chen CH, et al. Measurement of Pre-Existing IgG and IgM Antibodies against Polyethylene Glycol in Healthy Individuals. Anal Chem. 2016;88(21):10661–6.

134. Szebeni J, Muggia F, Gabizon A, Barenholz Y. Activation of complement by therapeutic liposomes and other lipid excipient-based therapeutic products: Prediction and prevention. Adv Drug Deliver Rev. 2011;63(12):1020–30.

135. Szebeni J. Complement activation-related pseudoallergy: A stress reaction in blood triggered by nanomedicines and biologicals. Mol Immunol. 2014;61(2):163–73.

136. Fang Y, Xue J, Gao S, Lu A, Yang D, Jiang H, et al. Cleavable PEGylation: a strategy for overcoming the "PEG dilemma" in efficient drug delivery. Drug Deliv. 2017;24(sup1):22–32.

137. Abrams MT, Koser ML, Seitzer J, Williams SC, DiPietro MA, Wang W, et al. Evaluation of Efficacy, Biodistribution, and Inflammation for a Potent siRNA Nanoparticle: Effect of Dexamethasone Co-treatment. Mol Ther. 2010;18(1):171–80.

138. Barros SA, Gollob JA. Safety profile of RNAi nanomedicines. Adv Drug Deliver Rev. 2012;64(15):1730–7.

139. Knop K, Hoogenboom R, Fischer D, Schubert US. Poly(ethylene glycol) in Drug Delivery: Pros and Cons as Well as Potential Alternatives. Angewandte Chemie Int Ed. 2010;49(36):6288–308.

140. Abbina S, Parambath A. 14 PEGylation and its alternatives A summary. Eng Biomaterials Drug Deliv Syst. 2018;363–76.

141. Gangloff N, Ulbricht J, Lorson T, Schlaad H, Luxenhofer R. Peptoids and Polypeptoids at the Frontier of Supra- and Macromolecular Engineering. Chem Rev. 2016;116(4):1753–802.

142. Secker C, Brosnan SM, Luxenhofer R, Schlaad H. Poly(α-Peptoid)s Revisited: Synthesis, Properties, and Use as Biomaterial. Macromol Biosci. 2015;15(7):881–91.

143. Kidchob T, Kimura S, Imanishi Y. Amphiphilic poly(Ala)-b-poly(Sar) microspheres loaded with hydrophobic drug. J Control Release. 1998;51(2–3):241–8.

144. Birke A, Ling J, Barz M. Polysarcosine-containing copolymers: Synthesis, characterization, self-assembly, and applications. Prog Polym Sci. 2018;81(Metabolism 42 1993):163–208.

145. Zimpel A, Danaf NA, Steinborn B, Kuhn J, Höhn M, Bauer T, et al. Coordinative Binding of Polymers to Metal–Organic Framework Nanoparticles for Control of Interactions at the Biointerface. Acs Nano. 2019;13(4):3884–95.

146. Negwer I, Best A, Schinnerer M, Schäfer O, Capeloa L, Wagner M, et al. Monitoring drug nanocarriers in human blood by near-infrared fluorescence correlation spectroscopy. Nat Commun. 2018;9(1):5306.

147. Stéen EJL, Jørgensen JT, Johann K, Nørregaard K, Sohr B, Svatunek D, et al. Trans -Cyclooctene-Functionalized PeptoBrushes with Improved Reaction Kinetics of the Tetrazine Ligation for Pretargeted Nuclear Imaging. Acs Nano. 2019;14(1):568–84.

148. Weber B, Seidl C, Schwiertz D, Scherer M, Bleher S, Süss R, et al. Polysarcosine-Based Lipids: From Lipopolypeptoid Micelles to Stealth-Like Lipids in Langmuir Blodgett Monolayers. Polymers-basel. 2016;8(12):427.

149. Weber B, Birke A, Fischer K, Schmidt M, Barz M. Solution Properties of Polysarcosine: From Absolute and Relative Molar Mass Determinations to Complement Activation. Macromolecules. 2018;51(7):2653–61.

150. Akinc A, Querbes W, De S, Qin J, Frank-Kamenetsky M, Jayaprakash NK, et al. Targeted Delivery of RNAi Therapeutics With Endogenous and Exogenous Ligand-Based Mechanisms. Mol Ther. 2010;18(7):1357–64.

151. Chen D, Parayath N, Ganesh S, Wang W, Amiji M. The role of apolipoprotein- and vitronectin-enriched protein corona on lipid nanoparticles for in vivo targeted delivery and transfection of oligonucleotides in murine tumor models. Nanoscale. 2019;11(40):18806–24.

152. Chen D, Ganesh S, Wang W, Amiji M. The role of surface chemistry in serum protein corona-mediated cellular delivery and gene silencing with lipid nanoparticles. Nanoscale. 2019;11(18):8760–75.

153. Gilleron J, Querbes W, Zeigerer A, Borodovsky A, Marsico G, Schubert U, et al. Image-based analysis of lipid nanoparticle–mediated siRNA delivery, intracellular trafficking and endosomal escape. Nat Biotechnol. 2013;31(7):638–46.

154. Sahay G, Querbes W, Alabi C, Eltoukhy A, Sarkar S, Zurenko C, et al. Efficiency of siRNA delivery by lipid nanoparticles is limited by endocytic recycling. Nat Biotechnol. 2013;31(7):653–8.

155. Bhattacharya S, Mandal SS. Evidence of Interlipidic Ion-Pairing in Anion-Induced DNA Release from Cationic Amphiphile−DNA Complexes. Mechanistic Implications in Transfection †. Biochemistry-us. 1998;37(21):7764–77.

156. Arteta M, Kjellman T, Bartesaghi S, Wallin S, Wu X, Kvist AJ, et al. Successful reprogramming of cellular protein production through mRNA delivered by functionalized lipid nanoparticles. Proc National Acad Sci. 2018;115(15):201720542.

157. Wang H, Tam YYC, Chen S, Zaifman J, Meel R van der, Ciufolini MA, et al. The Niemann-Pick C1 Inhibitor NP3.47 Enhances Gene Silencing Potency of Lipid Nanoparticles Containing siRNA. Mol Ther. 2016;24(12):2100–8.

158. Lorenzer C, Dirin M, Winkler AM, Baumann V, Winkler J. Going beyond the liver: Progress and challenges of targeted delivery of siRNA therapeutics. J Control Release. 2015;203:1–15.

159. Whitehead KA, Dorkin RJ, Vegas AJ, Chang PH, Veiseh O, Matthews J, et al. Degradable lipid nanoparticles with predictable in vivo siRNA delivery activity. Nat Commun. 2014;5(1):4277.

160. Ramishetti S, Hazan-Halevy I, Palakuri R, Chatterjee S, Gonna SN, Dammes N, et al. A Combinatorial Library of Lipid Nanoparticles for RNA Delivery to Leukocytes. Adv Mater. 2020;32(12):1906128.

161. Arvizo RR, Miranda OR, Moyano DF, Walden CA, Giri K, Bhattacharya R, et al. Modulating Pharmacokinetics, Tumor Uptake and Biodistribution by Engineered Nanoparticles. Plos One. 2011;6(9):e24374.

162. Harashima H, Kiwada H. Liposomal targeting and drug delivery: kinetic consideration. Adv Drug Deliver Rev. 1996;19(3):425–44.

163. Chen S, Tam YC, Lin P, Leung A, Tam YK, Cullis PR. Development of lipid nanoparticle formulations of siRNA for hepatocyte gene silencing following subcutaneous administration. J Control Release. 2014;196(Pharmaceutics 5 2013):106–12.

164. Reichmuth AM, Oberli MA, Jaklenec A, Langer R, Blankschtein D. mRNA vaccine delivery using lipid nanoparticles. Ther Deliv. 2016;7(5):319–34.

165. Ryals RC, Patel S, Acosta C, McKinney M, Pennesi ME, Sahay G. The effects of PEGylation on LNP based mRNA delivery to the eye. Plos One. 2020;15(10):e0241006.

166. Lokugamage MP, Vanover D, Beyersdorf J, Hatit MZC, Rotolo L, Echeverri ES, et al. Optimization of lipid nanoparticles for the delivery of nebulized therapeutic mRNA to the lungs. Nat Biomed Eng. 2021;5(9):1059–68.

167. Rungta RL, Choi HB, Lin PJ, Ko RW, Ashby D, Nair J, et al. Lipid Nanoparticle Delivery of siRNA to Silence Neuronal Gene Expression in the Brain. Mol Ther Nucleic Acids. 2013;2(12):e136.

168. Rosenblum D, Joshi N, Tao W, Karp JM, Peer D. Progress and challenges towards targeted delivery of cancer therapeutics. Nat Commun. 2018;9(1):1410.

169. Marcos-Contreras OA, Greineder CF, Kiseleva R, Parhiz H, Walsh LR, Zuluaga-Ramirez V, et al. Selective targeting of nanomedicine to inflamed cerebral vasculature to enhance the blood–brain barrier. Proc National Acad Sci. 2020;201912012.

170. Salvati A, Pitek AS, Monopoli MP, Prapainop K, Bombelli F, Hristov DR, et al. Transferrin-functionalized nanoparticles lose their targeting capabilities when a biomolecule corona adsorbs on the surface. Nat Nanotechnol. 2013;8(2):137–43.

171. Brown BD, Venneri MA, Zingale A, Sergi LS, Naldini L. Endogenous microRNA regulation suppresses transgene expression in hematopoietic lineages and enables stable gene transfer. Nat Med. 2006;12(5):585–91.

172. Suhr OB, Coelho T, Buades J, Pouget J, Conceicao I, Berk J, et al. Efficacy and safety of patisiran for familial amyloidotic polyneuropathy: a phase II multi-dose study. Orphanet J Rare Dis. 2015;10(1):109.

173. Solomon SD, Adams D, Kristen A, Grogan M, González-Duarte A, Maurer MS, et al. Effects of Patisiran, an RNA Interference Therapeutic, on Cardiac Parameters in Patients With Hereditary Transthyretin-Mediated Amyloidosis. Circulation. 2019;139(4):431–43.

174. Kuhn AN, Diken M, Kreiter S, Selmi A, Kowalska J, Jemielity J, et al. Phosphorothioate cap analogs increase stability and translational efficiency of RNA vaccines in immature dendritic cells and induce superior immune responses in vivo. Gene Ther. 2010;17(8):961–71.

175. Kreiter S, Konrad T, Sester M, Huber C, Türeci Ö, Sahin U. Simultaneous ex vivo quantification of antigen-specific CD4+ and CD8+ T cell responses using in vitro transcribed RNA. Cancer Immunol Immunother. 2007;56(10):1577–87.

176. Vogel AB, Lambert L, Kinnear E, Busse D, Erbar S, Reuter KC, et al. Self-Amplifying RNA Vaccines Give Equivalent Protection against Influenza to mRNA Vaccines but at Much Lower Doses. Mol Ther. 2018;26(2):446–55.

177. Batzri S, Korn ED. Single bilayer liposomes prepared without sonication. Biochimica Et Biophysica Acta Bba - Biomembr. 1973;298(4):1015–9.

178. Koppel DE. Analysis of Macromolecular Polydispersity in Intensity Correlation Spectroscopy: The Method of Cumulants. J Chem Phys. 1972;57(11):4814–20.

179. Eastman SJ, Hope MJ, Cullis PR. Transbilayer transport of phosphatidic acid in response to transmembrane pH gradients. Biochemistry-us. 1991;30(7):1740–5.

180. Zhang J, Fan H, Levorse DA, Crocker LS. Ionization Behavior of Amino Lipids for siRNA Delivery: Determination of Ionization Constants, SAR, and the Impact of Lipid p K a on Cationic Lipid−Biomembrane Interactions. Langmuir. 2011;27(5):1907–14.

181. Alabi CA, Love KT, Sahay G, Yin H, Luly KM, Langer R, et al. Multiparametric approach for the evaluation of lipid nanoparticles for siRNA delivery. Proc National Acad Sci. 2013;110(32):12881–6.

182. Ciccariello S, Goodisman J, Brumberger H. On the Porod law. J Appl Crystallogr. 1988;21(2):117–28.

183. Seddon JM, Cevc G. Lipid Polymorphism:Lipid Polymorphism Structure and Stability of Lyotropic Mesophases of Phospholipids. In: 1st Edition. 1993.

184. Goodby JW, Tschierske C, Gleeson H, Kato T, Raynes P, Collings PJ. Handbook of Liquid Crystals. 2014.

185. Blanchet CE, Spilotros A, Schwemmer F, Graewert MA, Kikhney A, Jeffries CM, et al. Versatile sample environments and automation for biological solution X-ray scattering experiments at the P12 beamline (PETRA III, DESY). J Appl Crystallogr. 2015;48(2):431–43.

186. Franke D, Kikhney AG, Svergun DI. Automated acquisition and analysis of small angle X-ray scattering data. Nucl Instruments Methods Phys Res Sect Accel Spectrometers Detect Assoc Equip. 2012;689:52–9.

187. Johnston G. Automated handheld instrument improves counting precision across multiple cell lines. 2010;48(4):325–7.

188. Alam J, Cook JL. Reporter genes: Application to the study of mammalian gene transcription. Anal Biochem. 1990;188(2):245–54.

189. Wet JR de, Wood KV, DeLuca M, Helinski DR, Subramani S. Firefly luciferase gene: structure and expression in mammalian cells. Mol Cell Biol. 1987;7(2):725–37.

190. Evans WH, Hardison WG. Phospholipid, cholesterol, polypeptide and glycoprotein composition of hepatic endosome subfractions. Biochem J. 1985;232(1):33–6.

191. Coch C, Lück C, Schwickart A, Putschli B, Renn M, Höller T, et al. A Human In Vitro Whole Blood Assay to Predict the Systemic Cytokine Response to Therapeutic Oligonucleotides Including siRNA. Plos One. 2013;8(8):e71057.

192. Dobrovolskaia MA, McNeil SE. Understanding the correlation between in vitro and in vivo immunotoxicity tests for nanomedicines. J Control Release. 2013;172(2):456–66.

193. Shah K. Current advances in molecular imaging of gene and cell therapy for cancer. Cancer Biol Ther. 2005;4(5):518–23.

194. Zhang Y, Wang L, Dey S, Alnaeeli M, Suresh S, Rogers H, et al. Erythropoietin Action in Stress Response, Tissue Maintenance and Metabolism. Int J Mol Sci. 2014;15(6):10296–333.

195. Leung AK, Tam YC, Chen S, Hafez IM, Cullis PR. Microfluidic Mixing: A General Method for Encapsulating Macromolecules in Lipid Nanoparticle Systems. J Phys Chem B. 2015;119(28):8698–706.

196. Kumar V, Qin J, Jiang Y, Duncan RG, Brigham B, Fishman S, et al. Shielding of Lipid Nanoparticles for siRNA Delivery: Impact on Physicochemical Properties, Cytokine Induction, and Efficacy. Mol Ther - Nucleic Acids. 2014;3(N Engl J Med 369 2013):e210.

197. Ishida T, Kiwada H. Accelerated blood clearance (ABC) phenomenon upon repeated injection of PEGylated liposomes. Int J Pharmaceut. 2008;354(1–2):56–62.

198. Kranz LM, Diken M, Haas H, Kreiter S, Loquai C, Reuter KC, et al. Systemic RNA delivery to dendritic cells exploits antiviral defence for cancer immunotherapy. Nature. 2016;534(7607):396–401.

199. Bleher S, Buck J, Muhl C, Sieber S, Barnert S, Witzigmann D, et al. Poly(Sarcosine) Surface Modification Imparts Stealth-Like Properties to Liposomes. Small. 2019;15(50):1904716.

200. Fenaroli F, Repnik U, Xu Y, Johann K, Herck SV, Dey P, et al. Enhanced Permeability and Retention-like Extravasation of Nanoparticles from the Vasculature into Tuberculosis Granulomas in Zebrafish and Mouse Models. Acs Nano. 2018;12(8):8646–61.

201. Maurer PH, Subrahmanyam D, Katchalski E, Blout ER. Antigenicity of Polypeptides (Poly Alpha Amino Acids). J Immunol. 1959;(83):193–7.

202. Besin G, Milton J, Sabnis S, Howell R, Mihai C, Burke K, et al. Accelerated Blood Clearance of Lipid Nanoparticles Entails a Biphasic Humoral Response of B-1 Followed by B-2 Lymphocytes to Distinct Antigenic Moieties. Immunohorizons. 2019;3(7):282–93.

203. Xu Y, Hui SW, Frederik P, Szoka FC. Physicochemical Characterization and Purification of Cationic Lipoplexes. Biophys J. 1999;77(1):341–53.

204. Salditt T, Koltover I, Rädler JO, Safinya CR. Two-Dimensional Smectic Ordering of Linear DNA Chains in Self-Assembled DNA-Cationic Liposome Mixtures. Phys Rev Lett. 1997;79(13):2582–5.

205. Koltover I, Salditt T, Safinya CR. Phase Diagram, Stability, and Overcharging of Lamellar Cationic Lipid–DNA Self-Assembled Complexes. Biophys J. 1999;77(2):915–24.

206. Rädler JO, Koltover I, Salditt T, Safinya CR. Structure of DNA-Cationic Liposome Complexes: DNA Intercalation in Multilamellar Membranes in Distinct Interhelical Packing Regimes. Science. 1997;275(5301):810–4.

207. Balbino TA, Gasperini AAM, Oliveira CLP, Azzoni AR, Cavalcanti LP, Torre LG de L. Correlation of the Physicochemical and Structural Properties of pDNA/Cationic Liposome Complexes with Their in Vitro Transfection. Langmuir. 2012;28(31):11535–45.

208. Majzoub RN, Ewert KK, Safinya CR. Cationic liposome–nucleic acid nanoparticle assemblies with applications in gene delivery and gene silencing. Philosophical Transactions Royal Soc Math Phys Eng Sci. 2016;374(2072):20150129.

209. Ziller A, Nogueira SS, Hühn E, Funari SS, Brezesinski G, Hartmann H, et al. Incorporation of mRNA in Lamellar Lipid Matrices for Parenteral Administration. Mol Pharmaceut. 2018;15(2):642–51.

210. Safinya CR. Structures of lipid–DNA complexes: supramolecular assembly and gene delivery. Curr Opin Struc Biol. 2001;11(4):440–8.

211. Leung AKK, Hafez IM, Baoukina S, Belliveau NM, Zhigaltsev IV, Afshinmanesh E, et al. Lipid Nanoparticles Containing siRNA Synthesized by Microfluidic Mixing Exhibit an Electron-Dense Nanostructured Core. J Phys Chem C Nanomater Interfaces. 2012;116(34):18440–50.

212. Hassett KJ, Higgins J, Woods A, Levy B, Xia Y, Hsiao CJ, et al. Impact of lipid nanoparticle size on mRNA vaccine immunogenicity. J Control Release. 2021;335:237–46.

213. Sago CD, Krupczak BR, Lokugamage MP, Gan Z, Dahlman JE. Cell Subtypes Within the Liver Microenvironment Differentially Interact with Lipid Nanoparticles. Cell Mol Bioeng. 2019;12(5):1–9.

214. Sago CD, Lokugamage MP, Paunovska K, Vanover DA, Monaco CM, Shah NN, et al. High-throughput in vivo screen of functional mRNA delivery identifies nanoparticles for endothelial cell gene editing. Proc National Acad Sci. 2018;115(42):201811276.

215. Cui L, Hunter MR, Sonzini S, Pereira S, Romanelli SM, Liu K, et al. Mechanistic Studies of an Automated Lipid Nanoparticle Reveal Critical Pharmaceutical Properties Associated with Enhanced mRNA Functional Delivery In Vitro and In Vivo. Small. 2022;18(9):2105832.

216. Carrasco MJ, Alishetty S, Alameh MG, Said H, Wright L, Paige M, et al. Ionization and structural properties of mRNA lipid nanoparticles influence expression in intramuscular and intravascular administration. Commun Biology. 2021;4(1):956.

217. Patel P, Ibrahim NM, Cheng K. The Importance of Apparent pKa in the Development of Nanoparticles Encapsulating siRNA and mRNA. Trends Pharmacol Sci. 2021;

218. Sato Y, Hashiba K, Sasaki K, Maeki M, Tokeshi M, Harashima H. Understanding structure-activity relationships of pH-sensitive cationic lipids facilitates the rational identification of promising lipid nanoparticles for delivering siRNAs in vivo. J Control Release. 2019;(Nature 411 2001).

219. Zhao X, Glass Z, Chen J, Yang L, Kaplan DL, Xu Q. mRNA Delivery Using Bioreducible Lipidoid Nanoparticles Facilitates Neural Differentiation of Human Mesenchymal Stem Cells. Adv Healthc Mater. 2021;10(4):2000938.

220. Zhao X, Chen J, Qiu M, Li Y, Glass Z, Xu Q. Imidazole-Based Synthetic Lipidoids for In Vivo mRNA Delivery into Primary T Lymphocytes. Angewandte Chemie Int Ed. 2020;59(45):20083–9.

221. Hong S, Choi DW, Kim HN, Park CG, Lee W, Park HH. Protein-Based Nanoparticles as Drug Delivery Systems. Pharm. 2020;12(7):604.

222. Green MR, Manikhas GM, Orlov S, Afanasyev B, Makhson AM, Bhar P, et al. Abraxane®, a novel Cremophor®-free, albumin-bound particle form of paclitaxel for the treatment of advanced non-small-cell lung cancer. Ann Oncol. 2006;17(8):1263–8.

223. Kim C, Hara E, Watabe N, Hara I, Kimura S. Modulation of immunogenicity of poly(sarcosine) displayed on various nanoparticle surfaces due to different physical properties. J Pept Sci. 2017;23(12):889–98.

224. Sakurai Y, Mizumura W, Ito K, Iwasaki K, Katoh T, Goto Y, et al. Improved Stability of siRNA-Loaded Lipid Nanoparticles Prepared with a PEG-Monoacyl Fatty Acid Facilitates Ligand-Mediated siRNA Delivery. Molecular Pharmaceutics. 2020;

225. Kauffman KJ, Mir FF, Jhunjhunwala S, Kaczmarek JC, Hurtado JE, Yang JH, et al. Efficacy and immunogenicity of unmodified and pseudouridine-modified mRNA delivered systemically with lipid nanoparticles in vivo. Biomaterials. 2016;109:78–87.

226. Samaridou E, Heyes J, Lutwyche P. Lipid nanoparticles for nucleic acid delivery: Current perspectives. Adv Drug Deliver Rev. 2020;154–155:37–63.

227. Blakney AK, McKay PF, Yus B, Aldon Y, Shattock RJ. Inside out: optimization of lipid nanoparticle formulations for exterior complexation and in vivo delivery of saRNA. Gene Ther. 2019;1–10.

228. Blakney AK, McKay PF, Yus B, Hunter JE, Dex EA, Shattock RJ. The Skin You Are In: Design-of-Experiments Optimization of Lipid Nanoparticle Self-Amplifying RNA Formulations in Human Skin Explants. Acs Nano. 2019;13(5):5920–30.

229. Lou G, Anderluzzi G, Schmidt ST, Woods S, Gallorini S, Brazzoli M, et al. Delivery of self-amplifying mRNA vaccines by cationic lipid nanoparticles: The impact of cationic lipid selection. J Control Release. 2020;325:370–9.

230. Brito LA, Chan M, Shaw CA, Hekele A, Carsillo T, Schaefer M, et al. A Cationic Nanoemulsion for the Delivery of Next-generation RNA Vaccines. Mol Ther. 2014;22(12):2118–29.

231. Pollard C, Rejman J, Haes WD, Verrier B, Gulck EV, Naessens T, et al. Type I IFN Counteracts the Induction of Antigen-Specific Immune Responses by Lipid-Based Delivery of mRNA Vaccines. Mol Ther. 2013;21(1):251–9.

232. Schmidt ST, Foged C, Korsholm KS, Rades T, Christensen D. Liposome-Based Adjuvants for Subunit Vaccines: Formulation Strategies for Subunit Antigens and Immunostimulators. Pharm. 2016;8(1):7.

233. Kaczmarek JC, Kauffman KJ, Fenton OS, Sadtler K, Patel AK, Heartlein MW, et al. Optimization of a Degradable Polymer–Lipid Nanoparticle for Potent Systemic Delivery of mRNA to the Lung Endothelium and Immune Cells. Nano Lett. 2018;18(10):6449–54.

234. Kim J, Jozic A, Sahay G. Naturally Derived Membrane Lipids Impact Nanoparticle-Based Messenger RNA Delivery. Cell Mol Bioeng. 2020;13(5):463–74.

235. Dahlman JE, Kauffman KJ, Xing Y, Shaw TE, Mir FF, Dlott CC, et al. Barcoded nanoparticles for high throughput in vivo discovery of targeted therapeutics. Proc National Acad Sci. 2017;114(8):2060–5.

236. Wu Q, Liu J, Wang X, Feng L, Wu J, Zhu X, et al. Organ-on-a-chip: recent breakthroughs and future prospects. Biomed Eng Online. 2020;19(1):9.

237. Wang W, Feng S, Ye Z, Gao H, Lin J, Ouyang D. Prediction of lipid nanoparticles for mRNA vaccines by the machine learning algorithm. Acta Pharm Sinica B. 2021;

238. Hassanzadeh P, Atyabi F, Dinarvand R. The significance of artificial intelligence in drug delivery system design. Adv Drug Deliver Rev. 2019;151:169–90.

239. Zhao P, Hou X, Yan J, Du S, Xue Y, Li W, et al. Long-term storage of lipid-like nanoparticles for mRNA delivery. Bioact Mater. 2020;5(2):358–63.

240. Zhang H, You X, Wang X, Cui L, Wang Z, Xu F, et al. Delivery of mRNA vaccine with a lipid-like material potentiates antitumor efficacy through Toll-like receptor 4 signaling. Proc National Acad Sci. 2021;118(6):e2005191118.

241. Meel R, Chen S, Zaifman J, Kulkarni JA, Zhang XRS, Tam YK, et al. Modular Lipid Nanoparticle Platform Technology for siRNA and Lipophilic Prodrug Delivery. Small. 2021;17(37):2103025.

SUPPORTING INFORMATION

Table S 1. Summary of physicochemical characterization of LNP manufactured at varied N/P.

N/P ratio	Particle size	PdI	Encapsulation efficiency [%]	Unbound mRNA [%]
0.3	106.3 ± 1.1	0.191	2.06 ± 2	81 ± 1
0.7	122.9 ± 1.0	0.183	20.6 ± 1	72.8 ± 3
1	135.3 ± 0.4	0.225	32.3 ± 6	45.9 ± 8
1.3	125.5 ± 0.4	0.176	33.2 ± 2	31.4 ± 2
1.7	100.4 ± 0.4	0.149	40.2 ± 7	10.1 ± 0
2	94.8 ± 0.5	0.154	46.6 ± 8	4.7 ± 0
2.3	91 ± 0.3	0.164	51.1 ± 4	2.5 ± 0
2.7	82.2 ± 0.3	0.101	56.1 ± 3	0 ± 0
3	80.9 ± 0.2	0.129	76.0 ± 4	0 ± 0
4	72.6 ± 0.3	0.104	88.4 ± 2	0 ± 0
6	68 ± 0.1	0.16	92.6 ± 0	0 ± 0

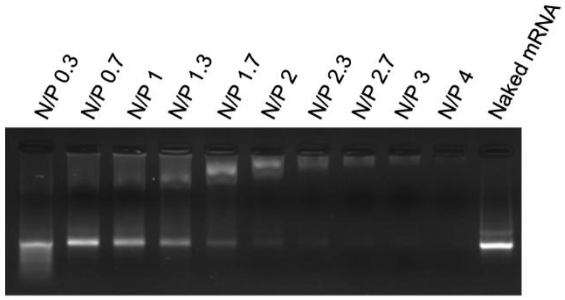

Figure S 1. Determination of unbound RNA as function of N/P ratio by the agarose gel electrophoresis.
LNP composed of DODMA, Chol, DOPE, PEG cerC16 at a respective 40/ 48/ 10/ 2 molar composition were formulated by microfluidic mixing at increasing N/P ratio. Formulations and control naked mRNA were loaded into a 1 % of agarose gel. Only at lower N/P ratios a clearer free mRNA band can be observed, indicating that above N/P 2.7 all mRNA is bounded to lipids/particles.

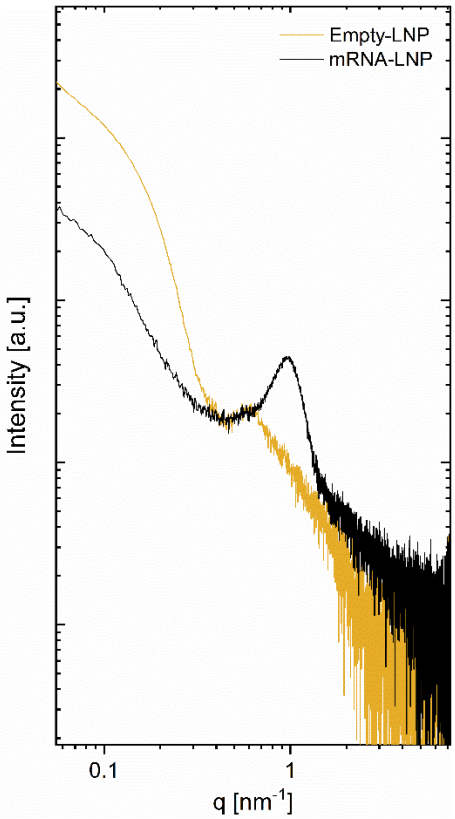

Figure S 2. Small angle X-Ray scattering data of mRNA-loaded and empty LNP.
LNP composed of DODMA, Chol, DOPE, PEG cerC16 at a respective 40/ 48/10/2 molar composition was formulated by microfluidic mixing in presence or absence of mRNA. The N/P ratio was 4.

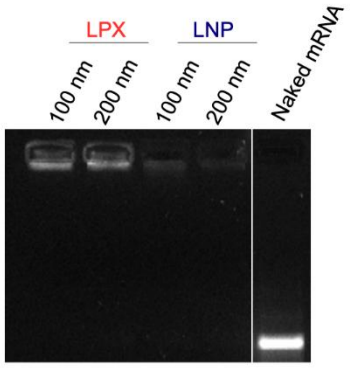

Figure S 3. Determination of unbound RNA of LPX and LNP by the agarose gel electrophoresis.
Identically composed LPX and LNP, and naked mRNA were loaded into a 1 % of agarose gel. No free mRNA in solution can be detected by agarose gel, suggesting that all mRNA is bounded to the lipids independently of manufacturing procedure.

Table S 2. Quantitative analysis of the peak of LPX and LNP as a function of particle size.

Nanocomplexes	Peak position [xc]	Peak width [w]	Area [A]	d-spacing [nm]	Corr. [nm]	Length
100nm-LNP	0.974	0.373	1214.5	6.451	5.362	
200nm-LNP	-	-	-	-	-	
100nm-LPX	0.937	0.577	1098.62	6.706	3.466	
200nm-LPX	0.928	0.298	1334.71	6.771	6.771	

Table S 3. Physicochemical characteristics of EPO LNP and LPX

Nanocomplexes	Particle Size (nm)	PdI	mRNA accessibility (%)	Unbound mRNA
100nm-LNP	81.85	0.166	10.5	n.d.
200nm-LNP	219.8	0.142	32.8	n.d.
100nm-LPX	126.25	0.1725	44.3	n.d.
200nm-LPX	204.55	0.166	55.0	n.d.

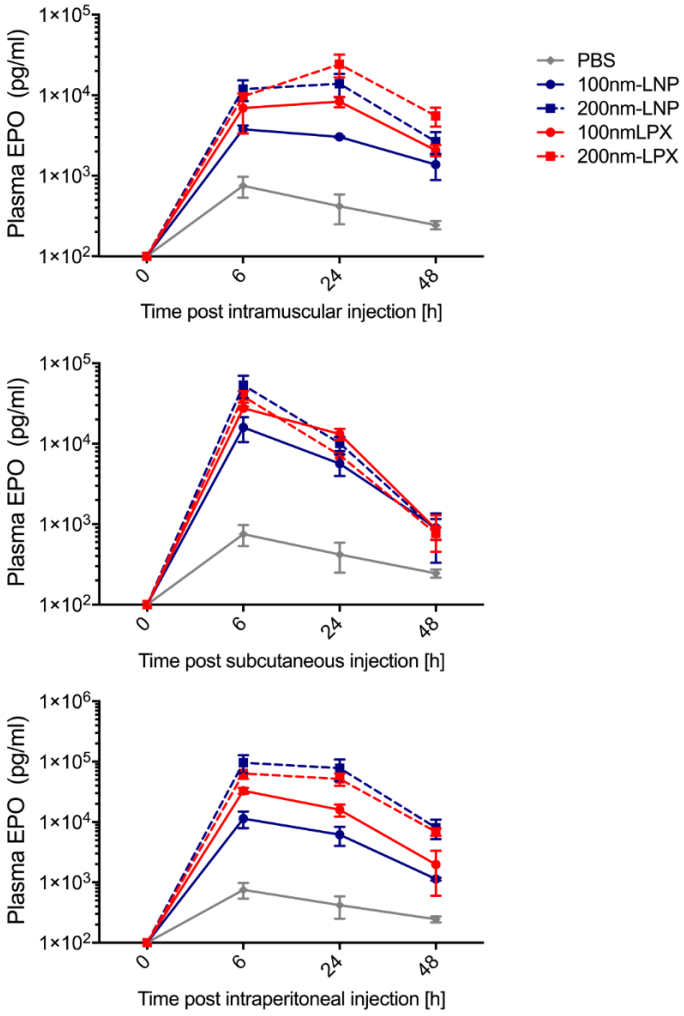

Figure S 4. EPO profile of LNP as LPX nanoformulations after IM, SC, and IP administration.
EPO mRNA-complexes were administrated at mRNA concentration of 2.5, 1, and 3 µg for IM, IP and SC injection, respectively, into Balb/C mice (n=3 per group). Data are presented as mean ± SD. These results suggested that 200 nm vehicles mediated higher and prolonged protein expression in different administration routes.

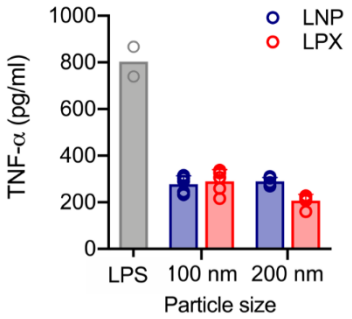

***Figure S 5. Production of proinflammatory cytokine activation by macrophages cell line after lipid nanoparticle exposure*.**
Macrophages were incubated for 24 h at 37 °C with LNP samples and LPS (100 ng/ml). IL-6 and TNF-α were quantified in culture supernatants by ELISA. IL-6 values were not detectable. Each bar represents mean ± SD of independent experiments performed at least in duplicate. These results indicated that increased nanoparticles sizes did not lead to enhanced production of proinflammatory cytokines.

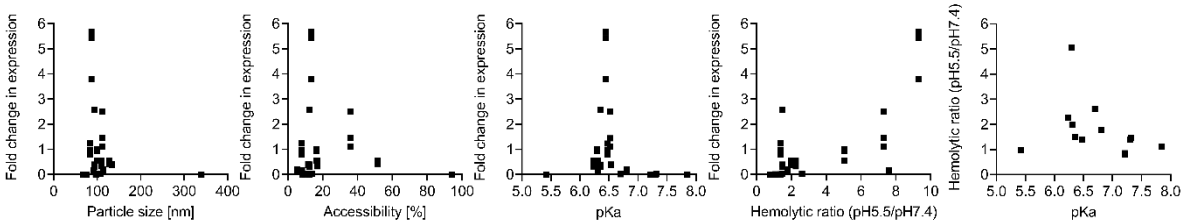

Figure S 6. Structure-activity correlations of mRNA-LNP.

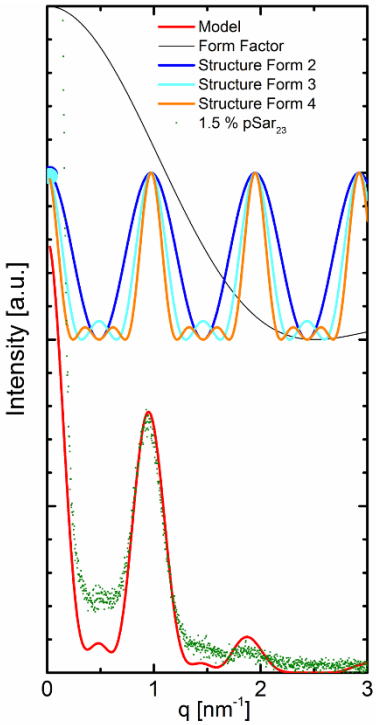

Figure S 7. Simulation and experimental data in linear scale.
Coloured curves on top show structure factors for a repeat distance of 6.45 nm with for 2 (blue), 3 (light blue) and 4 (orange) repeat units according to Equation 8. For clarity, data is scaled to the same maximum

values. The upper black curve shows a form factor resulting from a uniform scatterer of 2.5 nm length according to Equation 7. For the red curve, the form factors for 2 and 3 units were averaged without weighing and multiplied by the structure factor. The green dotted data represents the measurement of the LNP formulated with 1.5% $pSar_{23}$. Several key aspects of the experimental curve shape, e.g., peak position and width, are qualitatively represented by this simplified simulation.

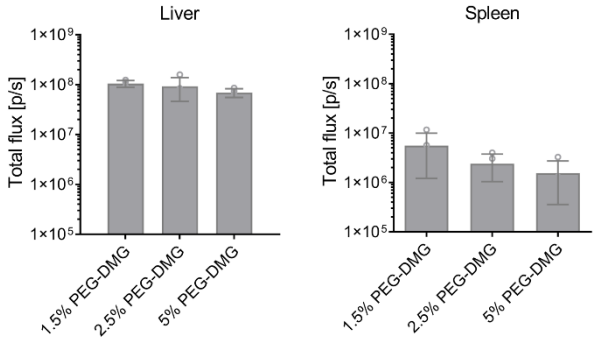

Figure S 8. Luciferase expression upon IV injection of PEG-DMG LNP.
Transfection in Balb/C mice treated with a luciferase mRNA dose of 10 µg administered through an intravenous injection of pSar and PEG LNP containing DODMA as the ionizable lipid. Luciferase expression in the liver and spleen 6 h post-injection is reported as the mean of total flux (p/s) ± standard deviation, for n=3. Increasing molar fractions of PEG lipid resulted in similar in vivo expression.

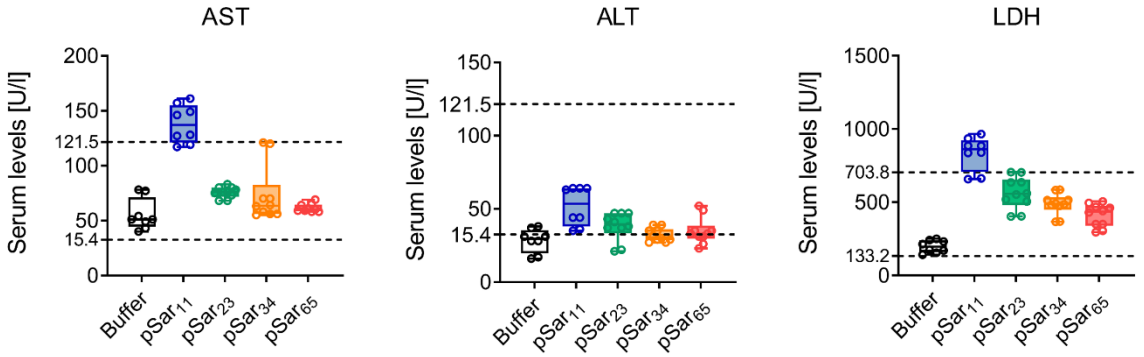

Figure S 9. ***Effect of pSar chain length on liver enzyme release profile.***
AST, ALT and, LDH concentrations were measured 6 h post-injection of 10 µg of luciferase encoding-mRNA formulated in LNP (DODMA) with 5 mol % pSar lipid with different chain length as indicated. Vehicle buffer (PBS) was used as control. Box plots show data as a mean ± standard deviation, for n=3. These results showed that upon administration of pSar LNP, the enzymes levels are within the reference values obtained from several healthy mice (dot line). Only pSar11 resulted in slightly higher liver enzyme values than the control groups**.**

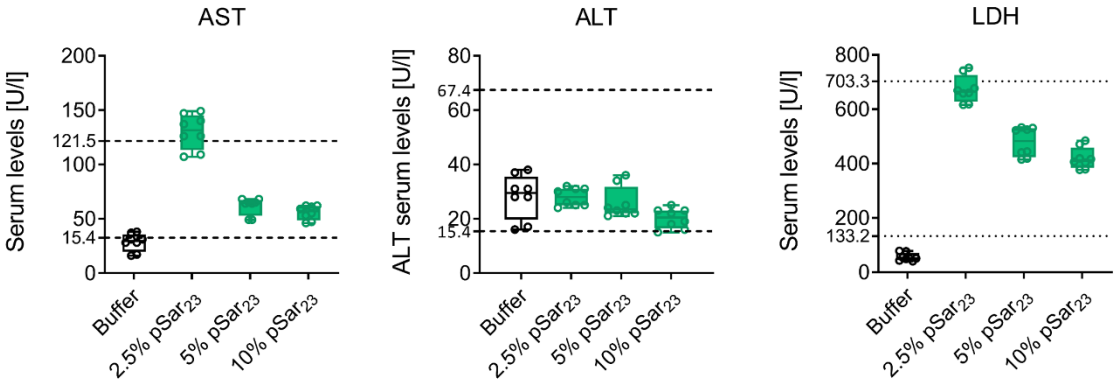

Figure S 10. Effect of pSar molar faction on liver enzyme release profile.
AST, ALT, LDH concentrations were measured 6 h post-injection of 10 µg of luciferase encoding-mRNA formulated within pSar-LNP containing DODMA as the ionizable lipid. pSar23-LNP was intravenously administered with increased molar fraction (2.5-10%). Vehicle buffer (PBS) was used as control. Box plots show data as a mean with ± standard deviation, for n=3. These results showed that upon administration of pSar LNP with varied molar fraction, the enzymes levels are within the reference values obtained from several healthy mice (dot line). Only in the case of 2.5 % of pSar23 mediated delivery slightly higher AST values were observed compared to healthy mice.

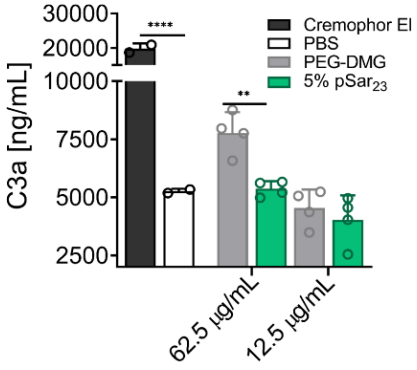

Figure S 11. Concentrations of C3a post incubation of pSar23 and PEG LNP with human serum.
DODMA was used as the ionizable lipid for both LNP formulations. Data was taken 1 hour post-incubation at 37°C. LNP concentrations were calculated as the nanoparticle theoretical plasma concentration, which derives from the ratio between the human dose and the human blood volume. The tested concnetrations were based on a human dose of 1 mg/kg, the theoretical plasma concentration (i.e., the in vitro testing concentration) is equivalent to an mRNA concentration of 12.5 µg/mL, with the 5 times higher concentration being equivalent to 62.5 µg/ml. Vehicle buffer (PBS) and Cremophor El were used as negative and positive control, respectively. Data is shown as mean ± standard deviation, n=2-3. Statistical significance was calculated with one-way ANOVA with multiple comparisons (* p< 0.05; ** p<0.01; *** p<0.001). LNP containing 5 % $pSar_{23}$ induced lower C3a levels when compared to PEG-DMG at high dose (62.5 µg/ml). This finding suggested that pSar LNP are likely less toxic than PEG LNP.

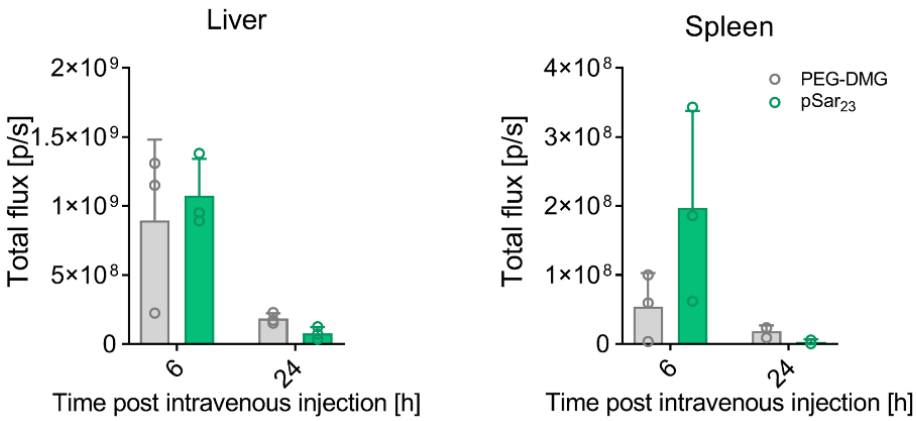

Figure S 12. Luciferase expression upon IV injection of pSar and PEG LNP.
Transfection in Balb/C mice treated with a luciferase mRNA dose of 10 µg administered through an intravenous injection of pSar and PEG a LNP containing DPL14 as the ionizable lipid. Luciferase expression in the liver and spleen 6 h post-injection is reported as the mean of total flux (p/s) ± standard deviation, for n=3. Increasing molar fractions of PEG lipid resulted in similar in vivo expression. The trend for a slight decrease in *in vivo* performance in the spleen is not significant.

Table S 4. Summary of LNP formulations and physicochemical properties.

Lipid Composition	Molar Composition [mol %]	Cationic lipid [mg]	Helper lipid [mg]	Chol [mg]	Stealth lipid [mg]	mRNA [mg]	N/P	Weight/weight ratio (ww)	Particle size [dm]	SD	PdI	mRNA accessibility [%]	SD
DODMA:Chol:DSPC:pSar$_{11}$	40:48.5:10:1.5	0.84	0.27	0.63	0.05	0.113	4	15.9				70.4	4.7
DODMA:Chol:DSPC: pSar$_{11}$	40:47.5:10:2.5	0.84	0.27	0.62	0.08	0.113	4	16.7	237.6	-	0.095	67.8	3.9
DODMA:Chol:DSPC: pSar$_{11}$	40:45:10:5	0.84	0.27	0.59	0.17	0.113	4	16.5	134.3	9.8	0.251	74.2	2.7
DODMA:Chol:DSPC: pSar$_{11}$	40:42.5:10:7.5	0.84	0.27	0.55	0.25	0.113	4	17.0	131.2	0.2	0.218	76.7	4.4
DODMA:Chol:DSPC: pSar$_{11}$	40:45:10:10	0.84	0.27	0.52	0.34	0.113	4	17.4	127.0	26.9	0.257	79.5	1.8
DODMA:Chol:DSPC:pSar$_{23}$	40:48.5:10:1.5	0.84	0.27	0.63	0.09	0.113	4	16.2	243.8	104.9	0.256	69.9	6.7
DODMA:Chol:DSPC: pSar$_{23}$	40:47.5:10:2.5	0.84	0.27	0.62	0.16	0.113	4	16.7	134.9	27.5	0.242	74.3	5.6
DODMA:Chol:DSPC: pSar$_{23}$	40:45:10:5	0.84	0.27	0.59	0.31	0.113	4	17.8	88.2	12.0	0.165	77.8	5.2
DODMA:Chol:DSPC: pSar$_{23}$	40:42.5:10:7.5	0.84	0.27	0.55	0.47	0.113	4	18.9	80.5	15.8	0.213	78.8	6.9
DODMA:Chol:DSPC: pSar$_{23}$	40:45:10:10	0.84	0.27	0.52	0.62	0.113	4	20.0	75.2	10.1	0.192	81.7	1.9
DODMA:Chol:DSPC:pSar$_{34}$	40:48.5:10:1.5	0.84	0.27	0.63	0.13	0.113	4	16.6	159.0	59.5	0.272	74.5	10.0
DODMA:Chol:DSPC: pSar$_{34}$	40:47.5:10:2.5	0.84	0.27	0.62	0.22	0.113	4	17.3	161.5	18.7	0.216	74.0	10.3
DODMA:Chol:DSPC: pSar$_{34}$	40:45:10:5	0.84	0.27	0.59	0.44	0.113	4	19.0	92.1	15.6	0.202	83.1	2.5
DODMA:Chol:DSPC: pSar$_{34}$	40:42.5:10:7.5	0.84	0.27	0.55	0.67	0.113	4	20.6	86.6	4.8	0.199	84.8	4.1
DODMA:Chol:DSPC: pSar$_{34}$	40:45:10:10	0.84	0.27	0.52	0.89	0.113	4	22.3	65.9	7.5	0.187	85.1	4.5
DODMA:Chol:DSPC:pSar65	40:48.5:10:1.5	0.84	0.27	0.63	0.24	0.113	4	17.6	145.8	21.3	0.244	73.1	11.2
DODMA:Chol:DSPC:pSar65	40:47.5:10:2.5	0.84	0.27	0.62	0.41	0.113	4	18.9	106.0	15.3	0.283	77.8	7.4
DODMA:Chol:DSPC:pSar65	40:45:10:5	0.84	0.27	0.59	0.82	0.113	4	22.3	91.4	27.9	0.246	88.8	0.5
DODMA:Chol:DSPC:pSar65	40:42.5:10:7.5	0.84	0.27	0.55	1.22	0.113	4	25.6	84.7	28.1	0.231	90.7	0.4
DODMA:Chol:DSPC:pSar65	40:45:10:10	0.84	0.27	0.52	1.63	0.113	4	28.9	70.8	24.2	0.194	85.1	10.2
DODMA:Chol:DSPC:PEG-DMG	40:48.5:10:1.5	0.84	0.27	0.63	0.13	0.113	4	16.5	90.1	2.4	0.111	7.1	0.3
DODMA:Chol:DSPC:PEG-DMG	40:47.5:10:2.5	0.84	0.27	0.62	0.21	0.113	4	17.2	67.6	0.8	0.135	6.2	0.2
DODMA:Chol:DSPC:PEG-DMG	40:45:10:5	0.84	0.27	0.59	0.42	0.113	4	18.7	54.6	0.6	0.133	24.5	0.2
DODMA:Chol:DSPC:PEG-DMG	40:42.5:10:7.5	0.84	0.27	0.55	0.63	0.113	4	20.3	51.4	0.8	0.217	47.2	1.1
DODMA:Chol:DSPC:PEG-DMG	40:45:10:10	0.84	0.27	0.52	0.83	0.113	4	21.9	56.7	1.0	0.374	58.5	0.6

Table S 5. Quantitative analysis of the peak as a function of pSar and PEG-DMG molar fraction.

Lipid	Molar fraction [%]	Peak analysis														
		Position1 [x_c]	σ	Position2 [x_c]	σ	Width1 [w]	σ	Width2 [w]	σ	Area1 [A]	σ	Area2 [A]	σ	Adj. R-square	d-spacing [nm]	Corr length [nm]
	1.5	0.917	1.34E-03			0.275	0.004			2024	20.2			0.96	6.85	7.3
	2.5	0.921	1.68E-03			0.236	0.005			1911	27.8			0.94	6.82	8.5
$pSar_{11}$	5	0.902	1.70E-03			0.290	0.005			2340	30.5			0.95	6.97	6.9
	7.5	0.917	4.65E-03	0.72945	0.0052	0.191	0.278	0.23364	0.01401	1312.5	80.6	755.28	76.9	0.93	6.39	10.5
	10	0.729	1.71E-02	0.63181	0.0055	0.244	0.017	0.12493	0.02299	738.6165	157.6	359.29	136.0	0.91	6.41	12
	1.5	0.944	1.04E-02			0.255	0.004			2661	30.1			0.96	6.66	7.9
	2.5	0.939	6.10E-03			0.271	0.005			2664	33.0			0.95	6.69	7.4
$pSar_{23}$	5	0.930	1.76E-03			0.283	0.005			2187	28.9			0.94	6.76	7.1
	7.5	0.920	1.74E-03			0.302	0.005			1582	20.1			0.94	6.83	6.6
	10	0.908	2.17E-03			0.292	0.007			1321	21.6			0.92	6.92	6.9
	1.5	0.943	1.48E-03			0.264	0.004			2397	28.4			0.96	6.66	7.6
	2.5	0.940	1.79E-03			0.266	0.005			2249	31.1			0.94	6.68	7.5
$pSar_{34}$	5	0.932	1.94E-03			0.294	0.006			1344	19.2			0.93	6.74	6.8
	7.5	0.927	2.61E-03			0.272	0.008			661	14.0			0.87	6.78	7.3
	10									0						
	1.5	0.947	1.66E-03			0.287	0.005			2486	30.5			0.95	6.63	7
	2.5	0.946	2.07E-03			0.293	0.006			1605	24.4			0.93	6.64	6.8
$pSar_{65}$	5	0.945	2.83E-03			0.276	0.009			475	10.5			0.86	6.65	7.3
	7.5									0						
	10									0						
	1.5	0.927	1.90E-03			0.310	0.006			2268	29.5			0.94	6.77	6.4
	2.5	0.901	2.11E-03			0.328	0.007			1508	21.3				6.97	6.1
PEG-DMG	5	0.853	5.91E-03			0.324	0.020			358.4	16.2			0.58	7.37	6.2
	7.5									0						
	10									0						

Table S 6. **Physicochemical characterization of ionizable lipids.**

Formulation	Particle Size [nm]	PdI	mRNA Accessibility [%]
DODMA: Chol:DSPC:pSar$_{23}$ (40:45:10:5)	84.0	0.151	79.8
KC2:Chol:DSPC:pSar$_{23}$ (40:45:10:5)	83.6	0.129	59.2
MC3:Chol:DSPC: pSar$_{23}$ (40:45:10:5)	82.3	0.150	35.7
cKK-E12:Chol:DSPC: pSar$_{23}$ (40:45:10:5)	3476.3	Multimodal	86.3
DLP14:Chol:DSPC: pSar$_{23}$ (40:45:10:5)	79.1	0.135	51.1
DPL38:Chol:DSPC: pSar$_{23}$ (40:45:10:5)	107.8	0.159	67.8
DPL57:Chol:DSPC: pSar$_{23}$ (40:45:10:5)	88.0	0.138	59.9
DPL1:Chol:DSPC: pSar$_{23}$ (40:45:10:5)	123.3	0.301	67.6
DPL52:Chol:DSPC: pSar$_{23}$ (40:45:10:5)	314.2	0.280	44.3
DPL53:Chol:DSPC: pSar$_{23}$ (40:45:10:5)	76.1	0.173	44.2
DPL58:Chol:DSPC: pSar$_{23}$ (40:45:10:5)	70.6	0.352	44.4
HY-405:Chol:DSPC: pSar$_{23}$ (40:45:10:5)	114.7	0.118	35.6
HY-PIP:Chol:DSPC: pSar$_{23}$ (40:45:10:5)	79.1	0.144	44.9

Table S 7. **Physicochemical characterization of pSar$_{23}$-LNP comprising DODMA, Dlin-MC3-DMA, and DPL14 ionizable lipids.**

Lipid Composition	Molar fraction [%]	N/P	Weight/weight ratio [w/w]	Particle Size [nm]	PdI	RNA accessibility [%]
DODMA:Chol:DSPC:pSar$_{23}$	40:45:10:5	4	17.8	84.0	0.151	79.8
MC3: Chol:DSPC:pSar$_{23}$	40:45:10:5	4	18.1	82.3	0.150	35.7
DPL14: Chol:DSPC:pSar$_{23}$	40:45:10:5	4	18.1	79.1	0.135	51.1

***Table S 8. Physicochemical characterization of $pSar_{23}$ and PEG-DMG LNP containing DPL14 ionizable cationic* lipids**.

Lipid Composition	Molar fraction [%]	N/P	Weight/weight ratio (w/w)	Particle Size [nm]	PdI	Zeta Potential [µm.cm/V.s]	mRNA accessibility [%]
DPL14:Chol:DSPC:PEG-DMG	40:48.5:10:1.5	4	16.8	87	0.196	2.48	5.6
DPL14: Chol:DSPC:$pSar_{23}$	40:45:10:5	4	18.8	85	0.166	2.6	47.9

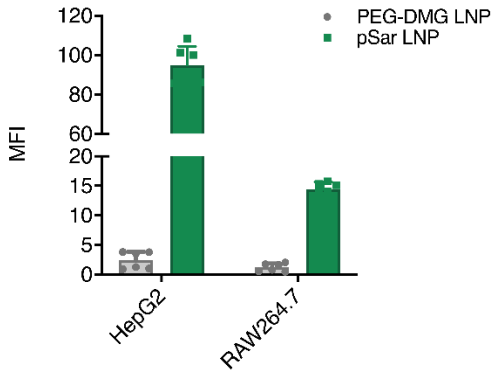

Figure S 13. Binding experiments with pSar and PEG LNP.
LNP formulated with PEG-DMG and $pSar_{23}$ were incubated with RAW244.7 and HepG2 cells at *50* ng for *30 min* at 4° C. Briefly, LNP composed of DPL14:Chol:DSPC:PEG-DMG (40:48.5:10:1.5 mol %) and DPL14: Chol:DSPC:$pSar_{23}$ (40:45:10:5 mol %) at N/P ratio 4. Data is represented as fold increment in MFI ± standard deviation, for n=*2*, 3 replicates. The results indicate that pSar LNP bind more efficiently to hepatocytes and macrophages than PEG-DMG LNP.

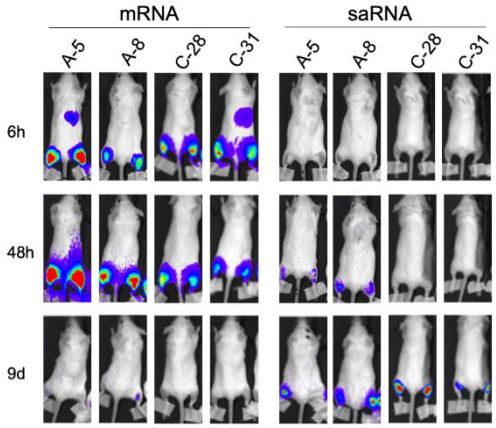

Figure S 14. Biodistribution expression of mRNA vs saRNA.
Balb/C mice were injected IM (each leg) with 1 µg of luciferase encoding-mRNA formulations A-5, A-8, C-28 and C31. Luciferase expression 6 h post IM injections can be found in the injection area, and for PEG-LNP also in the liver. Data are presented as mean ± SD, for n=3. These results indicated that pSar grafted lipids reduced off-target expression without diminishing the activity in the injection area.

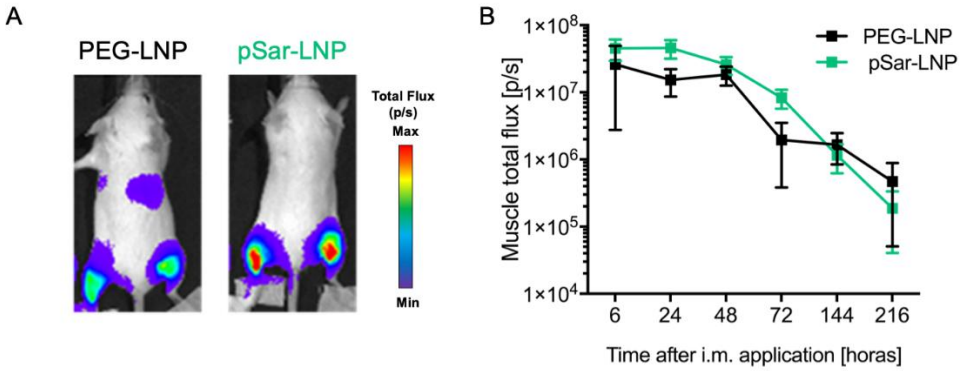

Figure S 15. Biodistribution expression of pSar compared to PEG-based LNP.
Balb/C mice were injected IM (each leg) with 1 µg of luciferase encoding-mRNA formulated into 2.5 % pSar or 2 % PEG LNP. Luciferase expression 6 h post IM injections can be found in the injection area, and for PEG-LNP also in the liver. Data are presented as mean ± SD, for n=3. These results indicated that pSar grafted lipids reduced off-target expression without diminishing the activity in the injection area.

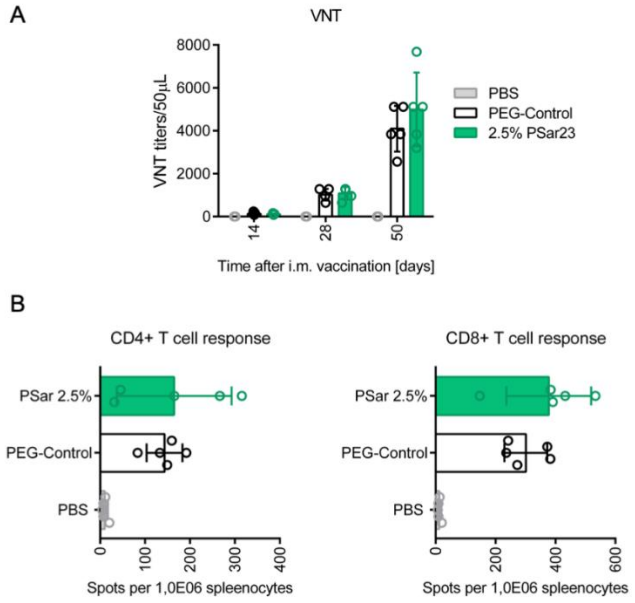

Figure S 16 Immune response of pSar LNP compared to PEG-based LNP.
BALB/c mice were immunized IM with 10 µg of H1N1-HA coding mRNA or buffer solution only (PBS). H1N1-specific antibody was measured by E VNT (A) 14-, 28- and 50-days weeks after IM LNP administration. Immunogenicity is represented as area under curve (AUC), with 5 mice per group. B) T cell response after 50 days post-immunization, with 5 mice per group. Statistical analyzes was performed with ordinary one-way ANOVA with Dunnett's multiple comparisons test of LNP formulations vs buffer * - P <0.05, ** P<0.01, ***P<0.001, ****P<0.0001.

Table S 9. Summary of physicochemical characterization of LNP encoding a model antigen HA.

ID	Lipid composition	Molar fraction [%]	Particle size [nm]	PDI	mRNA Accessibility [%]
A-8	DODMA:Chol:DOPE:PEGcerC16	40:48:10:2	87.25 ± 2	0.193 ± 0.004	26.1 ± 1
C-29	DODMA:Chol:DOPE:$pSar_{23}$	40:47.5:10:2.5	143.1 ± 6	0.236 ± 0.02	13.6 ± 1
C-30	DODMA:Chol:DOPE:$pSar_{23}$	40:45:10:5	106.3 ± 2	0.229 ± 0.05	31.3 ± 1
C-32	DODMA:Chol:DOPE:PEG-DMG	40:47.5:10:2.5	78.55 ±1	0.125 ± 0.03	38.3± 1

Affidavit

I hereby declare that I wrote the dissertation submitted without any unauthorized external assistance and used only sources acknowledged in the work. All textual passages which are appropriated verbatim or paraphrased from published and unpublished texts as well as all information obtained from oral sources are duly indicated and listed in accordance with bibliographical rules. In carrying out this research, I complied with the rules of standard scientific practice as formulated in the statutes of Johannes Gutenberg University Mainz to insure standard scientific practice.

Chapters 2, 3 and 4 use text, tables and figures of the following publication:

Sara S. Nogueira, Anne Schlegel, Konrad Maxeiner, Benjamin Weber, Matthias Barz, Martin A. Schroer, Clement E. Blanchet, Dmitri I. Svergund Srinivas Ramishetti, Dan Peer, Peter Langguth, Ugur Sahin & Heinrich Haas. Polysarcosine-Functionalized Lipid Nanoparticles for Therapeutic mRNA Delivery. *ACS Applied Nano Materials 2020;* 3 (11):10634–10645

Date, Place

Sara Nogueira